SOLID-STATE NMR OF HIGH TEMPERATURE FUEL CELL ELECTROLYTES

SOLID-STATE NMR OF HIGH TEMPERATURE FUEL CELL ELECTROLYTES

BY

NICOLE E. DE ALMEIDA, B.SC, M.SC.

A Thesis Submitted to the School of Graduate Studies in Partial Fulfillment of the Requirements for the Degree Doctor of Philosophy

McMaster University

McMaster University DOCTOR OF PHILOSOPHY (2015) Hamilton, ON (Chemistry)

TITLE: Solid-State NMR of High Temperature Fuel Cell Electrolytes

AUTHOR: Nicole E. De Almeida, B.Sc. (Ryerson University), M.Sc. (University of Ontario Institute of Technology)

SUPERVISOR: Professor Gillian R. Goward

NUMBER OF PAGES: xvi, 169

Abstract

Current fuel cell operating temperatures have been unintentionally optimized for the exact conditions that poison the platinum electrode. Raising the operating temperature can eliminate poisoning. Nafion®, the current benchmark fuel cell electrolyte, operates optimally at 80°C due to its dependence on water for proton conduction. Two approaches are described here to address this issue: modification of Nafion to remain hydrated and the synthesis of new materials that can operate at high temperatures. Casting the polymer with smaller thicknesses reduces the path length and allows water to diffuse throughout the whole polymer easily. When nanothin versions of the film were cast, water uptake was found to be significantly higher. However, the observed proton conductivity decreased. Solid-state NMR was used to determine if local dynamics were an issue in nanothin films or whether long-range transport was hindered. For materials that operate via a Grotthuss mechanism, organic solid acids were studied due to their thermal and electrochemical stability and significant proton conductivity at high temperatures. For this thesis three main organic solid acids were studied, including benzimidazolium- and imidazolium- methanesulfonate (BMSA and IMSA) and imidazolium trifluoromethanesulfonate (IFMS). Solid-state NMR was used to study their hydrogen-bonded structure to determine the dynamics in each of the solid acids. The local dynamics information was then compared with their macroscale proton conductivity. To produce a suitable host for fuel cell applications, the solid acids were inserted into polymer supports to determine the best salt-host composite. Polymers supports that were investigated include Teflon, sulfonated polyetheretherketone (sPEEK) and sulfonated polysulfone (sPSU). This thesis focuses on the use of solid-state NMR to probe these composites and to study their mobility on a localized scale to explain their macroscale proton conductivity.

Table of Contents

List of Tables

List of Figures

List of Abbreviations and Symbols

PEFCs	Proton electrolyte fuel cell
PEM	Proton electrolyte membrane
PAFC	Phosphoric acid fuel cell
n	Number of electrons transferred
F	Faraday's constant
E°	Cell Voltage
ISA	Inorganic solid acid
OSA	Organic solid acid
PVDF	Polyvinylidene
PBI	Polybenzimidazole
sPEEK	Sulfonated polyetheretherketone
sPSU	Sulfonated polysulfone
PEEK	Polyetheretherketone
PSU	Polysulfone
DSC	Differential scanning calorimetry
TGA	Thermogravimetric analysis
EIS	Electrochemical impedance spectroscopy
R	Resistance
V	Voltage
I	Current
Z	Impedance
R_c	Resistance of the cell

R_p	Resistance of the polymer
Z’	Resistance of the electrochemical cell
Z”	Capacitance of the electrochemical cell
NMR	Nuclear magnetic resonance
MAS	Magic angle spinning
T_2	Spin-spin relaxation
T_2*	Spin-spin relaxation with inhomogeneity
T_1	Spin lattice relaxation
Z	Protons
N	Neutrons
I	Spin Number (observed spin)
S	Spin (non-observed spin)
m	Multiplicity of spin states
E	Energy between spin states
Bo	Applied magnetic field
γ	Gyromagnetic ratio
h	Plank's constant
k	Boltzmann constant
$N_{1/2}$	Population of spins at energy level 1/2
w	Larmor frequency
B1	Oscillating field
H_{rf}	Hamiltonian of radiofrequency
H_j	Hamiltonian of scalar coupling

H_σ	Hamiltonian of chemical shift anisotropy
H_D	Hamiltonian of dipole-dipole coupling
H_Q	Hamiltonian of quadrupolar coupling
CSA	Chemical shift anisotropy
σ_{iso}	Isotropic shift
$\Delta\sigma$	Chemical shielding anisotropy (CSA)
η_{CS}	Asymmetry in chemical shielding
ϕ	Angle of the chemical shielding tensor relative to the magnetic field
θ	Angle of the chemical shielding tensor relative to the magnetic field
σ_{11}, σ_{22}, and σ_{33}	Principal components of the chemical shielding tensor
r	Distance between two nuclei
C_q	Quadrupolar coupling constant
η_Q	Asymmetry in quadrupolar coupling
q_{xx}, q_{yy} and q_{zz}	Principal components of the quadrupolar tensor
M_z	Magnetization along z axis
M_o	Magnetization that relaxes back to the z axis
CRAMPS	Combined rotational and multiple pulse spectrocopy
PMLG	Phase modulated lee goldburg
DUMBO	Decoupling under mind boggling optimization
VT	Variable temperature
FWHM	Full width at half max
DQF	Double quantum filter
BaBa	Back-to-back

τ_R	Rotor period
DQC	Double quantum corherence

Chapter 1
Introduction to Organic Solid Acids and Composites for High Temperature Polymer Electrolyte Fuel Cells

This chapter aims to introduce different types of fuel cells focusing on polymer electrolyte fuel cells. Limitations of fuel cells will be presented specifically where voltage losses occur. Each part of the fuel cell will be discussed to understand its purpose in fuel cell technology specifically to highlight the challenges each part poses. This chapter will go into depth about the membrane, which serves as the polymer electrolyte in the fuel cell, through different methods of how proton conduction occurs, and water management. Organic solid acids will be presented as an alternative to water based polymers and details of their polymer supports will also be discussed. An explanation of the thesis' main motivations will be presented. Lastly, an overview of remainder of the chapters will be included.

1.0 Fuel Cells

Fossil fuel is currently widely used for automobiles, however they are limited resources and produce CO_2 after combustion. High CO_2 production results in damaging environmental effects, such as global warming, therefore, implementing renewable forms of energy is becoming crucial to curtail the emission of harmful greenhouse gases. Oxidizable fuel sources such as hydrogen, which can be produced via the electrolysis of water, represent one such form of energy storage. The stored energy can then be released as an electrical current through the use of a fuel cell. They represent a desirable alternative to the internal combustion engine due their compatibility with renewables and their higher fuel efficiencies.[1] Fuel cells typically use hydrogen as a fuel, which involves the controlled oxidation of a fuel source to generate electrons, which are available to do

work.

There are several types of fuel cells that operate at different temperature ranges. Solid oxide fuel cells can be used for stationary applications due to their high operation temperature of 500 - 1000°C.[2] For this fuel cell the charge carrier is O^{2-} that transverse through the ceramic electrolyte to react with the hydrogen fuel.[3] This is the cheapest of the fuel cells presented due to the electrodes not being made of expensive catalysts such as platinum, but use nickel catalysts.[4] This is due to the temperature of the fuel cell being able to reduce hydrogen and oxidize oxygen without the requirement of a catalyst. Due to the high temperatures the solid oxide fuel cell possess slow startup times and requires significant shielding from heat making this cell unsuitable for portable applications.[5] Phosphoric acid fuel cells (PAFC) use concentrated liquid electrolyte for the proton conductor. Due to the liquid electrolyte phosphoric acid fuel cells operate at much lower temperatures than solid oxide fuel cells (200°C). However, the electrolyte must be replaced often due to its highly corrosive properties.[6]

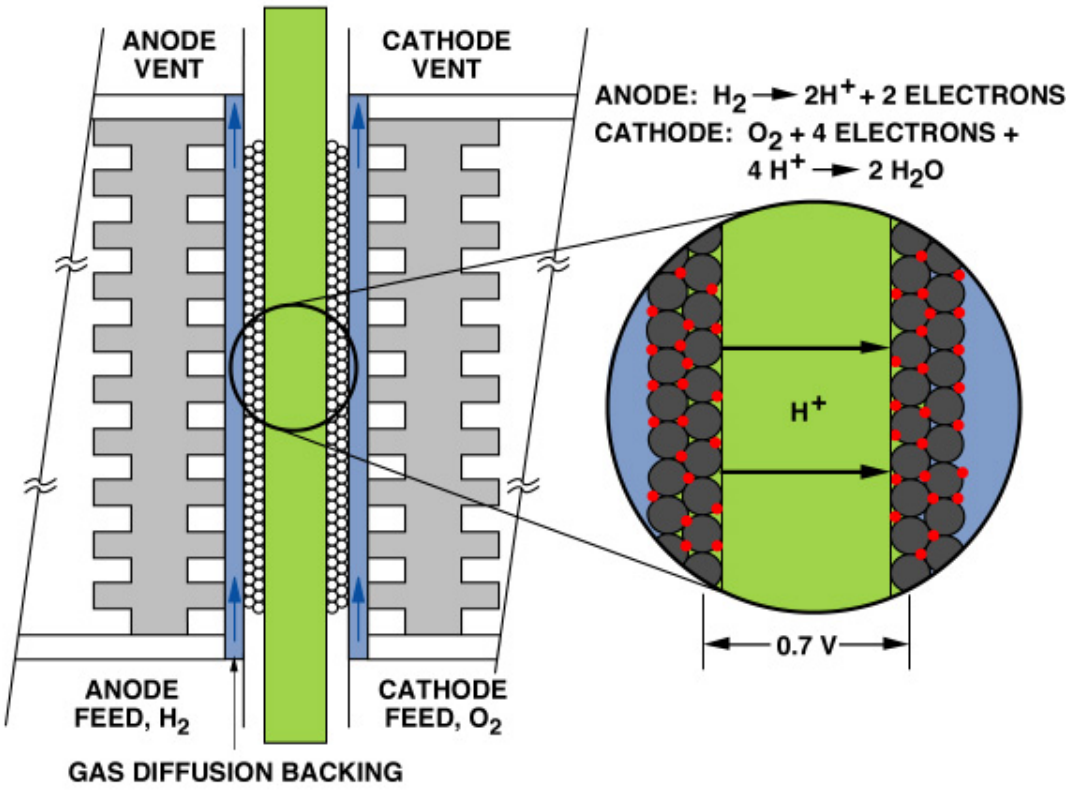

Figure 1.1: Cross-Section of a polymer electrolyte fuel cell, insert of platinized carbon catalyst layer with polymer electrolyte. Figure is the courtesy of National Energy Technology Laboratory (NETL), U.S. Department of Energy.[7]

Depicted in **Figure 1.1** is a cross section of PEFC that consists of an anode and cathode separated by solid polymer electrolyte membrane (PEM). PEFCs operate by having hydrogen introduced to the anode, which is oxidized to protons and electrons as seen in **Equation 1.1**. The electrons travel though an external circuit to power an application and the protons traverse through the polymer electrolyte. On the cathode oxygen undergoes a reduction with the electrons and protons to form water as seen in **Equation 1.2**. The overall reaction can be seen in **Equation 1.3**. Using Gibbs free energy in **Equation 1.4**, where n is amount of electrons being transferred, F is the Faraday's constant and E° is the cell voltage, the Gibbs free energy can be determined to

be -237.35 kJ/mol, which indicates a spontaneous reaction. However, the voltage is only a theoretical voltage that cannot be obtained realistically due to several factors.

Anode: $H_2 \rightarrow 2H^+ + 2e^-$ $E° = 0$ V **(1.1)**

Cathode: $½O_2 + 2H^+ + 2e- \rightarrow H_2O$ $E° = 1.23$ V @ 298 K **(1.2)**

Overall: $2H_2 + ½O_2 \rightarrow H_2O$ $E° = 1.23$ V @ 298 K **(1.3)**

$$\Delta G = -nFE \quad \textbf{(1.4)}$$

Each part of the fuel cell possesses resistance that contributes to the over potential and lowers the overall voltage. Even with this over potential, PEM-FCs possesses a higher electrical efficiency than the combustion engine.[8] The combustion engine is 30 % efficient and fuel cells are 80 % efficient with heat recovery.

1.1: PEM-FC Electrodes

Fuel cells contain two electrodes, anode and cathode, which both consist of the same materials. Both the anode and cathode are made of carbon, platinum and ionomer. Carbon is present to conduct the electrons to and from the load of the cell. The function of platinum is to catalyze both reactions that occur in each electrode (more details below). Ionomer is used to aid in proton conduction within the electrodes to assist protons to transverse to and from the electrolyte.

The anode is involved in catalyzing the oxidation of hydrogen into protons and electrons. This reaction is highly efficient and is the part of the fuel cell that requires the least energy. The cathode, however, is responsible for the highest energy loses in the fuel cell. The cathode is where the oxygen reduction reaction takes place, which possesses

high activation energy because it is a three-phase reaction.[6]

Early renditions of the fuel cell did not contain ionomer, in which case higher platinum loadings were necessary within each electrode to obtain decent performance.[9] With the introduction of ionomer into the electrodes, the amount of platinum required was dramatically reduced. When adding ionomer to the electrodes the ionomer must not block gas diffusion into the electrodes but still aid in proton conduction throughout the whole electrode. Currently, the ionomer used is the same material as the electrolyte, which is Nafion, a fluorinated polymer. Overall, the morphology of the electrodes is a topic of intense ongoing investigation, but it is not the focus of this thesis.[10]

1.2 Electrolytes

Fuel cell electrolytes are present between the two electrodes, and should prevent gas diffusion, be ionically conductive, but not electronically conductive. The electrolyte must also perform at temperatures above 100°C to prevent carbon monoxide poisoning on the platinum catalyst. Carbon monoxide is introduced into fuel cells based on the current inexpensive method of producing hydrogen gas from steam formation of methane. Hydrogen that is produced from methane contains ~0.5% CO that would poison the electrodes.[7] Platinum prefers binding to CO than hydrogen due to its high electron density that exists in the triple bond and is chemisorbed to the platinum surface over hydrogen. Carbon monoxide chemisorption can be significantly reduced with higher temperatures (>120°C) from the Pt-O=C bond being unfavorable at these temperatures however, the specific mechanism of this behaviour is highly debated in literature but it is believed to be due to the bond energy being overcame at higher temperatures based on simulations.[11] To put this in perspective at 80°C fuel cells can only tolerate 0.00025% CO

and at 120°C the fuel cell CO tolerance increases upwards to 5% dramatically limiting poisoning on the platinum surface.[7] Currently, our best electrolyte is Nafion, which represents the best compromise for the various properties desired for an electrolyte.

1.2.1 Nafion

Nafion was first developed by Dupont in the 1970s and has become the industry standard to which all new materials are compared.[12] It possesses desirable properties such as durability, chemical resistance and a high proton conductivity that has not been surpassed by any other material to date.[12] Nafion's structure consists of a fluorinated backbone that has fluorocarbon side chains with sulfonic acid terminated ends (**Figure 1.2**).[13] The sulfonic acid ions form ionic, hydrophilic clusters throughout the membrane promoting pore formation within the polymer.[14] Proton conductivity within Nafion is achieved by proton hopping from water to sulfonate groups. Therefore, to remain highly conductive, Nafion has to maintain hydration throughout use and cannot be operated above 80°C otherwise proton conductivity decreases dramatically.[15] The U.S Department of energy target operating temperature for PEMFC operating temperature is 120 to 150°C. The higher temperatures are necessary to obtain acceptable current densities for automobile use and to reduce catalyst poisoning due to carbon monoxide.[16,17] However, unmodified Nafion is incapable of reaching this target because of its dependence on water content and the 100°C glass transition temperature which limits its mechanical stability.[18] Another issue with Nafion arises from the dangerous synthetic chemistry involved in making fluorinated polymers and the resultant high manufacturing cost. There are two main methods to combat these issues: adding additives to Nafion to improve water retention or to synthesize a new class of polymers that can operate at higher temperatures.

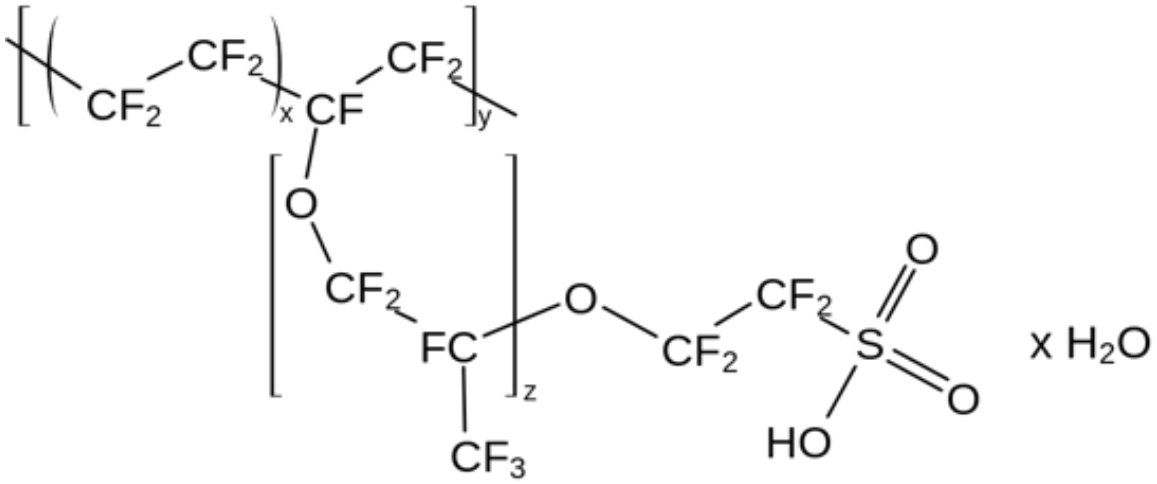

Figure 1.2: Structure of Nafion 1100 (x=6, Z=1)

Nafion composites have been heavily studied in literature. A common approach is to add chemical additives to Nation to enhance performance at higher temperatures to increase water retention or assist in synergistic proton conduction and water retention.[19] Therefore, hygroscopic additives are inserted to enhance water retention properties at high temperatures and low humidity conditions. Examples of additives include SiO_2 and TiO_2, which maintain water content but do not contribute to proton conductivity.[20,21] The additives chosen were electrically neutral to ensure the proton conductivity of Nafion was not competitively inhibited by ionic exchange with the additive.

1.2.1.1 Vehicular Mechanism

Vehicular transport, using typically water, is utilized in Nafion as well as most hydrocarbon polymers. This mechanism exploits the fact that there are free volumes of space throughout the polymer. These free spaces allow guest molecules to assist in movement of protons between conducting groups. The guest molecule physically binds with the proton and diffuses throughout the polymer behaving like a Bronsted base (a proton acceptor).[22] In particular, Nafion uses water to transport protons between sulfonate groups as seen in **Figure 1.3**. Issues with this mechanism for fuel cells relate to

significant water sensitivity. For example, insufficient water limits proton conduction, as the conduction mechanism is directly dependent on its presence to transport protons across the film. Therefore, operation of a fuel cell with water requirements can be difficult to maintain proper hydration levels for optimal proton conduction.

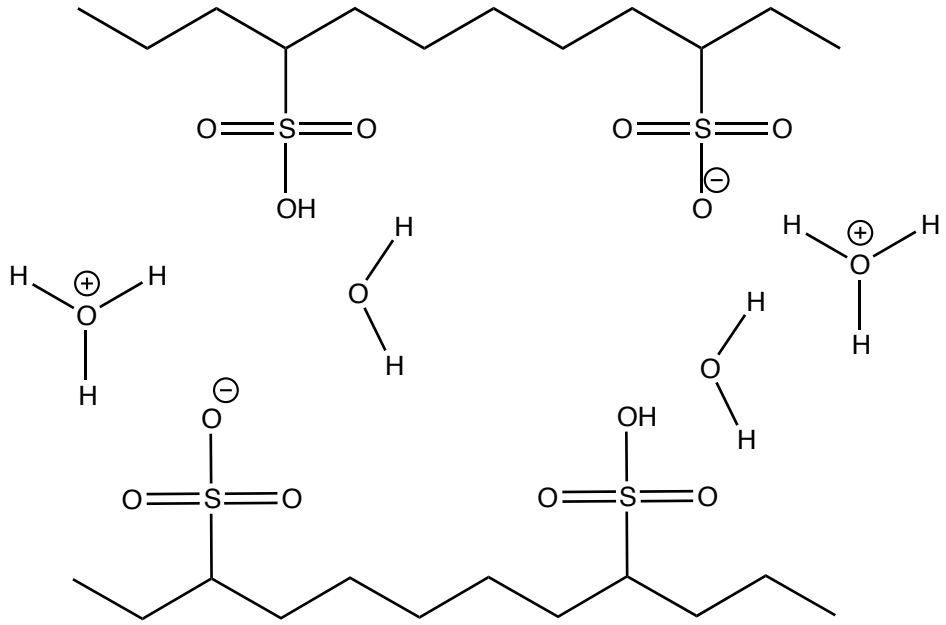

Figure 1.3: Vehicle mechanism of proton transport

1.2.2 Solid Acids as Electrolytes

One promising class of materials for fuel cell electrolytes are solid acids. Solid acids have gained interest recently from their high electrochemical stability, ideal melting points and high proton conductivity under anhydrous conditions.[23,24] There are two main categories of solid acids that these inorganic solid acids (ISA) and organic solid acids (OSA).

The first of the inorganic solid acids used for fuel cells were those involving oxyacids. The series of oxyacids were in the format of XO_4, where the X is P, S and Se were paired with first group metals cations such as Na, K, Rb and Cs.[25] The first

combination that was used for fuel cell applications was $CsHSO_4$ as described by Haile et al.[26] $CsHSO_4$ possesses a high proton conductivity of $3.13x10^{-2}$ S/cm at 150°C that was maintained for 80 hours.[26] $CsHSO_4$ goes through at superprotonic transition, where a state of high disorder is observed, which dramatically increases proton conductivity. For $CsHSO_4$ the structure changes from a monoclinic to a tetragonal structure at 141°C and the proton conductivity increases by 2-3 orders of magnitudes to $3.13x10^{-2}$ S/cm.[27]

Organic solid acids (OSAs) involve an organic cation with organic acid to make an overall acidic salt. Previously investigated OSAs were phosphate derivatives with heterocycles.[23,28] It was shown that heterocycles possessed dynamics that was determined through solid-state NMR.[29,30] For this thesis sulfonated-functionalized OSAs were investigated. OSAs were prepared by combining an organic heterocycle, to act as base, with an acidic anion to produce an overall acidic salt. For this thesis organic cations that have exhibited dynamics (imidazole and benzimidazole) were combined with sulfonic acids to form organic solid acid salts. However, these salts do not possess the mechanical properties to form thin films and thus a polymer support is required for these materials to be suitable for fuel cell operation.

1.2.2.1 Grotthuss Proton Transport

These materials utilize a Grotthuss mechanism, also known as structural diffusion, for proton conduction that involves the breakage and formation of hydrogen bonds as the proton transverses throughout the material.[31,32]

Materials that can physically rotate or flip to transfer protons use the Grotthuss mechanism for proton transport as seen in **Figure 1.4**. Since it is based on the physical process within the molecule this mechanism possesses higher activation energy than the

vehicular mechanism. However, since the mechanism does not depend on water content, issues arising from excess or insufficient water content are not a factor. Grotthuss mechanism based materials must operate at a higher temperature to be competitive with compounds that possess a vehicular mechanism, in order to circumvent the high activation energy.

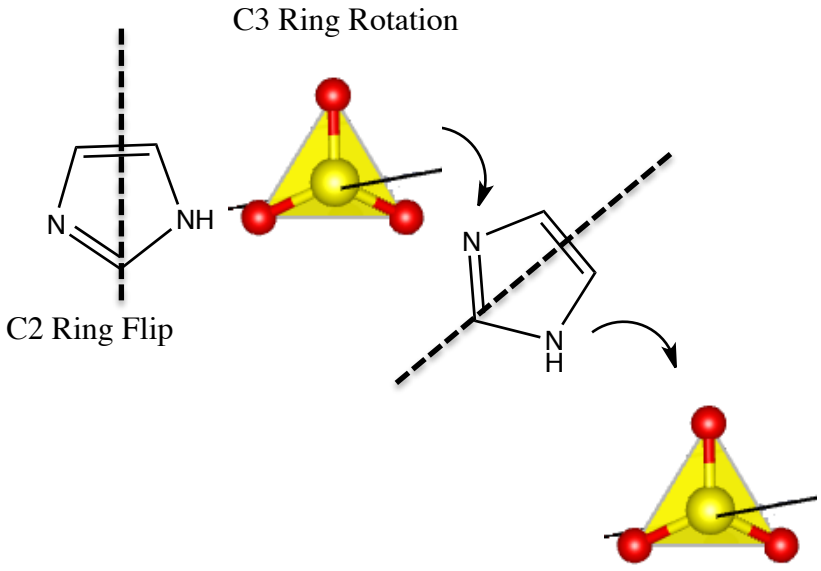

Figure 1.4: Grotthuss mechanism of proton transport

1.2.2.2 Inert Polymer Hosts

In order for OSAs to be suitable for fuel cell applications a polymer support is required since OSAs do not readily form thin films. Using inert hosts, solid acids can be supported into a film to conduct protons. Previous research has used PVDF and PTFE as hosts for inorganic solid acids. For Grotthuss mechanism bonds tend to break for protons to be transferred to another compound. This process only works if there are defects in the structure because if there were protons in every available site proton conduction would not occur. The host increases the salt's proton conductivity by increasing the defects in the overall structure.

Ionic salts can be incorporated into polymers to provide the necessary mechanical support. A polymer support previously investigated is polyvinylidene fluoride (PVDF), where the main advantages were that it has high chemical resistance and is inexpensively manufactured. ISA-PVDF was the first class of composites, using $CsHSO_4$. Previous research showed that the higher the salt loading the higher the proton conductivity. At 20% $CsHSO_4$-PVDF proton conductivity was at $1x10^{-6}$ S/cm at 160°C and at 90% $CsHSO_4$-PVDF the proton conductivity dramatically increased to $1x10^{-2}$ S/cm.[33] However, PVDF contains large pores that allow gas diffusion of reactants across the membrane from composites tested thus far.[15] However, the SEM micrograph shows the loading of the OSA is not homogeneous as seen in **Figure 1.5A**. With this homogeneous loading numerous dead-ends would be created decreasing proton conductivity. Thus salt-Teflon composites have been synthesized where proton conductivity was increased after inserted into Teflon.[34,35]

A B

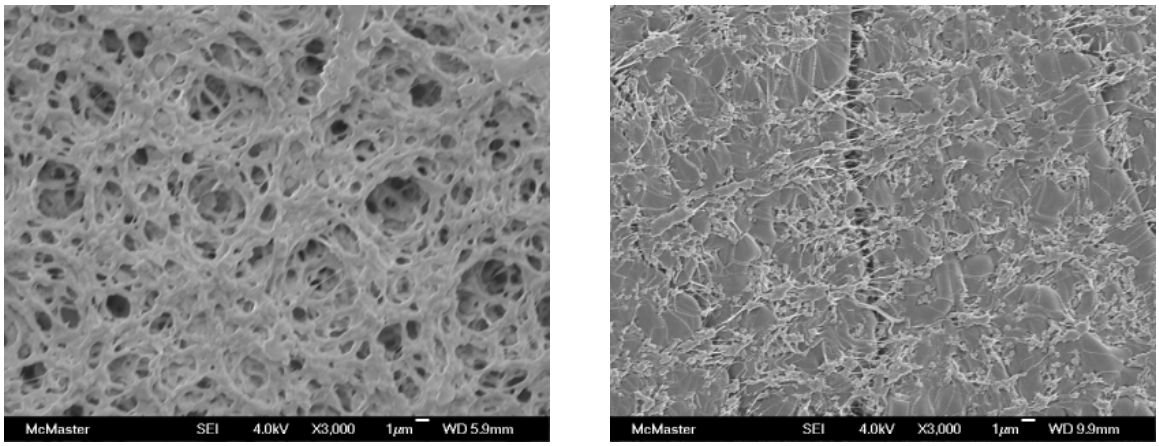

Figure 1.5: SEM of Inert Polymer Hosts A) PDVF, salt insertion is heterogeneous B) PTFE, salt insertion is homogeneous. Figure reproduced with permission from Physical Chemistry Chemical Physics.[29]

Porous Teflon is another host candidate, which behaves similar to PVDF. However, composites formed from it exhibited a limited degree of gas diffusion as a result of smaller pore sizes.[16] In the SEM micrograph homogeneous loading to create the potential of higher proton conductivity by containing more complete pathways of the salt throughout the polymer as seen in **Figure 1.5B**.

However, both supports suffer from the leaching of the ionic salts due to a lack of ionic interactions on the polymer itself. Thus combining salts with a sulfonate functionalized hydrocarbon host has the advantage that the solid acid is chemically bonded to the polymer through sulfonic acids to prevent the salt from leaching out of the composite. Hydrocarbon polymers such as polybenzimidazole (PBI), sulfonated polyetheretherketone (sPEEK) and sulfonated polysulfone (sPS) have previously shown to form composites and are excellent candidates for a host material.[36,37] The host in this case can also contribute its own proton conductivity to assist the salt. Typically a high degree of sulfonation was required to obtain high proton conductivity, however this also decreased the mechanical stability of the polymer. Sulfonated-functionalized hydrocarbon polymers fail when operated anhydrously at high temperatures due to the dependence of water for proton conduction. With the addition of salts into these sulfonated functionalized hosts, with the absence of water, would aid the composite to operate at ideal fuel cell conditions. Previous salt hydrocarbon polymer composites were made using $CsHSO_4$-PVDF and SiO_2-sPEEK, however these composites were still studied in humidified conditions often with acid doping.[33,38]

1.2.2.3 Sulfonate Functionalized Hosts

Hosts that can also participate in proton conductivity are hypothesized to be beneficial for use in solid acid composites. Additionally, the host could aid in retaining the salt due to its hydrogen-bonded network whereas an inert host could not assist in this fashion. Two different hosts were investigated for this thesis, which were polyetheretherketone (PEEK) and polysulfone (PSU). For this thesis sulfonation reactions were performed on PEEK and PSU for the hydrocarbons to be conductive. Typically, the higher DS the higher the water uptake and thus the mechanical strength of the polymer decreases. However, the goal in this thesis is to operate the fuel cell anhydrously (no added humidity) and at high temperatures thus decreasing catalyst poisoning and improving operating conditions.

1.3 Macroscale Analysis of PEMs

1.3.1 Thermal Analysis

Differential scanning calorimetry (DSC) is used to quantitatively study thermal transitions, with respect to a standard.[39] During DSC the sample is heated slowly and compared to a standard. When a phase change occurs, for example cross-linking in a polymer, the heat flow must be increased to match the reference sample creating a peak in the DSC curve. The peak area is directly proportional to the change in enthalpy.[39] This technique was used in this thesis to determine melting points of the organic solid acids studied.

Thermogravimetric analysis (TGA) measure how mass is lost as function of temperature instead of heat flow changes.[40] This technique is performed under air or inert gases to determine how a sample combusts or decomposes. The thermogram shows weight percent lost as a function of temperature. This technique determines the quantity

of solvent, functionalization of polymer as well as percent composition of additives. In this thesis TGA is used to determine residual solvent and salt loading into a polymer host.

1.3.2 Electrochemical Impedance Spectroscopy

To determine the conductivity of a membrane, electrochemical impedance spectroscopy (EIS) is employed. Impedance under ideal circumstance is equivalent to the idea of resistance as described by Ohm's law (**Equation 1.5**), where the current and voltage responses are in phase with each other, where R is the resistance of the circuit, I is the current and V is the voltage.[41] Ohm's law is applied when considering circuits based on direct current however, the consideration of alternating current involves the case where current and voltages responses are out of phase with respect to each other.

$$R = \frac{V}{I} \tag{1.5}$$

In real cases impedance (Z) the ability to impede on electrical current, is used instead of resistance. In **Equation 1.6** represents an observed voltage (V), where V_o is initial voltage, ω is angular frequency and t is time. In alternating current circuits there is a phase shift (ϕ) in the current response and in **Equation 1.6** showing the current response the applied voltage. In **Equation 1.6** is the sinusoidal response that describes impedance. Impedance responses are plotted on a Cartesian plane called a Nyquist plot from high frequency to low frequency. The Nyquist plot is presented with a x-axis that is the resistance or impedance of the circuit in units of Ωcm denoted as Z' and a y-axis that is negative which is the capacitance of the circuit in the units of farad (F) denoted as Z".

$$Z = \frac{V}{I} = \frac{V_O sin(wt)}{I_O sin(wt + \phi)} = Z_o \frac{in(wt)}{in(wt + \phi)} = Z_o(cos\phi + isin\phi) \tag{1.6}$$

With EIS an electrical circuit model is used to describe the system being considered. In **Figure 1.6A** shows the electrical circuit model for a PEM, which involves

resistor attached to a resistor and capacitor in parallel. The capacitor represents protons in the PEM and the electrons on the cathode as if it is storing a charge. The two resistors represent the resistance of the cell (R_c) and the resistance of the polymer (R_p).[24] The impedance response is a semicircle that is shifted to the right, where the first intercept is the resistance of the cell and the second intercept is the resistance of the cell and the resistance of the polymer. Therefore, to determine the resistance of the polymer the semicircle is fitted to obtain the diameter, which is just the resistance of the polymer. Typical Nyquist plots can be seen in **Figure 1.6B**, which depicts a Nafion composite and its response to variable humidity. As the humidity increases the polymer resistance decreases as observed by the semicircle possessing a smaller diameter. Polymer resistances are used to determine the proton conductivity as seen in **Equation 1.7**, where L is the length of the polymer (cm), R_p as discussed above is in Ω, A is the area of the polymer in cm^2 and σ represents proton conductivity in S/cm, where S is in Siemens which represents 1/Ω.

$$\sigma = \frac{L}{R_p * A} \quad \textbf{(1.7)}$$

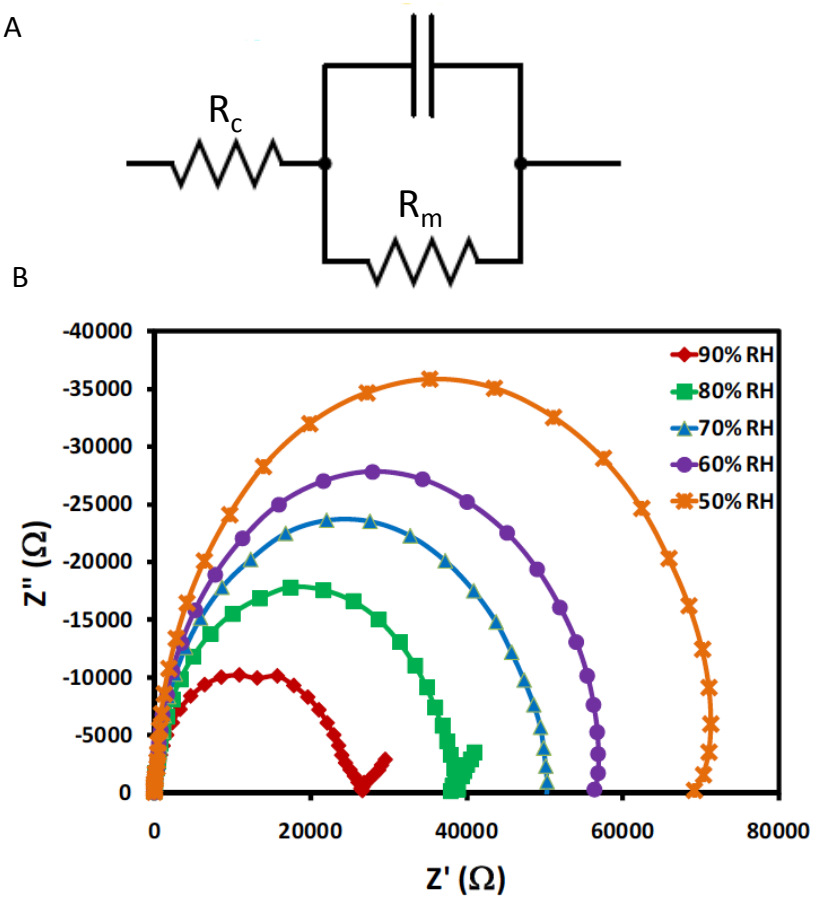

Figure 1.6: Electrochemical Impedance Spectroscopy A) the electrochemical Circuit of a Proton Exchange Membrane B) Typical Nyquist EIS measurement of Nafion with a Function of Humidity. As the humidity increases the semicircle decreases meaning the polymer is possesses less resistance. Figure reproduced with permission from the journal of Thermal Analysis and Calorimetry.[42]

EIS can be measured using two different methods, which are in-plane or through-plane. Through-plane EIS is conducted by a two electrode arrangement, typically used for powders. In order for this cell arrangement to be feasible an electronically conductive layer must be placed on either side of the cell. This can be achieved through a gold or platinum coating or by applying a layer of platinized carbon. The advantage of this method is that in-plane EIS is in the same orientation as a fuel cell. A through-plane EIS measurement has four contacts and all the wires leading to the polymer are platinum. There are several advantages of this cell arrangement, which are the additional accuracy

of a four-cell setup over a two-cell setup, no additional sample preparation and the cell is open to the environment, therefore variable humidity controlled EIS can be conducted in addition to variable temperature. For this thesis in-plane conductivity was used for powder samples that were pressed and gold coated and through-plane conductivity was used for polymers and salt composites.

1.4 Motivation and Goals

Current polymer electrolyte fuel cells suffer from water management issues which arise from the high humidity conditions necessary to enable proton conduction in the electrolyte. By limiting the water required for fuel cell operation, temperatures can be increased to improve catalyst longevity and issues such as flooding can be eliminated. Two methods are employed to reduce water content; synthesis of thinner polymer electrolytes to promote more effective hydration, and the synthesis of electrolytes, which can conduct anhydrously such as organic solid acids. The goal of this thesis is to describe how proton conduction is improved or hindered in these materials by characterizing mobility on a localized scale and to explain macroscale proton conductivity. To achieve this, solid-state NMR (Chapter 2) is used to probe hydrogen-bonded networks on a localized scale to determine pathways and mobility within the network. The first set of materials are nanothin casted Nafion films, which uptake more water, however they possess a larger activation energy for proton conductivity when compared to the thicker derivatives of Nafion. In this thesis solid-state NMR will be used to determine how the conductivity was affected either by a localized change or issues with long-range transport. Studies on nanothin Nafion films have an application towards

a better understanding of cathode operation where the electrolyte thickness approaches those of the independently studied Nafion thin films.

A goal of this thesis is to understand local mobility of anhydrous electrolytes, specifically OSAs. Due to the fact that OSAs cannot form thin films, a combined investigation of salt-polymer dynamics both on a localized scale with solid-state NMR and macroscopically with EIS is conducted. Three organic solid acids were investigated, which were benzimidazole and imidazole paired with methanesulfonate and imidazole paired with trimethylfluorosulfonate to make an overall acidic salt. Dynamics of these salts were studied by themselves and in polymer hosts to investigate how the polymer influences local mobility and ultimately proton conductivity. Three hosts were investigated for this thesis: an inert host (Teflon), and two hydrocarbon hosts (sPEEK and sPSU), where the hydrocarbon host was functionalized to further assist in the proton conductivity of OSAs.

1.5 Thesis Outline

The first chapter introduces the current state of materials and macroscale analysis for proton exchange membrane fuel cells. The solid-state NMR techniques used in this thesis are introduced in chapter 2, which involve dipole-dipole recoupling sequences and ^{2}H static NMR to probe hydrogen-bonded networks. In chapter 3 solid-state NMR is utilized to investigate the difference in proton conducting pathways in ultrathin and nanothin Nafion films. The ultrathin films behave similarly to Nafion, however the ultrathin Nafion film possesses higher water content but lower proton conductivity. From this the question arises of whether the phenomenon is due to local dynamics or long-range

transport. In Chapter 4 the ^{1}H homonuclear the dipolar recoupling method, POST C7, is used to characterize the OSAs themselves, and thereby determine the existence of a correlation between the averaging of the dipole-dipole coupling interaction and the macroscale property of proton conductivity in organic solid acids. In chapter 5 OSAs-Teflon composites are synthesized and solid-state NMR is used to describe the morphological changes between the salt itself and the composite on a localized scale, ultimately helping to explain the observed proton conductivity. In chapter 6, ^{2}H NMR is used to determine hopping rates in composites composed of OSAs and sulfonate functionalized polymers. This chapter investigates the role of homogeneous and heterogeneous functionalization to determine if this affects the hopping rate of OSA within the composite. Chapter 7 is a summary of this thesis and contains a proposed set of future directions.

1.7 References

1. Steele, B. C. H. & Heinzel, A. Materials for fuel-cell technologies. *Nature* **414,** 345–352 (2001).
2. Ormerod, R. M. Solid oxide fuel cells. *Chem. Soc. Rev.* **32,** 17–28 (2003).
3. Tsipis, E. V. & Kharton, V. V. Electrode materials and reaction mechanisms in solid oxide fuel cells: a brief review. *J. Solid State Electrochem.* **12,** 1367–1391 (2008).
4. Malavasi, L., Fisher, C. A. J. & Islam, M. S. Oxide-ion and proton conducting electrolyte materials for clean energy applications: structural and mechanistic features. *Chem. Soc. Rev.* **39,** 4370–4387 (2010).

5. Haile, S. M. Fuel cell materials and components. *Acta Mater.* **51,** 5981–6000 (2003).
6. O'Hayre, R., Cha, S.-W., Colella, W. & Prinz, F. *Fuel Cell Fundamentals*. (John Wiley & Sons, 2006).
7. Services, E. T. *Fuel Cell Handbook*. (U.S. Department of Energy, 2004).
8. Carrette, L., Friedrich, K. A. & Stimming, U. Fuel Cells - Fundamentals and Applications. *Fuel Cells* **1,** 5–39 (2001).
9. Costamagna, P. & Srinivasan, S. Quantum jumps in the PEMFC science and technology from the 1960s to the year 2000: Part I. Fundamental scientific aspects. *J. Power Sources* **102,** 242–252 (2001).
10. Holdcroft, S. Fuel Cell Catalyst Layers: A Polymer Science Perspective. *Chem. Mater.* **26,** 381–393 (2013).
11. Jacob, T., Muller, R. P. & Goddard, W. A. Chemisorption of Atomic Oxygen on Pt(111) from DFT Studies of Pt-Clusters. *J. Phys. Chem. B* **107,** 9465–9476 (2003).
12. Smitha, B., Sridhar, S. & Khan, A. A. Solid polymer electrolyte membranes for fuel cell applications—a review. *J. Membr. Sci.* **259,** 10–26 (2005).
13. HeitnerWirguin, C. Recent advances in perfluorinated ionomer membranes: Structure, properties and applications. *J. Membr. Sci.* **120,** 1–33 (1996).
14. Mauritz, K. A. & Moore, R. B. State of understanding of Nafion. *Chem. Rev.* **104,** 4535–4585 (2004).

15. Zhang, J., Tang, Y., Song, C., Cheng, X. & Wang, H. PEM fuel cells operated at 0% relative humidity in the temperature range of 23–120°C. *Electrochimica Acta* **52,** 5095–5101 (2007).
16. Kabasawa, A., Saito, J., Miyatake, K., Uchida, H. & Watanabe, M. Effects of the decomposition products of sulfonated polyimide and Nafion membranes on the degradation and recovery of electrode performance in PEFCs. *Electrochimica Acta* **54,** 2754–2760 (2009).
17. Ghassemzadeh, L. *et al.* Chemical degradation of proton conducting perflurosulfonic acid ionomer membranes studied by solid-state nuclear magnetic resonance spectroscopy. *J. Power Sources* **186,** 334–338 (2009).
18. Osborn, S. J. *et al.* Glass Transition Temperature of Perfluorosulfonic Acid Ionomers. *Macromolecules* **40,** 3886–3890 (2007).
19. Li, Q., He, R., Jensen, J. O. & Bjerrum, N. J. Approaches and Recent Development of Polymer Electrolyte Membranes for Fuel Cells Operating above 100 °C. *Chem. Mater.* **15,** 4896–4915 (2003).
20. Miyake, N., Wainright, J. S. & Savinell, R. F. Evaluation of a Sol-Gel Derived Nafion/Silica Hybrid Membrane for Proton Electrolyte Membrane Fuel Cell Applications: I. Proton Conductivity and Water Content. *J. Electrochem. Soc.* **148,** A898 (2001).
21. Shao, Y., Yin, G., Wang, Z. & Gao, Y. Proton exchange membrane fuel cell from low temperature to high temperature: Material challenges. *J. Power Sources* **167,** 235–242 (2007).

22. Kreuer, K.-D., Rabenau, A. & Weppner, W. Vehicle Mechanism, A New Model for the Interpretation of the Conductivity of Fast Proton Conductors. *Angew. Chem. Int. Ed. Engl.* **21,** 208–209 (1982).
23. Noda, A. *et al.* Bronsted acid-base ionic liquids as proton-conducting nonaqueous electrolytes. *J. Phys. Chem. B* **107,** 4024–4033 (2003).
24. Watanabe, M., Tsurumi, K., Mizukami, T., Nakamura, T. & Stonehart, P. ACTIVITY AND STABILITY OF ORDERED AND DISORDERED CO-PT ALLOYS FOR PHOSPHORIC-ACID FUEL-CELLS. *J. Electrochem. Soc.* **141,** 2659–2668 (1994).
25. W. Zhou, A. S. B. Superprotonic conductivity in MH(PO3H) (M = Li , Na , K , Rb , Cs , NH4). *Solid State Ion.* (2008). doi:10.1016/j.ssi.2008.02.019
26. Haile, S. M., Boysen, D. A., Chisholm, C. R. I. & Merle, R. B. Solid acids as fuel cell electrolytes. *Nature* **410,** 910–913 (2001).
27. Boysen, D. A., Uda, T., Chisholm, C. R. I. & Haile, S. M. High-Performance Solid Acid Fuel Cells Through Humidity Stabilization. *Science* **303,** 68–70 (2004).
28. Traer, J. W. & Goward, G. R. The proton dynamics of imidazole methylphosphonate: an example of cooperative ionic conductivity. *Phys. Chem. Chem. Phys.* **12,** 263–272 (2010).
29. Yan, Z. B., De Almeida, N. E., Traer, J. W. & Goward, G. R. Dynamics of benzimidazole ethylphosphonate: a solid-state NMR study of anhydrous composite proton-conducting electrolytes. *Phys. Chem. Chem. Phys.* **15,** 17983–17992 (2013).

30. Goward, G. Reorientation phenomena in imidazolium methyl sulfonate as probed by advanced solid-state NMR. *Solid State Nucl. Magn. Reson.* **24,** 150–162 (2003).
31. Peng, Z., Morin, A., Huguet, P., Schott, P. & Pauchet, J. In-Situ Measurement of Electroosmotic Drag Coefficient in Nafion Membrane for the PEMFC. *J. Phys. Chem. B* **115,** 12835–12844 (2011).
32. Dippel, T. & Kreuer, K. D. Proton transport mechanism in concentrated aqueous solutions and solid hydrates of acids. *Solid State Ion.* **46,** 3–9 (1991).
33. Boysen, D. A., Chisholm, C. R. I., Haile, S. M. & Narayanan, S. R. Polymer Solid Acid Composite Membranes for Fuel-Cell Applications. *J. Electrochem. Soc.* **147,** 3610–3613 (2000).
34. Połtarzewski, Z. Novel proton conducting composite electrolytes for application in methanol fuel cells. *Solid State Ion.* **119,** 301–304
35. Park, Y.-I. High proton conductivity in ZrP-PTFE composites. *J. Mater. Sci. Lett.* **19,** 1735–1738
36. Xing, P. *et al.* Synthesis and characterization of sulfonated poly(ether ether ketone) for proton exchange membranes. *J. Membr. Sci.* **229,** 95–106 (2004).
37. Manea, C. & Mulder, M. Characterization of polymer blends of polyethersulfone/sulfonated polysulfone and polyethersulfone/sulfonated polyetheretherketone for direct methanol fuel cell applications. *J. Membr. Sci.* **206,** 443–453 (2002).

38. Jones, D. J. & Roziere, J. Recent advances in the functionalisation of polybenzimidazole and polyetherketone for fuel cell applications. *J. Membr. Sci.* **185,** 41–58 (2001).

39. Höhne, G., Hemminger, W. & Flammersheim, H.-J. *Differential Scanning Calorimetry*. (Springer Science & Business Media, 2003).

40. Doyle, C. D. Estimating Thermal Stability of Experimental Polymers by Empirical Thermogravimetric Analysis. *Anal. Chem.* **33,** 77–79 (1961).

41. Loveday, D., Peterson, P. & Rodgers, B. Evaluation of Organic Coatings with Electrochemical Impedance Spectroscopy Part 1: Fundamentals of Electrochemical Impedance Spectroscopy. *JCT Coat. Tech* 46–52 (2004).

42. De Almeida, N. E. & Easton, E. B. Nafion/Sulfonated Silica Composite Membranes for PEM Fuel Cells. *Fuel Cell Membr. Electrode Bind. Mea Perform.* **28,** 29–38 (2010).

Chapter 2
Introduction to Solid-State NMR

This chapter introduces the background for the solid-state NMR techniques that are performed in this thesis. The focus of this chapter is on double quantum filter experiments, which probe proton mobility of salts and salt-polymer composites with and without homonuclear decoupling. Another technique that will be discussed is linewidth analysis that is performed by variable temperature NMR, which can measure the activation energy for a particular motion based on the changes of T_2*. The last major topic will be ^{2}H NMR, which is used to determine hopping rates of proton conductive sites in salts and in salt-polymer composites.

2.1 Introduction

Solid-state NMR is a great tool for investigating structure and dynamics on a localized scale. This technique has the advantage of analyzing materials in the same state of matter as their intended use. For this thesis OSAs and OSA-polymer host materials will be analyzed using solid-state NMR to determine how local structure affects dynamics, which may ultimately lead to a deeper understanding of their suitability for fuel cell applications. NMR linewidths are considerably broader in solid-state NMR than in solution-state NMR due to the lack of fast molecular tumbling which averages nuclear spin interactions such as chemical shift anisotropy, dipole-dipole coupling and quadrupolar coupling. Solid-state NMR tools such as magic angle spinning (MAS) and homonuclear decoupling techniques can narrow linewidths by averaging these interactions. However, these interactions contain valuable information, which is lost in the process. Pulse sequences that reveal ^{1}H-^{1}H dipole-dipole coupled pairs can further

probe the hydrogen-bonded network in materials of interest. This makes solid-state NMR a challenging but highly useful technique in determining local dynamics and structure.

2.2 Spin

Each electron has a spin number associated with it of +1/2 or -1/2 and according to the Pauli exclusion principle each electron is paired with another. Protons and neutrons also have spin numbers of ±½.[1] A proton can cancel the spin from another proton and it is the same with the neutrons. Therefore, it is important to know the number of protons (Z) and neutrons (N) to determine whether a nucleus has an overall spin (I) to be detected by NMR. There are three main cases to determine the overall spin number of a nucleus; when both protons and neutrons are even, when both protons and neutrons are odd and when protons are even and neutrons are odd or vice versa. When the numbers of protons and neutrons are both even (everything paired) the spin is 0, therefore NMR inactive, examples are ^{12}C, ^{18}O and ^{32}S, which also happen to be highly abundant nuclei.[1] When the number of protons and neutrons are both odd (some unpaired) leads to the spin of the nucleus being a whole integer with examples being ^{2}H, ^{14}N and ^{10}B.[1] When protons are even and neutrons are odd (or vice versa) leads to ½ integer value of spin for example ^{1}H, ^{19}F and ^{13}C.[1] For this thesis the focus will be on two nuclei, which are ^{1}H and ^{2}H, with spins of ½ and 1 respectively. Nuclei that have spin I = ½ possess a spherical distribution of charge at the nucleus, whereas any spin >1/2 possesses a non-spherical distribution of charge at the nucleus; the latter are referred to as quadrupolar nuclei.[2] All spins have a different multiplicity of spin states, which is dictated by **Equation 2.1**, where m is the multiplicity of spin states and I is the spin value therefore, ^{1}H possesses two spin states and ^{2}H has three.[1]

$$m = 2I + 1 \quad \textbf{(2.1)}$$

Without an applied magnetic field the direction all spin states are degenerate. In an applied magnetic field the spin states are not degenerate as seen in **Figure 2.1** for I=1/2 and I=1, this effect is called Zeeman splitting.[1,2] The energy that separates the spin states is determined by **Equation 2.2**, where E is the energy between the spin states, m is multiplicity of spin states, γ the gyromagnetic ratio, which is a physical constant specific to a nucleus and B_o is the applied magnetic field.[3]

$$E = m\left(\frac{\gamma h B_0}{2\pi}\right) \quad \textbf{(2.2)}$$

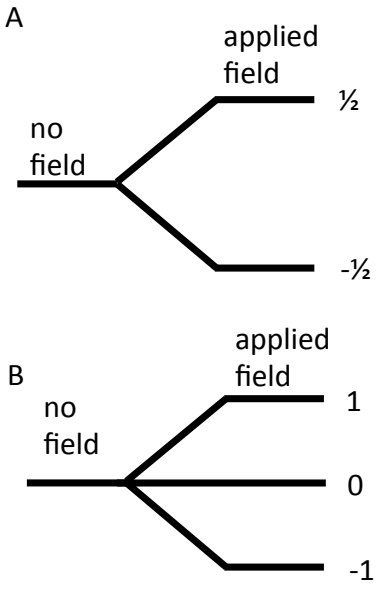

Figure 2.1: Spin states without and with an applied magnetic field. A) Spin ½ B) Spin 1

The populations of the spin states are almost equivalent. This can be shown through the Boltzmann distribution in **Equation 2.3**, where the tiny population difference between the spin states is caused by the gyromagnetic constant (γ, fundamental constant in all nuclei), Plank's constant (h), the applied magnetic field B_o, Boltzmann constant (k) and temperature in Kelvin.[3]

$$\frac{N_{\frac{1}{2}}}{N_{\frac{-1}{2}}} = exp\left(\frac{\gamma h \mathcal{B}_o}{kT}\right) \quad \textbf{(2.3)}$$

This small population difference makes NMR inherently insensitive and thus relatively concentrated samples are required compared to other spectroscopic techniques.[4] However, NMR is incredibly sensitive to the local structure and dynamics, which will be discussed in detail in future sections in this chapter.

2.3 Applying a Radiofrequency Pulse

In section 2.2 it was discussed that NMR active nuclei are populated in spin states in a magnetic field. With the applied magnetic field only a small fraction of nuclei align with the external field in each spin state, however slightly more are aligned with the field. Radiofrequency pulses must be applied at the Larmor frequency of that nucleus (the energy difference in the spin states), which can be determined by **Equation 2.4**, where ω is the Larmor frequency.[3]

$$\omega = -\gamma B_o \quad \textbf{(2.4)}$$

The Larmor frequency for ^{1}H and ^{2}H is given for two different magnetic fields in **Table 2.1** (300 MHz and 500 MHz). A radiofrequency pulse, whose frequency is close to the Larmor frequency of the nuclei of interest, is applied to materials to excite spins into the xy plane. The pulse creates an oscillating field (B_1) that is perpendicular to the applied magnetic field (B_o) which, is described in **Equation 2.5**, where ωI_z relates to the spin interacting with the static field (B_o) and $2\omega_1 cos\omega_{rf} t I_x$ is the spin interacting with B_1, the oscillating field.[5]

$$H_{rf} = \omega I_z + 2\omega_1 cos\omega_{rf} t I_x \quad \textbf{(2.5)}$$

In a typical NMR experiment the nuclei are aligned along z, the static field, and after a pulse move to the xy plane, where they can be detected. Nuclei can be thought of as magnets with north and south poles.[6] When pulsed into the x-y plane the nuclei starts precessing at the Larmor frequency, which creates electrical current. This occurs because each nucleus has magnetic moment. This creates a sinusoidal response represented by the free induction decay (FID); however the length of time this current is present is dependent on the relaxation time of each nucleus. There are four main nuclear spin interactions that can influence this relaxation, which include scalar, chemical shift anisotropy (CSA), dipole-dipole coupling and quadrupolar coupling. For this thesis only CSA, dipole-dipole coupling and quadrupolar coupling are relevant, this will be explained in following section.[7]

Table 2.1: Comparison of ^{1}H and ^{2}H

Isotope	Spin	Gyromagnetic Ratio ($x10^7$ $T^{-1}s^{-1}$)	Natural Abundance	Larmor frequency and Field Strength	
				7.0 Tesla	11.7 Tesla
^{1}H	½	26.75	99.9885	300.0 MHz	500.0 MHz
^{2}H	1	4.11	0.0115	46.1 MHz	76.8 MHz

2.4 Nuclear Spin Interactions

The nuclear spin interactions are described by a Hamiltonian, which is shown in **Equation 2.6**, where the total Hamiltonian is composed of the radiofrequency pulse (H_{rf}), a scalar (H_J), the chemical shift anisotropy (H_σ), dipole-dipole coupling (H_D) and quadrupolar (H_Q).[6]

$$H_{total} = H_{rf} + H_J + H_\sigma + H_D + H_Q \quad \textbf{(2.6)}$$

Each of the nuclear interactions has its own tensor with its own principal axis orientation represented by the following symbols; CSA (σ), dipole-dipole coupling (D) and

quadrupolar coupling (Q). CSA, dipole coupling and quadrupolar coupling will be the only interactions discussed in this thesis because the other interactions are much smaller in magnitude than the interactions presented in this section.

Chemical shift is the result of the external magnetic field (B_o) generating a current in the electron clouds of a molecule.[3] Electron distributions around different types of nuclei are not symmetric creating variable sizes of electrical current. Therefore, different types of chemical shielding are obtained which results in variable chemical shifts. **Equation 2.7** is the Hamiltonian for chemical shielding that can be expressed by an isotropic term and an anisotropic term where, σ_{iso} is the isotropic shift, $\Delta\sigma$ is the chemical shielding anisotropy (CSA), η_{CS} is the asymmetry in chemical shielding and ϕ and θ are polar angles of the chemical shielding tensor relative to the magnetic field.[8]

$$H_\sigma = \gamma\hbar\hat{I_z}B_O\left[1 - \left(\sigma_{iso} + \Delta\sigma(3cos^2\theta - 1 + \eta_{CS}sin^2\theta cos2\phi)\right)\right] \quad \textbf{(2.7)}$$

The isotropic shift, CSA and the asymmetry are further described in **Equations 2.8-2.10**, where σ_{11}, σ_{22}, and σ_{33} are the principal components of the chemical shielding tensor.

$$\sigma_{iso} = \frac{(\sigma_{11} + \sigma_{22} + \sigma_{33})}{3} \quad \textbf{(2.8)}$$

$$\Delta\sigma = \sigma_{33} - \frac{(\sigma_{11} + \sigma_{22})}{2} \quad \textbf{(2.9)}$$

$$\eta_{CS} = \frac{(\sigma_{22} - \sigma_{11})}{(\sigma_{33} - \sigma_{iso})} \quad \textbf{(2.10)}$$

In solution-state CSA, is averaged to narrow isotropic shift, where resonances can be easily identified. For highly shielded nuclei, a nucleus that is not close to highly electronegative atoms has a low chemical shift, whereas nucleus that is close to electron withdrawing nuclei possesses a high chemical shift. In solid-state NMR the CSA is not

averaged and what is observed is a sum of the chemical shift that appears as a shielding powder pattern. This powder pattern changes shape from the orientation of all the nuclei in the sample based on their symmetry. For example, changes in symmetry will change the value of η_{CS} (can be -1 to 1) and thus the resultant powder pattern lineshape. **Figure 2.2** shows four simulated spectra with different asymmetry parameters, η_{CS}=-1 (σ_{22}=σ_{33}) or 1 (σ_{11}=σ_{22}) depicts an axial symmetry and when all the values of tensor are different dictates the shape of the CSA powder pattern. Changes in $\Delta\sigma$ will result in a different width for the lineshape. For this thesis, the focus of study is on ^{1}H and ^{2}H nuclei where CSA does not contribute significantly to linewidths, due to the lack of p orbitals for the electrons. Moreover, CSA effects in ^{1}H spectra are averaged by magic angle spinning, such that only the isotropic chemical shift is observed in most of the spectra included in this thesis.

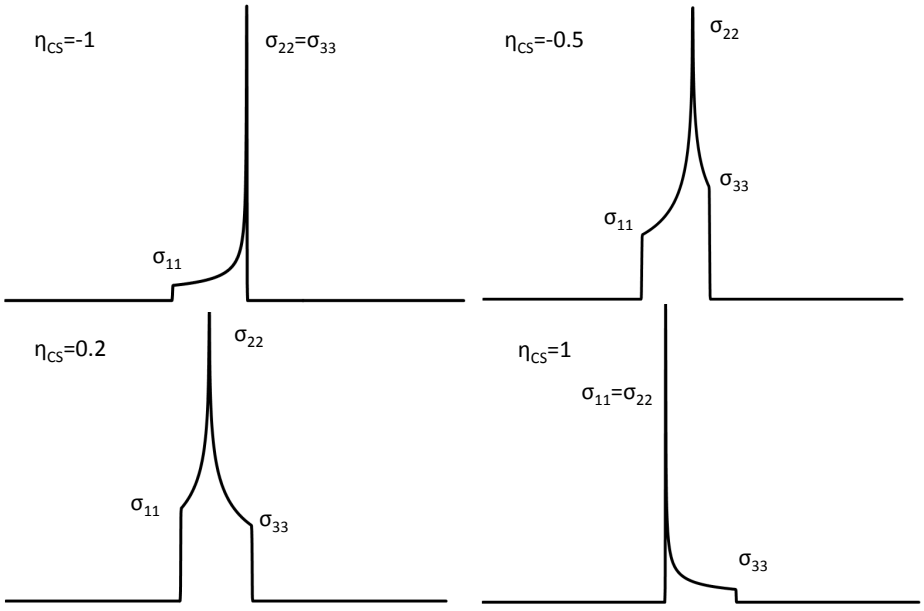

Figure 2.2: Simulated spectra of a spin=1/2 nucleus with different asymmetry parameters

Dipole-dipole coupling is a through space interaction that occurs between nuclei as a result of their magnetic moments. This interaction is based on the gyromagnetic

ratio (γ), the distance between the nuclei (r) and the angler momentum of the spins (I and S) as seen in **Equation 2.11**.[8]

$$H_D = -\sum_{i>j}\left(\frac{\mu_o}{4\pi}\right)\left(\frac{\gamma_i\gamma_j\hbar}{r_{ij}^3}\right) * \frac{1}{2}(3\cos^2\theta - 1)\left[\hat{I}_z\hat{S}_z\right] \quad \textbf{(2.11)}$$

In the solution-state this interaction is completely averaged however, in solid-state this interaction is dominant and is the main interaction that will be probed to study local dynamics of protons in salts and salt-polymer composites in this thesis. In the simplest instance of a spin-pair, the dipole-dipole interaction occurs between a discrete pair of nuclei as seen in **Figure 2.3**. The strength of this interaction depends on the distance between the spins therefore, the smaller the distance between the spins the larger the dipole-dipole interaction.[9] In dipole-dipole coupling of ^{1}H-^{1}H pairs this interaction is large and dominant. This is because protons have the highest gyromagnetic ratio; therefore homonuclear interactions between ^{1}H pairs create broad resonances. For example the two ^{1}H spins in a CH_2 group being ~1.7 Å apart would possess a dipole-dipole coupling of 24 kHz. If this CH_2 group were the only two resonances, the NMR spectrum would show a linewidth of 24 kHz at its full width at half max. However, with organic solids acids and polymer hosts there is large network of ^{1}H that contribute to the dipole-dipole coupling, the total dipole-dipole coupling contributes to the width of the observed peak. In amorphous samples, where there are numerous crystallites within one sample the value of dipole-dipole coupling increases even further than in crystalline samples.

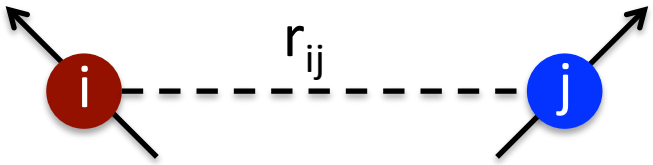

Figure 2.3: Dipole-dipole coupling between spins i and j over distance r.

Quadrupolar interactions are only present in nuclei with spins greater than ½ and are the strongest of all the possible interactions. However, since a quadrupolar nucleus possesses a mulipole nucleus this type of nucleus interacts with the external magnetic fields as well as the local magnetic fields. The Hamiltonian for this interaction is:[5]

$$H_Q = \frac{3C_q}{8I(2I-1)}\left(3cos^2\theta - 1 + \frac{1}{2}\eta_Q sin^2\theta cos2\phi\right)(3I_z^2 - I^2) \quad \textbf{(2.12)}$$

where;

$$C_Q = \frac{e^2 q_{zz} Q}{\hbar} \quad \textbf{(2.13)}$$

$$\eta_Q = \frac{q_{xx} - q_{yy}}{q_{zz}} \quad \textbf{(2.14)}$$

Cq is the quadrupolar coupling constant, η_Q is the asymmetry parameter, q_{xx}, q_{yy} and q_{zz} are the principal components of the quadrupolar tensor and Q is the quadrupolar moment that is specific to each nuclei and is independent of environment.[5] Like CSA the asymmetry parameter changes the shape of the resultant linewidths. The quadrupolar coupling constant changes the width of the observed linewidth. In this thesis, no spin >1/2 quadrupolar nuclei are studied, but Chapter 6 relies on ^{2}H NMR, which is a special case of a spin 1 nucleus. The ^{2}H lineshape is known to be particularly sensitive to motional averaging, therefore the discussion of its properties are given at the end of the chapter, where dynamic effects on NMR spectra are considered.

2.5 T_1 and T_2 Relaxation

There are two main types of relaxation: spin-lattice (T_1) relaxation and spin-spin (T_2) relaxation. After a radiofrequency pulse the spins that were excited to the xy plane relax back to equilibrium. The period of time that this relaxation takes is defined as the spin-lattice relaxation, which is described in **Equation 2.15** where, M_z is the magnetization along z axis, M_o is the magnetization that relaxes back to the z axis and t is time.[10]

$$M_z = M_o\left(1 - \exp\left(\frac{t}{T_1}\right)\right) \quad \textbf{(2.15)}$$

Spin lattice relaxation can change for several reasons such as symmetry or nuclear spin interactions like dipole-dipole coupling. In this thesis T_1 relaxation will be a measure of how dipole-dipole coupling changes in organic solid acids when they are inserted into a polymer host. If there are mobility changes between the salt and polymer the T_1 relaxation will be faster due to dipole-dipole coupling becoming less prominant.[11] Typical values for the T_1 relaxation in ^{1}H samples are on the order of milliseconds to seconds.

Another type of relaxation that typically measured in NMR is $T_1\rho$ that is analogous to T_1, but describes the relaxation along B_1 instead of B_o. This relaxation is measured applying a 90° pulse for the magnetization to be in the xy plane and then applying a spin locking pulse. Overtime, the magnetization that is being held in the xy plane decays and this decay fitted using **Equation 2.16**.[10]

$$M_{xy}(t) = M_o\left[exp\left(-\frac{t}{T_{1\rho}}\right)\right] \quad \textbf{(2.16)}$$

Transverse relaxation (T_2) occurs when the magnetism loses coherence in the xy plane as seen in **Equation 2.16** where, M_{xy} is the magnetization along x or y depending on the phase of the initial excitation pulse and M_o is the initial magnetization.[10]

$$M_{xy}(t) = M_o \left[exp\left(-\frac{t}{T_2}\right)\right] \quad \textbf{(2.17)}$$

This decay in signal is influenced by nuclear spin interactions and is inversely proportional to linewidth. Typical values of T_2 for solution state experiments are on the order of seconds, corresponding to the narrow resonances. The broad resonances observed in solid-state NMR correspond to short T_2 relaxation, which occurs on the order of milliseconds.

In this thesis changes that occur in T_1 and T_2 from impregnation of salts into host materials are attributed to changes in the dipole-dipole coupling.[8,11,12] This is due to the influence of the polymer host on the local ordering of the salt.

2.5 Magic Angle Spinning

As mentioned above lineshapes in solid-state NMR are broad due to the lack of molecular motion to average nuclear spin interactions. Thus methods of averaging these lineshapes are implemented in solid state NMR to narrow these broad resonances. However, before introducing these methods an introduction to contributions to line broadening must be discussed. There are two fundamental types of contribution to linewidth, which are homogeneous and inhomogeneous. In solution-state NMR an example of homogeneous linewidth would be T_2 relaxation, whereas an inhomogeneous would be the instrumental from inhomogeneity of the magnetic field. This inhomogeneity of the field creates a distribution of NMR frequencies resulting in an overall broadening of the linewidth. In solid-state dipole-dipole coupling has a large

impact in line broadening, which is the homogeneous contribution to increase linewidth. If a sample is amorphous, line broadening increases dramatically because the sample is made up of multiple crystal orientations.[6] Only the homogeneous line broadening can be narrowed using solid-state techniques, heterogeneous contributions can never be narrowed. With amorphous samples it does not matter which magnetic field or pulse sequence is used the linewidths, will be always the same due to heterogeneous line-broadening portion.

Equation 2.11 is the Hamiltonian for dipole-dipole coupling, which possesses two main parts; a spatial term and a spin term which both have an angle dependence. Spinning at the magic angle, 54.74°, the $\cos^2\theta$ term is averaged to zero when spinning faster than the interaction.[13] This is achieved by physically spinning a rotor containing a sample at this angle to achieve higher resolution. However, using spinning as stated above only affects homogeneous line broadening, whereas the heterogeneous line broadening remains present. Typical spinning speeds are around 30 kHz but ultrafast spinning upward to 110 kHz has been achieved with specialized probes.

2.5.1 Heteronuclear and Homonuclear Decoupling

Heteronuclear decoupling is a technique that dephases one kind of nuclei while measuring another. The most common type of heteronuclear decoupling is during a cross polarization technique that places a strong pulse on protons during acquisition to detect carbon.[14] Envision a dipole-dipole interaction between spins I and S, where these two different spins are interacting with each other. When you apply a continuous pulse to affect I and observe on S, the dipolar interactions that were previously present are now removed resulting in narrower lineshapes.

In this thesis homonuclear decoupling will be employed to obtain narrow resonances for crystalline samples. However, homonuclear decoupling is difficult since dephasing and observing a signal occur on the same channel since these homonuclear-decoupling sequences will involve multiple pulses. These pulses would rotate the spins around the magic angle to average the spin term of the Hamiltonian for dipole coupling, while still physically spinning the sample to average the space portion. The overall process is called CRAMPS (combined rotational and multiple pulse spectroscopy).[15] There have been several different types of homonuclear-decoupling sequences, where one of the first editions was Lee-Goldburg. A Lee-Goldburg homonuclear decoupling sequence involved two different phased pulses, however this type of sequence involves long high power pulses and can only be implemented for low spinning experiments.[16] The next iteration was the phase modulated Lee Goldburg (PMLG) that allowed for lower power and could be conducted at higher spinning speeds.[17] In this thesis decoupling under mind boggling optimization (DUMBO) is used for homonuclear decoupling which is a similar to PLMG.[18]

2.6 NMR Experiments

2.6.1 Dynamics Measured by Variable Temperature Solid-State NMR

Solid-state NMR can probe local structure through correlation experiments, however this technique can also observe molecular motion. One straightforward method is to use variable temperature solid-state NMR. By using a direct one-pulse experiment on a sample at a varied temperature, information can be obtained. There are three types of motion that can be observed between two or more resonances as seen in **Figure 2.4**, which are slow, intermediate and fast dynamics.[19] The slow dynamic regime occurs when

the rate of chemical exchange is less than the frequency that separates the two resonances.[19] For the intermediate dynamic regime the exchange rate is equal or close to the frequency in between the two resonances. As the exchange rate increases the frequency between the sites reduces as the two resonances come together. The process of coalescence is when the two resonances broaden and combine to a single chemical shift is the process of coalescence.[19] The average chemical shift between the two resonances is observed if both the exchanges rates are equal, otherwise the coalescence shifts to the resonance with the larger population.

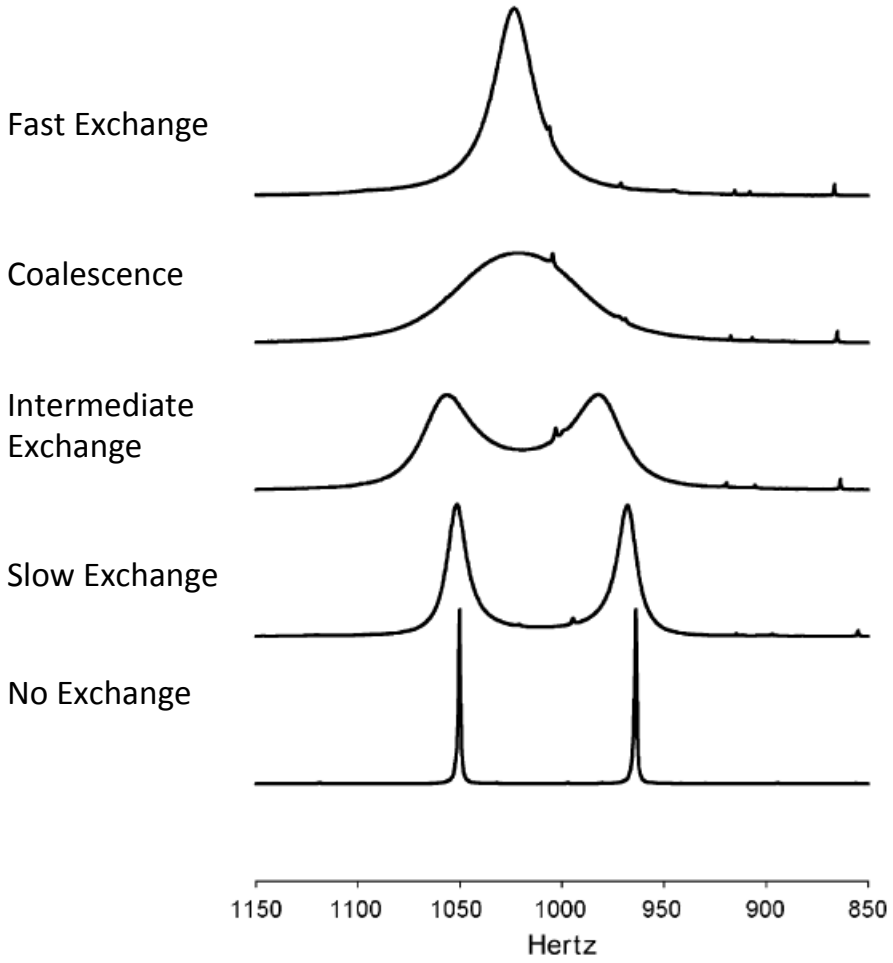

Figure 2.4: Linewidths showing varying chemical exchange as observed with ^{1}H MAS

NMR. Reproduced with permission from Progress in Nuclear Magnetic Resonance Spectroscopy.[19]

In the fast dynamic regime, following coalescence, the resonance becomes a single narrow linewidth. As temperature increases the resonance continues to narrow, where this narrowing effect is due to an increasing T_2*, which is T_2 that is affected by inhomogeneity from imperfect magnetic field on the sample, that is also impacted by nuclear spin interactions. In the case of this thesis, it is assumed that the increasing of T_2* is due to dipole-dipole coupling lessening from higher spin dynamics. T_2* can be determined from the relationship with the full width at half max (FWHM) from deconvolution of the spectrum. From this narrowing being correlated to a time an Arrhenius plot for motion of a particular site can be obtained. The T_2* can be calculated from FWHM (**Equation 2.17**), which is the spin-spin relaxation (T_2) coupled with the effect of field inhomogeneity.

$$FWHM = \frac{1}{\pi T_2^*} \qquad \textbf{(2.18)}$$

An Arrhenius relationship can be extracted from the behaviour of T_2* as a function of temperature.[20] Activation energy can be determined for a localized exchange process and then compared to macroscale techniques such as proton conductivity.

2.6.2 Double Quantum Filter

Broad linewidths are obtained with ^{1}H solid-state NMR due to high dipole-dipole couplings and thus as discussed above MAS and homonuclear decoupling techniques are employed to narrow linewidths. However, dipole-dipole coupling possesses information about dynamics and solid-state structure. By reintroducing dipole-dipole couplings in a

controlled manor information on solid-state structure and dynamics can be obtained. For this thesis proton conductors in salts and salt-polymer composites are being studied by using double quantum filter (DQF) experiments such as back-to-back and POST C7 that reintroduce dipole-dipole coupling to determine mobility and hydrogen bonding on the timescale of the rotor period.[21–23]

This thesis utilizes two different DQF experiments called back-to-back (BaBa) and POST C7. Both of these sequences select for dipole-dipole coupled spin pairs at different timescales. **Figure 2.5A** shows the pulse sequence for BaBa, where the four $\pi/2$ pulses shown must fit within a rotor period, in the incremental excitation and reconversion periods. By incrementing the time periods for excitation and reconversion different strengths of dipole-dipole coupling can be excited. Strong dipole-dipole coupled pairs can be excited with short periods of excitation and reconversion where as weak dipole-dipole couplings require longer times to be fully excited. The BaBa pulse sequence can be used at high speeding speeds and short high-powered broadband pulses can be used. The POST C7 sequence is shown in **Figure 2.5B**.

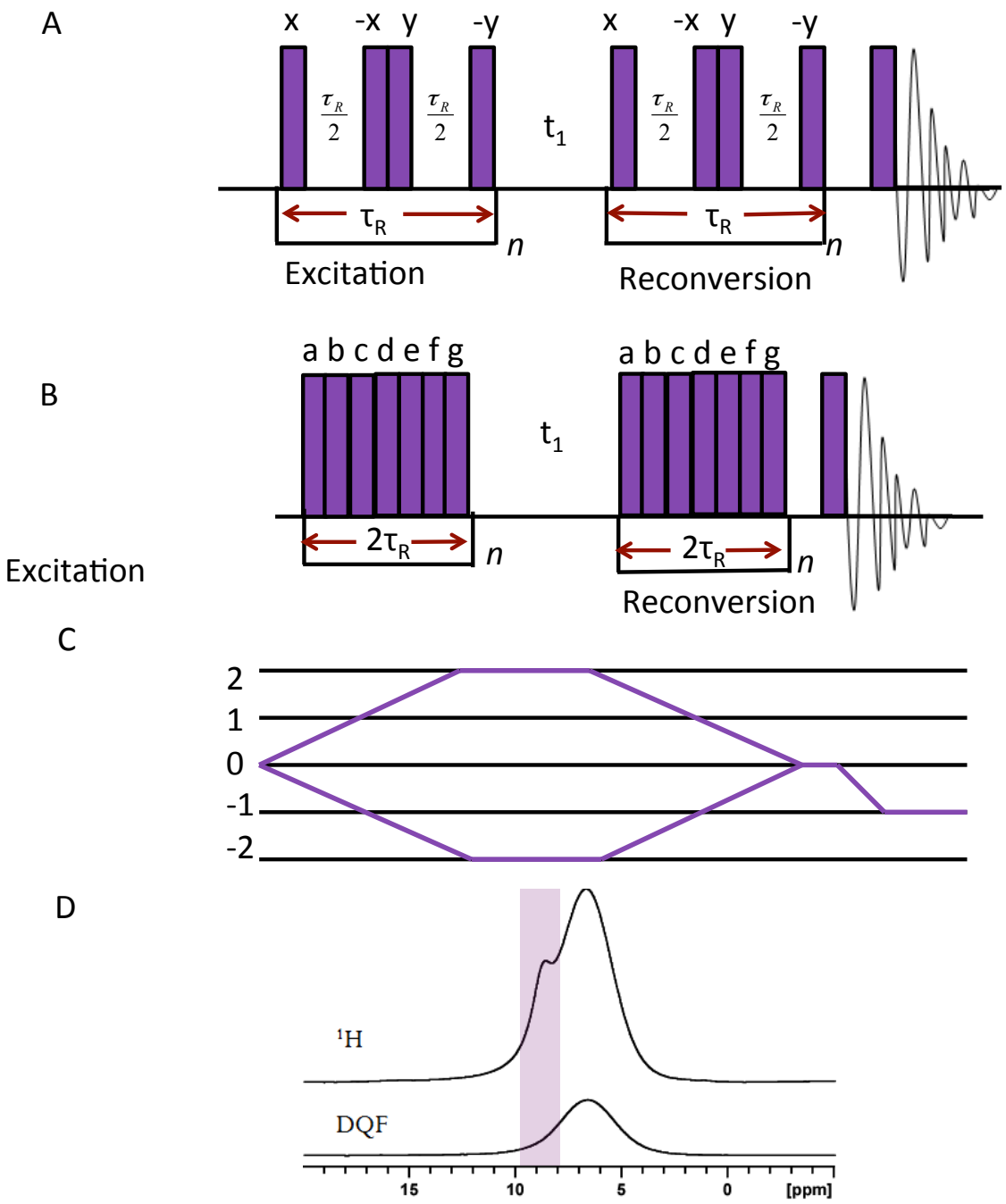

Figure 2.5: A) Back-to-Back pulse sequence, where each rectangle is a 90° pulse B) POST C7 pulse sequence, where each rectangle (or C element) is a composite 360° pulse composed of a 90, 360, 270° pulses. The phases for the pulses are as follows: a) (0/7)2π b) (1/7)2π c) (2/7)2π d) (3/7)2π e) (4/7)2π f) (5/7)2π g) (6/7)2π C) Coherence pathway for a double quantum experiment D) Purple site is completely removed in the DQF spectrum showing that it either possesses no near neighbors or is highly mobile on the timescale of the experiment.[22,24]

In this sequence all 7 of the C-elements (composite 360° pulses) must be applied within two rotor periods, however each rectangle represents a composite 360° pulse that consists of three pulses (90°, 360° and 270°) and each composite pulse has a phase (1/7) of 2π. Therefore this sequence is used at low speeding speeds (12.5 kHz and lower). For example, using a 12.5 kHz spinning speed would require a B_1 of 87.5 kHz since the sequence requires the pulses to have a power level that is seven times the spinning speed which requires the 90° pulse to be 2.86 μs. Therefore, it is impossible to achieve at high spinning speeds with current equipment due the power restrictions. These symmetry-based pulse sequences are designed to select certain dipole-dipole interaction based on average Hamiltonian theory, where the mathematical derivations, which is beyond the scope of this thesis, and is available elsewhere.[24]

BaBa is typically used at high speeding speeds because the power of the pulses does not need to be correlated to its spinning speed. Both sequences required rotor synchronization to reintroduce the dipole-dipole interactions properly. This is how the two different sequences reintroduce dipole-dipole coupling at different recoupling times. POST C7 is used when long recoupling times are required and BaBa is used when shorter times are sufficient to reintroduce the interaction, as the timescale of the recoupling is correlated with the rotor period (τ_R). The choice of sequence is determined from the strength of the interaction that is being probed. It is important to note that since POST C7 requires a slower spinning speed for proper execution, therefore lower resolution is obtained due from the lack of averaging by high speed MAS. Therefore, POST C7 is typically paired with a homonuclear-decoupling sequence to obtain high resolution while reintroducing dipole-dipole interactions.

With 1D DQF experiments resonances that are removed from the spectrum are either mobile or possess no close neighbors on the timescale of the experiment.[25] An example of this is portrayed in **Figure 2.5D**, where the ^{1}H NMR possesses two sites and the ^{1}H DQF NMR only has one from being mobile or having no close neighbors. The 2D DQF experiment reveals a map of dipole-dipole coupled pairs within the sample. For example **Figure 2.6** depict red and blue sites in the direct dimension. In the indirect dimension there are three signals due to a dipole-dipole coupling that exists between spin pairs. In this case there is dipole-dipole coupling between red-red, red-blue and blue-blue. The diagonal crosses through autocorrelations that occur within the sample, however these may not always be observed if there is no coupling within the same site.

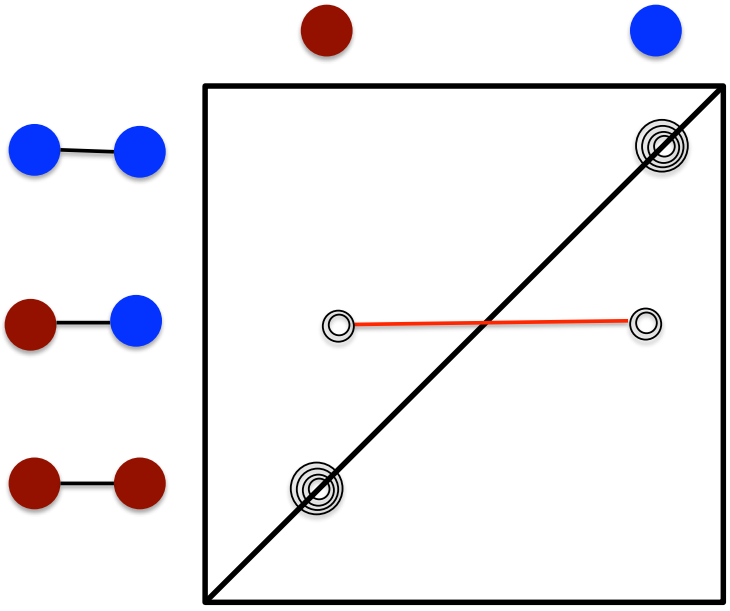

Figure 6: 2D DQF spectrum between red and blue. Correlations are only observed for spins that possess a dipole-dipole coupling.

When implementing DQF sequences the times for recoupling can be lengthened by increasing the number of loops of recoupling in a rotor-synchronized fashion, as shown in **Figure 2.5A** and **Figure 2.5B**. By collecting 2D DQF spectra at different

excitation and recoupling times and integrating each site over time a double quantum coherence (DQC) buildup curve is created.[26] **Figure 2.7** shows two different DQC buildup curves, over the same time period, where the focus of the comparison is based on two factors; the maximum of the DQC buildup curve and the steepness of the curve. When the DQC buildup possesses a steep buildup the coupling between the two resonances is strong, if the curve possesses a shallow buildup the coupling between the two resonances is weak. These double quantum coherence buildup curves can be simulated in SPINEVOLUTION to extract distance and dynamic informtation.[27]

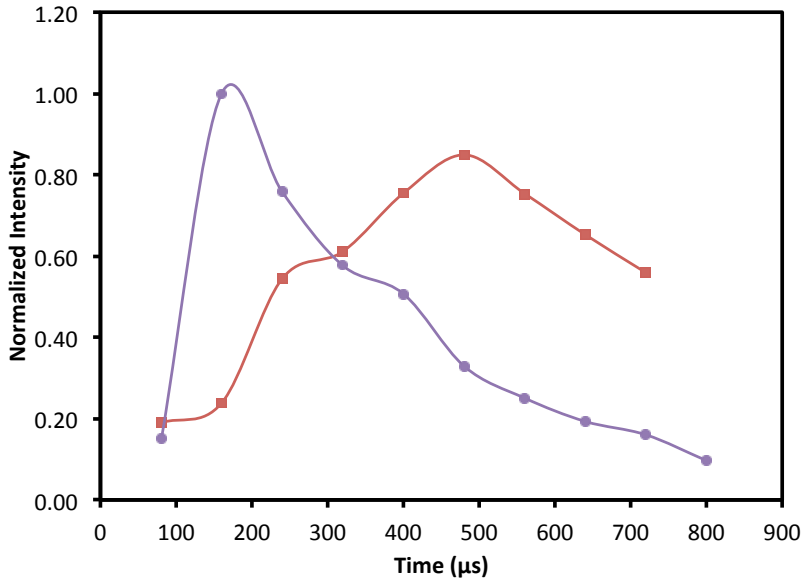

Figure 2.7: Double quantum coherence buildup curved for two different couplings. The purple curve represents a strong dipole-dipole coupling from its steep slope and short time to recouple the spins. The red curve shows a dipole-dipole coupling that is short from its shallow slope and long time to recouple.

1D DQF can be used as a qualitative method to probe mobility in proton conductive samples. 2D DQF experiments are used to create double quantum coherence curves, which typically are used to determine structure based on the relationship between dipole-dipole coupling and to distance. In this thesis, 2D DQF will be used for the first

time to probe dynamics in a sample and to determine possible pathways of proton conduction based on the connections between dipole-dipole coupled pairs.

2.6.3 ^{2}H Static NMR

Double quantum experiments cannot capture all relevant timescales of molecular motion, so in some cases we turn to an alternative, well-known method for probing molecular motion: ^{2}H static NMR. This technique is relevant to samples, with highly mobile proton dynamics that cannot be captured by the above DQF experiments and in cases where high resolution cannot be obtained using techniques that average dipole-dipole coupling. Advantages to this technique are that proton conductive sites are the easiest to exchange with deuterium, thus selective exchange of the peaks of interest can be obtained. Also, heterogeneous line broadening due from these amorphous samples is no longer an issue since this technique is a direct probe to the site of interest.

^{2}H possesses a small quadrupolar constant and is not affected by CSA effects. The static spectrum of ^{2}H portrays two horns (**Figure 2.8**), which occur from the two transitions from its three spin states that ordinate from it being a spin 1 nucleus. Since ^{2}H possesses a small quadrupolar constant the splitting of the horns is on the order of 140-220 kHz therefore, these spectra are sensitive to motion at 10^4 and 10^6 Hz, which is typical in organic solids.[6] **Figure 2.8** shows four different simulated spectra of a three-site rotation for the sulfonate functional group, which participate in proton conduction, at different proton hopping rates. As proton hopping increases the powder pattern lineshapes changes due to an averaging effect. These changes can be fitted with a program called EXPRESS that was written by Robert Vold to extract hopping rates.[28] In order to use EXPRESS to determine hopping rates for a particular sample a few pieces of information

must be known; quadrupolar coupling constant, which can be determined by low temperature static measurements (when there is no dynamics affecting the linewidth), asymmetry (obtained from low temperature), Euler angles of each site and how these sites are connected to each other. Euler angles allow for the rotation of an orientation-dependent interaction such as the quadrupolar interaction into the frame of the molecular structure.

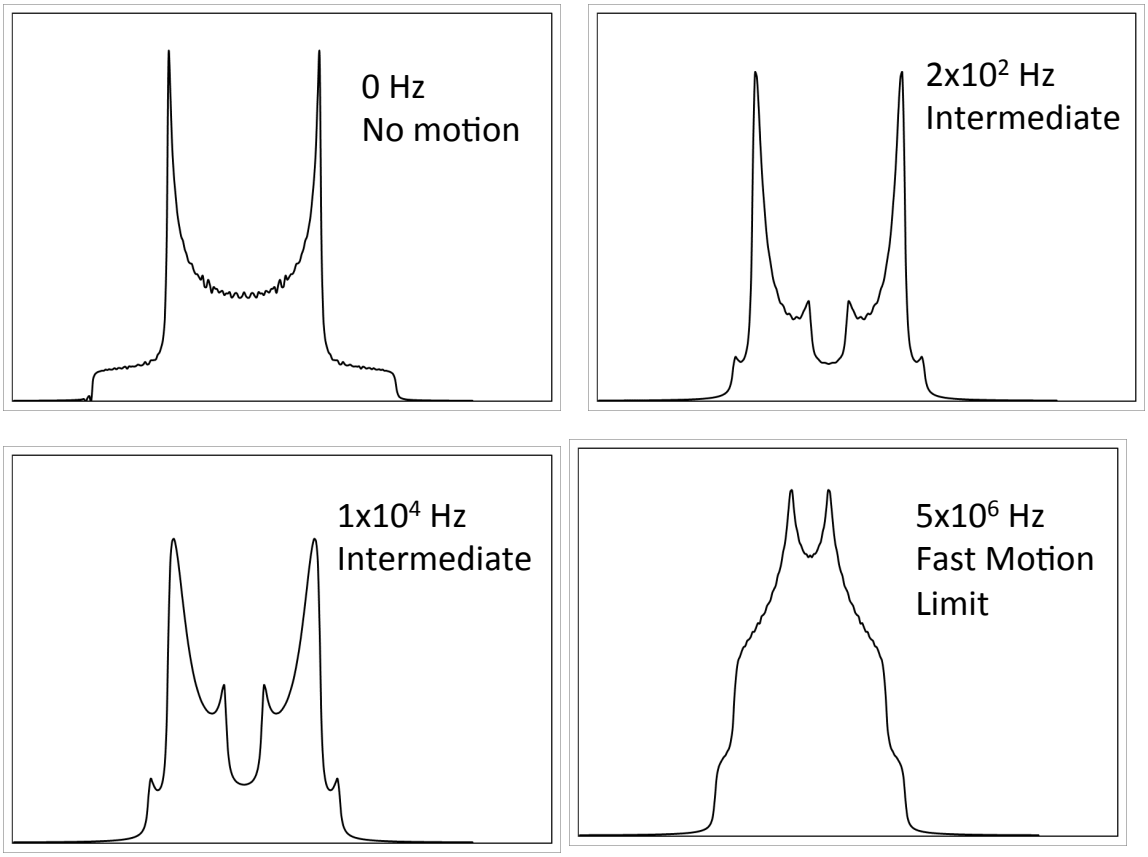

Figure 2.8: Three-site rotation at different rates simulated in EXPRESS

Utilizing these parameters, the influence of specific molecular motions on the ^{2}H lineshape can be calculated. In this thesis we employ ^{2}H NMR to characterize the ion transport pathways in the solid acid IFMS, and the host polymer, SPEEK. We then extend this to characterize the ion dynamics in the salt-polymer composites, as described in chapter 6.

2.7 Timescales and Dynamics

Each of the experiments discussed above probe their own range of molecular dynamics. For experiments that measured relaxation such as T_1 and $T_1\rho$ molecular motion can be probed on the scale of milliseconds to seconds. However, relaxation that was measured as function of signal decay (T_2) is typically on the order of μs. DQF experiments probe motion that occurs within the rotor period of the specific experiment. With the sequence Back-to-Back the timescale is on the order of 40-100 μs and with POST C7 is on the order of 80-800 μs. For example, an isolated spin pair separated by 1.4 Å has a dipole-dipole coupling of 24 kHz, which would require motion of 40 μs to average that would be at the lower limit of detection for Back-to-Back and immeasurable for POST C7, therefore these pulse sequences are appropriate for multi-pair dipole-dipole coupled systems. Lastly, ^{2}H NMR probes motion that can average the powder pattern observed, which is typically 140-220 kHz, which allows motion on the order of 1-100 μs to be observed. All of the above techniques are highly sensitive to motion in the ranges stated and are used throughout this thesis to determine motion that occurs at different timescales.

2.8 Summary

Solid-state NMR is a powerful tool in measuring local dynamics to determine mobility. In chapter 3, ^{1}H MAS NMR at variable temperature will be used to determine differences in Nafion casted with different thicknesses and how T_2 can be used to determine the rate of exchange for the H-bonded protons. Chapter 4 uses DQC buildup curves to investigate dynamics in organic solid acids rather than the more typical structure determination. In chapter 5, 1D DQF is used to qualitatively investigate how dynamics changes from the salts themselves to salt-Teflon composites. ^{1}H 1D MAS

variable temperature experiments are used to quantify how the activation energy of proton changes from the salt itself to salt-composite form. Chapter 6 utilizes ^{2}H NMR to determine hopping rates as well as mechanism for proton transport on organic solid acids in sulfonate-functioned hydrocarbon hosts. These techniques are shown to effectively characterize proton-conducting materials and to correlated molecular-level dynamics with performance.

2.8 References

1. Macomber, R. S. *A complete introduction to modern NMR spectroscopy*. (Wiley, 1998).
2. Duer, M. J. *Introduction to Solid-State NMR Spectroscopy*. (Wiley, 2005).
3. Levitt, M. H. *Spin Dynamics: Basics of Nuclear Magnetic Resonance*. (Wiley, 2001).
4. Pavia, D. L., Lampman, G. M. & Kriz, G. S. *Introduction to Spectroscopy: A Guide for Students of Organic Chemistry*. (Harcourt College Publishers, 2001).
5. Duer, M. J. *Solid State NMR Spectroscopy: Principles and Applications*. (Wiley, 2001).
6. Apperley, D., Harris, R. & Hodgkinson, P. *Solid-State NMR: Basic Principles and Practice*. (Momentum Press, 2012). at <http://www.momentumpress.net/books/solid-state-nmr-basic-principles-and-practice>
7. Keeler, J. *Solid-State NMR Lecture Notes*. (1998).
8. Schmidt-Rohr, K. & Spiess, H. W. *Multidimensional Solid-state NMR and Polymers*. (Academic Press, 1994).

9. Brown, S. P. Applications of high-resolution 1H solid-state NMR. *Solid State Nucl. Magn. Reson.* **41,** 1–27 (2012).

10. Freeman, R. & Hill, H. D. W. Fourier Transform Study of NMR Spin--Lattice Relaxation by ``Progressive Saturation''. *J. Chem. Phys.* **54,** 3367–3377 (1971).

11. Yan, Z. B., De Almeida, N. E., Traer, J. W. & Goward, G. R. Dynamics of benzimidazole ethylphosphonate: a solid-state NMR study of anhydrous composite proton-conducting electrolytes. *Phys. Chem. Chem. Phys.* **15,** 17983–17992 (2013).

12. Ye, G., Hayden, C. A. & Goward, G. R. Proton dynamics of nafion and Nafion/SiO2 composites by solid state NMR and pulse field gradient NMR. *Macromolecules* **40,** 1529–1537 (2007).

13. Andrew, E. R. Magic Angle Spinning. *Int. Rev. Phys. Chem.* **1,** 195–224 (1981).

14. Pines, A., Gibby, M. G. & Waugh, J. S. Proton-enhanced NMR of dilute spins in solids. *J. Chem. Phys.* **59,** 569–590 (1973).

15. Gerstein, B. C. in *eMagRes* (John Wiley & Sons, Ltd, 2007). at <http://onlinelibrary.wiley.com/doi/10.1002/9780470034590.emrstm0100.pub2/abstract>

16. Madhu, P. K. High-resolution solid-state NMR spectroscopy of protons with homonuclear dipolar decoupling schemes under magic-angle spinning. *Solid State Nucl. Magn. Reson.* **35,** 2–11 (2009).

17. Leskes, M., Madhu, P. K. & Vega, S. Supercycled homonuclear dipolar decoupling in solid-state NMR: Toward cleaner [sup 1]H spectrum and higher spinning rates. *J. Chem. Phys.* **128,** 052309 (2008).

18. Sakellariou, D., Lesage, A., Hodgkinson, P. & Emsley, L. Homonuclear dipolar decoupling in solid-state NMR using continuous phase modulation. *Chem. Phys. Lett.* **319,** 253–260 (2000).

19. Bain, A. D. Chemical exchange in NMR. *Prog. Nucl. Magn. Reson. Spectrosc.* **43,** 63–103 (2003).

20. Celik, S. U., Akbey, U., Graf, R., Bozkurt, A. & Spiess, H. W. Anhydrous proton-conducting properties of triazole-phosphonic acid copolymers: a combined study with MAS NMR. *Phys Chem Chem Phys* **10,** 6058–66 (2008).

21. Brown, S. P., Lesage, A., Elena, B. & Emsley, L. Probing Proton−Proton Proximities in the Solid State: High-Resolution Two-Dimensional 1H−1H Double-Quantum CRAMPS NMR Spectroscopy. *J. Am. Chem. Soc.* **126,** 13230–13231 (2004).

22. Brown, S. P. & Spiess, H. W. Advanced solid-state NMR methods for the elucidation of structure and dynamics of molecular, macromolecular, and supramolecular systems. *Chem. Rev.* **101,** 4125–4155 (2001).

23. Traer, J. W. & Goward, G. R. The proton dynamics of imidazole methylphosphonate: an example of cooperative ionic conductivity. *Phys. Chem. Chem. Phys.* **12,** 263–272 (2010).

24. Brinkmann, A. & Levitt, M. H. Symmetry principles in the nuclear magnetic resonance of spinning solids: Heteronuclear recoupling by generalized Hartmann–Hahn sequences. *J. Chem. Phys.* **115,** 357–384 (2001).

25. Brown, S. P., Schnell, I., Brand, J. D., Müllen, K. & Spiess, H. W. A 1H double-quantum magic-angle spinning solid-state NMR investigation of packing and

dynamics in triphenylene and hexabenzocoronene derivatives. *J. Mol. Struct.* **521,** 179–195 (2000).

26. JP, B., C, T., C, F. & SP, B. Determining relative proton-proton proximities from the build-up of. *Phys Chem Chem Phys* **11,** 6941 (2009).

27. M, V. & RG, G. -SPINEVOLUTION: a powerful tool for the simulation of solid and liquid state NMR. *J Magn Reson* **178,** 248–282 (2006).

28. Hahn, E. L. Spin Echoes. *Phys. Rev.* **80,** 580–594 (1950).

29. Vold, R. L. & Hoatson, G. L. Effects of jump dynamics on solid state nuclear magnetic resonance line shapes and spin relaxation times. *J. Magn. Reson.* **198,** 57–72 (2009).

Chapter 3
^{1}H Solid State NMR Study of Nanothin Nafion Films

This manuscript is published in the Journal of Physical Chemistry C. The co-authors of this paper are D.K. Paul, K. Karan and G.R. Goward. D.K. Paul synthesized the thin and ultra-thin films and performed the macroscale measurements, which included thickness, EIS and water uptake under the supervision of K. Karan. I performed all the solid-state NMR that is detailed in this chapter. I initially wrote the manuscript and it was edited by all the co-authors as well as myself.

Within a fuel cell the anode is a highly reducing dry environment and on the cathode side is an oxidizing wet environment. The polymer electrolyte must be able to withstand both of these conditions. The industry standard is Nafion, however when dried the polymer cannot conduct protons effectively. On the anode Nafion is quite dry and water is unable to diffuse throughout the whole polymer to maintain complete hydration. Therefore, if the polymer were thinner to allow for full diffusion would be an asset. In this chapter two different thicknesses of Nafion are studied a 160 nm (thin) and 10 nm (nanothin) films. As the polymer thickness decreases the water content increases, which also lowered proton conductivity. The chapter is using solid-state NMR to probe if this is a result of local dynamic changes or effects in long-range transport.

3.1 Introduction

Nafion® is a well-known copolymer made of a fluorocarbon backbone with a sulfonic acid terminated perfluorovinyl ether side-chains as seen in **Figure 3.1**. It is commercially available with 10% degree of sulfonation and different equivalent weights (EW), defined as average mass of the polymer per sulfonic acid group. The most

commonly form of Nafion is 1100 EW available either as a dispersion or as a membrane. Where the latter is available in various thicknesses. Nafion 117 implies a membrane of EW 1100 and thickness of 7 mil (or 7 thousandth of an inch).[1] Nafion has numerous applications such as polymer electrolyte fuel cells (PEFCs), methanol fuel cells, and water electrolyzers.[2,3] For these applications, Nafion is typically a free standing film with thicknesses of >25 μm and is considered to be the benchmark material for polymer electrolytes. A key functional property of Nafion in these applications is proton conduction between the anode and the cathode. Nafion also exists in the porous composite electrodes of these devices serving the same functionality of providing a pathway for protons to arrive at or leave the electro-catalyst surface. In PEFC electrodes or catalyst layers, Nafion exists as a 4-10 nm thin film covering the aggregates of Pt/C catalyst.[4] Whereas the free-standing films (>25 μm) have been intensely studied over the past decades, the structure and properties of sub-micron thin, supported Nafion films are only now begun to be explored in sufficient depth. Here, we define thin films as those possessing thicknesses greater than 100 nm but less than 1 μm and ultra-thin films as those with thicknesses less than 100 nm.

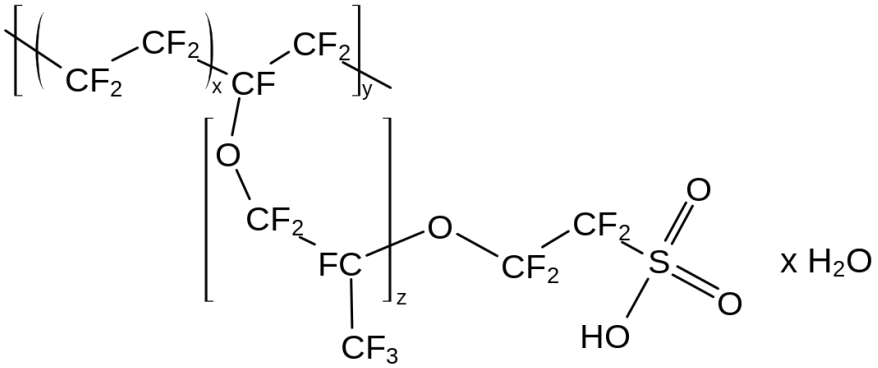

Figure 3.1: Structure of Nafion 1100 (x=6, Z=1)

There is growing evidence that the structure and properties of ultra-thin films differ from the membrane form of Nafion.[5–7] Diverse techniques including neutron reflectometry, atomic force microscopy, contact angles and ellipsometry have been employed to probe different structural aspects and properties of thin and ultra-thin films.[5,6,8] A highly suppressed conductivity of nanometer thin films was reported by Siroma *et al.*, and recently by Paul *et al.* for self-assembled films, both prepared on SiO_2 substrate.[9–11] As summarized in **Table 3.1**, the conductivity of ultra-thin 10 nm and thin 160 nm Nafion films on SiO_2 substrates are highly suppressed compared to the membrane form. Conductivity in the perfluorosulfonic ionomer is known to correlate with water content and it may be expected that the low conductivity in ultra-thin Nafion films is due to low water content.[5] However, from water uptake measurements, expressed in terms of number of water molecules per sulfonic acid group (represented as λ), it can be noted that the low water content is likely not the cause for observed low ionomer conductivity for thin films. This opens up the question as to why or what factors are responsible for the low conductivity in these Nafion thin/ultra-thin films. As discussed by Eikerling *et al.*, on a fundamental level, for Nafion-type ionomers, the overall membrane conductance is determined by the interplay between the mobility mechanisms, the charge distribution inside pores, and the pore microstructure.[12] The latter two factors depend on the internal structure of the membrane/films, i.e. the local pore structure and the long-range interconnectivity of the pores. Further, the mobility may be a function of the local pore structure, which is also a function of water content. The macroscopic conductivity can be described as the product of three factors; intrinsic mobility (m_{H+}), charge carrier

concentration (C_{H+}) and a structural factor that accounts for porosity (e_w) and tortuosity (t) as seen in **Equation 3.1**.

$$\sigma = \mu_{H+} \cdot C_{H+} \cdot f(\varepsilon_w, \tau) \quad \textbf{(3.1)}$$

Table 3.1: Relative humidity dependent proton conductivity and water uptake of 10nm and 160 nm Nafion® ionomer films on SiO_2 at 25 °C.

	10 nm		160 nm		Nafion117	
Relative Humidity	σ (mS.cm^{-1})[a]	λ[b]	σ (mS.cm^{-1})[a]	λ[b]	σ (mS.cm^{-1})[c]	λ[d]
20	0.0002	33	0.336	3	2.4	2
40	0.020	34	3.25	3	10	3
60	0.41	43	8.31	5	19	4
80	7.8	52	27.1	8	40	6
95	23.9	59	54.0	12	65	13

[a]Paul *et al*[22], [b]Modestino *et al*[6], [C]Sone *et al.*[23],[d] Zawodzinski *et al.*[24]

To resolve the difference in conductivities between bulk membrane and thin films, all three factors must be known. Unfortunately, even for the well-studied free-standing form of Nafion, there are ongoing debates about the pore structure.[13] Nonetheless, the evidence of difference in the internal structure and property between Nafion thin films and membranes is emerging. For example, the absence of ionic domains in 4-10 nm Nafion films were noted from GISAXS (Glancing Incident Small Angle X-ray Scattering) measurements whereas thicker films showed 4-5 nm ionic domain.[5] In related work, water diffusivity measurements using polarization-modulation infrared reflection absorption spectroscopy (PM-IRRAS) on Nafion films of thickness ranging 20-220 nm revealed that sub-60 nm films possess highly depressed diffusivities compared to

thicker films.[7] Similarly, the surface wettability of sub-55 nm and thicker Nafion films differed where hydrophilic surfaces were reported with for thinner films and hydrophobic surface for thicker films on SiO_2.[6] While these findings have highlighted the differences in the structure and properties between ultra-thin, thin and freestanding membranes of Nafion, there has been no direct study of proton mobility in ultra-thin/thin Nafion films. Solid- state NMR (^1H) is a well-established tool for characterizing dynamics, and is able to provide direct information regarding the local proton mobility or ion hopping. However, studies of such thin films are challenging due both to the difficulty in fabricating reproducible nanothin films (homogeneous with respect to thickness and structure) and to the challenges of low signal to noise.

In this study, solid-state ^1H NMR characterization of 10 nm ultra-thin and 160 nm thin Nafion films on SiO_2 substrate is reported. It is important to note that NMR measurements on such thin Nafion films (10 nm) are unprecedented and required substantial effort to develop a suitable experimental protocol. Fortunately, the comparatively high receptivity of the ^1H nucleus allows for the detection of protons, even in these extremely thin films. NMR measurements were performed at different temperatures and relative humidity (RH) conditions to extract the activation energy and compare with available data on the long-range proton transport as determined by impedance spectroscopy measurements on the nanothin films. Here we utilize a combination of ^1H transverse relaxation (T_2) properties, and chemical shift trends, both measured as a function of temperature and RH, to scrutinize the difference between these two types of Nafion films. Within the Nafion films, the dominant mechanism of ^1H T_2-relaxation is homonuclear dipolar couplings among the protons in the water/acidic proton

domains. Increasing local mobility, which changes internuclear distances, and the orientation between spin pairs, readily averages the dipolar couplings in a H-bonded network. Therefore, differences in the T_2 behaviour may be used as a measure of the difference in local dynamics in the hydrogen-bonded domains. Trends in line width (which are proportional to $1/T_2^*$) as a function of temperature have been shown to correlate with the trends in macroscopic conductivity.[14] In this case, due to the very subtle differences between the samples of interest, we have implemented Hahn echo measurements to directly measure T_2, and eliminate any influence of local field inhomogeneity on the observed relaxation properties.[15]

In addition to monitoring relaxation properties, the chemical shift trends of the single observable peak in these spectra are attributed to changes in the strength of the local H-bonding network.[16] A trend to lower chemical shift is attributed to increasing local dynamics, as the H-bonding network loosens allowing higher mobility to occur.

3.2 Experimental

3.2.1 Nafion Dispersion Preparation

Commercially available 5 wt % Nafion (EW 1100) solution in water–alcohol mixture (75/20 w/w alcohol to water) acquired from Ion Power (USA) was used. Like prior studies, the stock dispersion was diluted to desired Nafion concentration by isopropyl alcohol.[7,9,17,18] Nafion solutions of concentration 0.25 and 3.0 wt % were prepared by adding appropriate amount of isopropyl alcohol (Sigma-Aldrich) to the stock 5 wt % Nafion solution. The diluted solution was equilibrated at least 24 h after initial 5 min sonication. Dilution followed by long equilibration time was allowed to bring the high aggregation state to its lower aggregation state.

3.2.2 Substrate Cleaning

Silicon wafer with a 300 nm thermally grown in both side of SiO_2 layer (MTI, USA) was selected as a model substrate. The cleaning of SiO_2/Si wafers involved multiple steps. First, the wafer was exposed to a Piranha (Caution!) solution (H_2SO_4:H_2O_2; 7:3) at 80–90 °C for 1 h to remove surface contamination. Next, the wafer was rinsed with Millipore water and dried under flow of compressed air. Subsequently, the wafer was placed into an RCA (Radio Corporation of America) cleaning solution mixture (DI H_2O:NH_4OH:H_2O_2; 5:1:1) at 70–80 °C for 30 min to remove organic contaminants from the surface. Finally, the wafer was washed by Millipore water several times and dried again under flow of compressed air. The cleanliness of the wafer was confirmed by AFM and XPS analyses.

3.2.3 Film Fabrication by Self-Assembly

Nafion thin films were generated by a self-assembly method onto cleaned SiO_2/Si substrate. The cleaned substrate was immersed in the Nafion solution of known concentration contained in a capped beaker. The substrate was exposed to Nafion solutions for 12 h or otherwise specified time. After carefully removing the substrate from the solution it was dried under a flow of dry air. Vacuum drying was carried out in low vacuum (−30 in. of Hg) at 40 °C for 16–20 h.

The dry film thicknesses were measured on the similar 300 nm SiO_2 terminated Si wafer but on a larger dimension (1 cm x 1 cm) sample by three different techniques; AFM, ellipsometry, and XPS.[5] The three techniques yielded thicknesses by examining sample area over three different length scales; a line scan over a micron long region by AFM, 50 micron diameter spot by ellipsometry and a few mm^2 areal region probed by XPS.

Further, homogeneity of film thickness and morphology was characterized by AFM topography, phase contrast image and calculated roughness as described by Paul et al.[5]

3.2.4 Solid-State NMR

The 160 nm and 10 nm films of Nafion were prepared, following the procedure described above, on 5 mm circular disks of Si wafer terminated with 300 nm thick SiO_2. Fourteen disks were placed into a 7 mm rotor with powdered Teflon in between each layer. The rotors were then placed in a humidity chamber to equilibrate for 24 hours. Afterwards the rotor was capped, to maintain a constant lambda within the rotor during variable temperature ^{1}H MAS NMR experiments. The samples were spun only to 800 Hz due to stability in spinning and the weight of the rotor. As a control Teflon was packed in a rotor and humidified to 95%, where no ^{1}H signal was obtained. Therefore, any dynamics observed due to humidification is due to the films and not due to the packing material. NMR measurements were performed on an Avance Bruker 500 MHz spectrometer. Pulses used were calibrated to 7 μs for the 90° pulse with a 2 s delay between pulses. All ^{1}H NMR shifts were calibrated to the adamantane ^{1}H chemical shift of 1.84 ppm, acquired at 5 kHz MAS. Variable temperature experiments were conducted in the 300-350 K range and temperature achieved by heating the bearing gas. Transverse magnetization relaxation measurements were conducted using a Hahn echo pulse sequence. This sequence uses an initial 90° pulse followed by a delay and 180° pulse with acquisition at the peak of the echo achieved using a synchronized delay. The delays were incremented through 16 steps between 30-630 μs. Hahn echo data was analyzed to evaluate the relaxation rate, T_2, from the intensity of each FID after magnitude correction, a single exponential fit the data to extract T_2.

3.3 Results and Discussion

3.3.1 Solid-State ^{1}H NMR

Solid-state NMR of protons is inherently sensitive, due to the high gyromagnetic ratio of the ^{1}H nuclei. However, ultimately the number of nuclei within the NMR coil determines the sensitivity of the experiment. This makes the particular configuration of nanothin films coated on silicon wafers particularly challenging, as the bulk of the sample holder is filled with inactive material. In most cases this would be alleviated by simply increasing the thickness of the coating upon the substrate, however in this case, it is particularly the nanothin nature of the film, which is of physical interest. Thus, we spent a great deal of effort on experimental design, to ensure the viability of the experiment. We established that a static measurement of a stack of rectangular wafers was in fact sensitive to the orientation of the wafers within the magnetic field, resulting in chemical shift changes with orientation. This is a well-known effect for single crystals, and implies a degree of orientational preference for the hydrated domains within the nanofilms. To overcome this difficulty, and ensure the reproducibility of the chemical shift measurements, we modified the sample preparation to take advantage of the full rotor volume, and to enable modest magic angle spinning, simply to achieve sufficient averaging to overcome position-dependent chemical shift or linewidth changes.

3.3.1.1 Transverse Relaxation (T_2) Measurements

Figure 3.2 shows an example transverse relaxation data set, which was measured using a series of ^{1}H Hahn echoes, as a function of both film thickness and temperature. The delay between the pulses is incremented, and the signal intensity decreases exponentially; subsequently this decay is modeled using a single exponential to determine T_2. The fit of the T_2 decay is of very high quality and the spectra collected were of a high

signal/noise ratio in spite of the minute amount of sample present in the rotors. Even the 160 nm film, on a stack of 10 disks, would only have a total hydrated sample mass of ~60 μg. In contrast, a typical solid-state ^{1}H NMR experiment on an organic solid would be performed with 10 mg of active material. The challenging experiment attempted here is made feasible by the high sensitivity and receptivity of the ^{1}H nuclei, and careful, deliberate setting of the NMR parameters (stable spinning speed, accurate pulse lengths). This demonstrable sensitivity is promising for any future solid-state NMR experiments on ionomers in catalyst layers due to the similar amounts of active material being present.

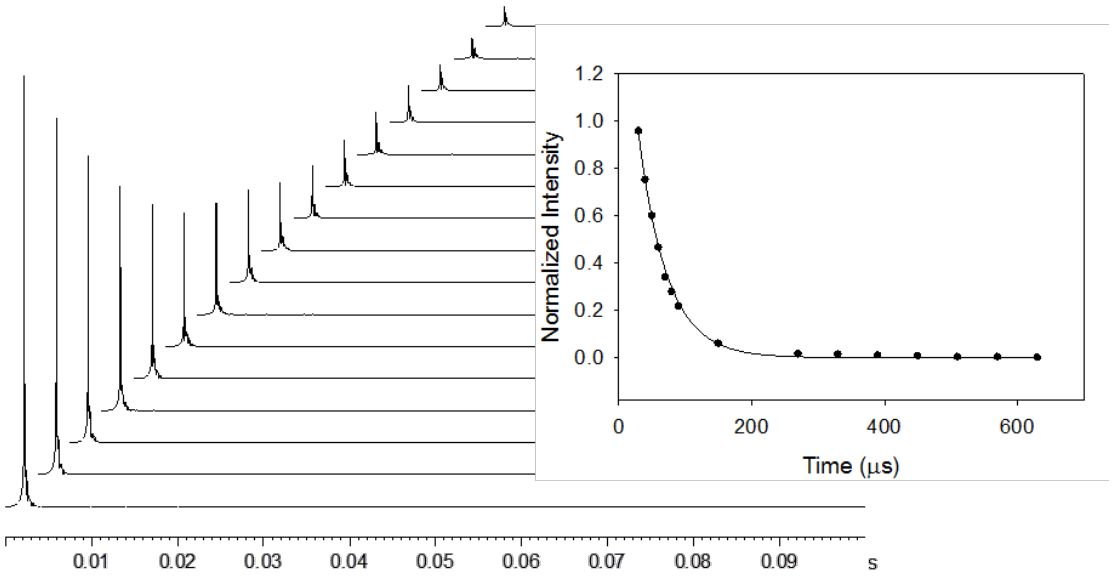

Figure 3.2: Stack plot of ^{1}H Hahn echo free induction decays, presented in magnitude mode to show the change of intensity. Delay times were incremented from 30μs to 630 μs delays. Example data is shown for the 10 nm thin film at 300 K and 60 % RH. The intensity of each FID is plotted against the incremented delay and is modeled using a single-exponential decay function. T_2 was determined to be 44.7±3 μs in this instance.

The ^{1}H Hahn echo method was applied to the ultra-thin and thin films as a function of relative humidity and temperatures. The T_2 values extracted from these datasets are plotted in **Figure 3.3**. The samples were equilibrated to the same relative humidity and, once equilibrated and sealed within the rotor, the value of lambda was

assumed to be constant with increasing temperature. For both the ultra-thin and the thin films, the T_2 was the same within error at all temperatures and humidities performed. It is concluded that the local proton dynamics in both films are in the fast exchange limit.[19] Since both the ultra-thin and thin films have similar behaviour with T_2 measurements, data provided by this technique is not able detect the differences in proton mobility. This is a first indication that the NMR reveals a strong similarity in the local proton dynamics, hinting that a more long-range structural difference may give rise to the different macroscopic behaviours. Moving beyond ^{1}H T_2 measurements, the trends of chemical shift as a function of temperature are monitored, as a measure of changing local environments, and an increasingly loose hydrogen-bonding arrangement.[20]

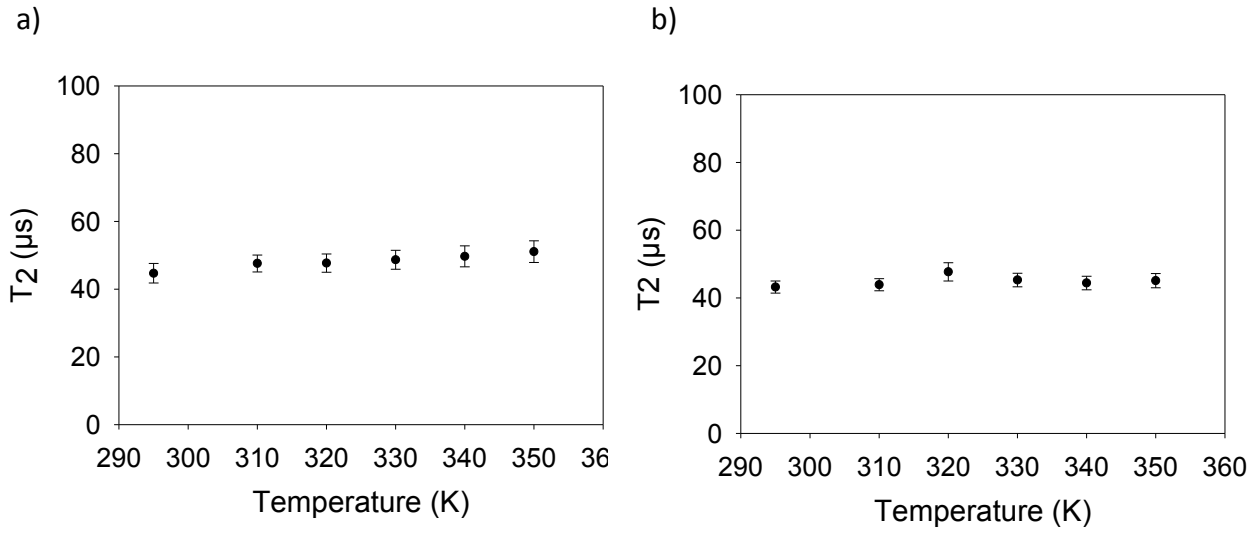

Figure 3.3: ^{1}H Variable Temperature NMR T_2 Hahn echo, Static, 7 mm rotor, 500 MHz a) 10 nm Nafion Thin Film λ=45 b) 160 nm Nafion Thin Film λ=5.

3.3.1.2 Shift Trends in ^{1}H NMR

A previous study showed that the ^{1}H chemical shift and linewidth in Nafion are highly responsive to water content.[21] As shown by Ye *et al.,* fully dehydrated Nafion possess a broad peak at a high chemical shift, whereas fully hydrated Nafion exhibits a

narrow peak at lower chemical shift.[21] **Figure 3.4** illustrates the chemical shift trends for both the ultra-thin and thin Nafion films. Both the ultra-thin and thin films follow trends observed with bulk Nafion, where the resonance at high water content occurs at a low chemical shift and moves toward higher chemical shift with decreasing humidity. One main difference between the ultra-thin and thin films is their ^{1}H chemical shift. The ultra-thin Nafion film possesses a higher chemical shift overall than the thin film indicating that the H-bonded network is bound more tightly than in the thin Nafion film. This is the first evidence that there is a measurable difference in the local dynamics between both films observed by ^{1}H NMR.

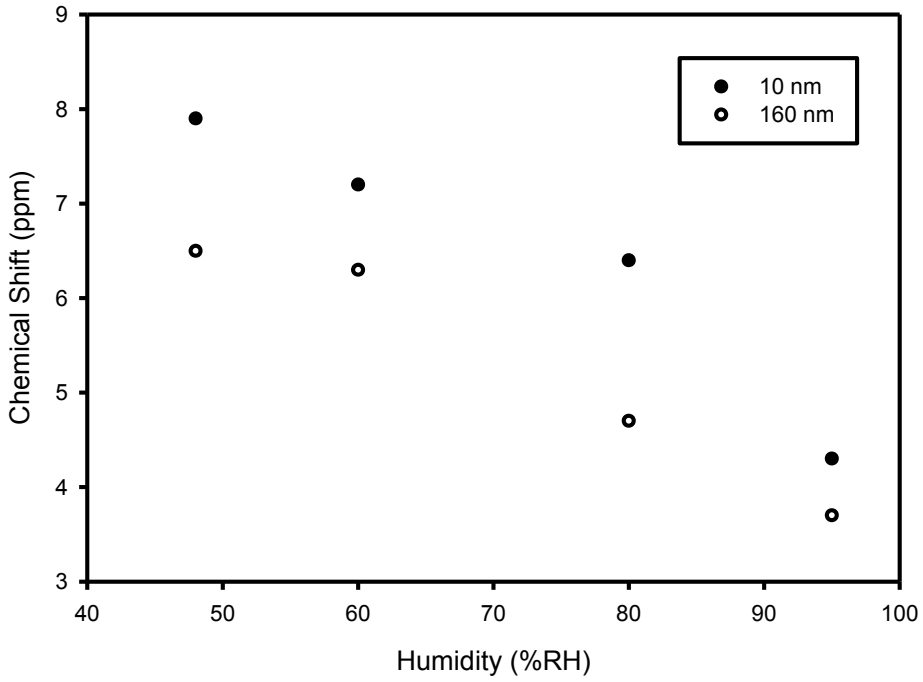

Figure 3.4: ^{1}H 800 Hz MAS Solid-State NMR of Humidified Ultra-Thin and Thin Nafion Films at 25°C. Samples were packed into a 7 mm rotor with powdered Teflon in between the disks. Samples were humidified for 24 hours to equilibrate fully to the conditions.

^{1}H chemical shifts are known to change with temperature due to changes in the H-bonded network. This phenomenon can be observed in **Figure 3.5** where the ^{1}H MAS NMR of Nafion thin films at 95% RH changes with chemical shift as the temperature is increased. The peak is narrow as expected with high water content that increases local dynamics with higher mobility in the H-bonded network. The chemical shift dramatically decreases towards lower frequency with increasing temperature due changes in local dynamics with the H-bonded network increasing in mobility. To further probe the differences in the films variable temperature ^{1}H NMR was performed at various relative humidities to observe differences in local dynamics via the influence on the chemical shift. Under variable temperature ^{1}H NMR at high humidity, both films exhibit a low chemical shift (between 3-4 ppm) that is comparatively unchanged with increasing temperature as seen in **Figure 3.6a**. Thus, both the ultra-thin and thin Nafion films show similar behaviour, indicating that at high humidity the local dynamics similar, as found by T_2 analysis as well. However, as seen above in **Figure 3.4** more substantial differences between ultra-thin and thin films are observed as the humidity is lowered.

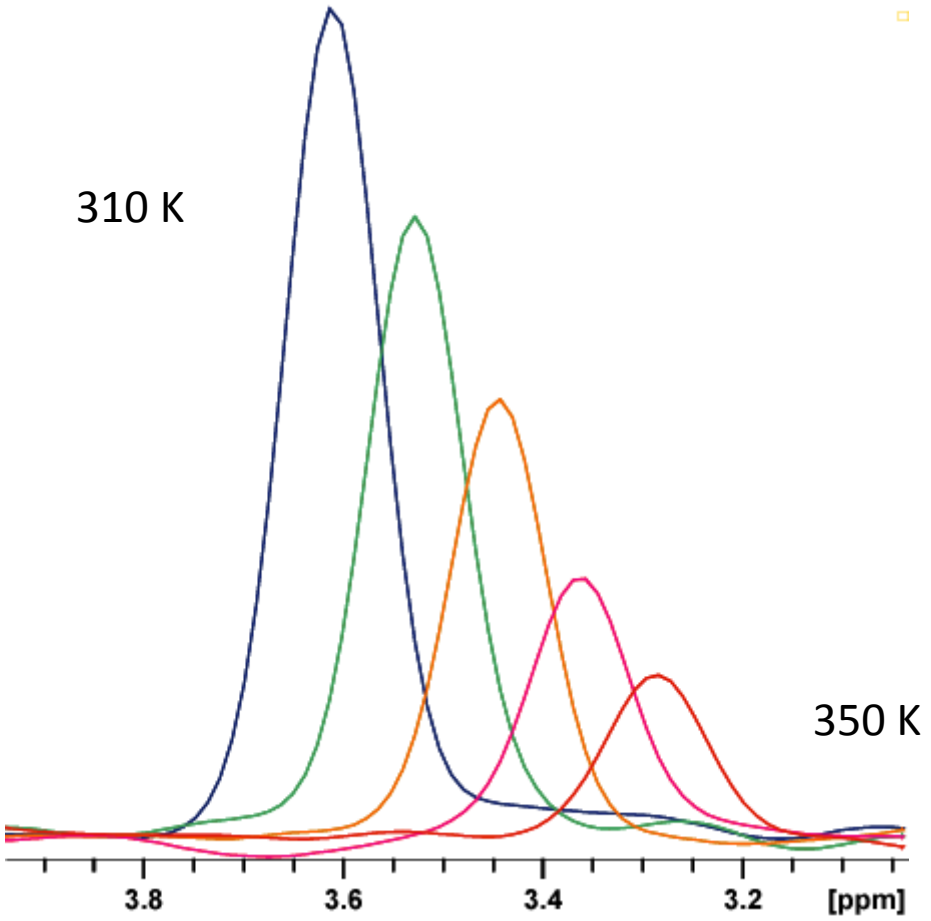

Figure 3.5: ^{1}H MAS Variable Temperature NMR of 160 nm film at 95% (λ=10).

At decreased relative humidity (60 and 48%) the ^{1}H chemical shifts of both the ultra-thin and thin Nafion films move to higher frequency, consistent with stronger hydrogen bonding, as seen in **Figure 3.6b and 3.6c**. The thin film exhibits behavior that was comparable to the membrane form of Nafion, where the chemical shift increased with decreasing R.H., and the chemical shift change with temperature becomes substantial. This indicates a strongly thermally activated proton hopping process within the thicker films, as within Nafion membranes. In contrast, the ultra-thin film does not change its ^{1}H chemical shift as a function of temperature at low humidity (48 and 60%). The chemical shift differences between the ultra-thin and thin films are most significant

under lower humidity conditions, as described in **Figure 3.4**; moreover, the thin film chemical shift is increasingly temperature dependent with decreasing humidity, in contrast to the temperature-independent chemical shift of the ultra-thin films. This temperature-independent behaviour of the ultra-thin films at low humidity indicates a lack of change in its H-bonded network. It may be noted that for the 10 nm film, the water uptake at 40% RH, as reported in **Table 3.1**, is still significantly higher than that of the thicker film, or Nafion membrane. Thus, the local proton environment of the ultra-thin film is water-rich and protons have highly dissociated such that as a result further change in humidity does not change the proton dynamics. The T_2 study above showed that at low humidities the ultra-thin film was in fast exchange, and yet at these conditions it is also temperature independent. This combined behaviour implies that there are domains within the structure that are in fast exchange, however long-range transport is impeded between the domains, which accounts for the larger activation energy for macroscopic conductivity in the ultra-thin films. In contrast, the thin film exhibits typical temperature-dependent behaviour, as seen for Nafion 117, indicating that long-range transport could be achieved in this film, explaining the differences of proton conductivity with ultra-thin and thin films.[11]

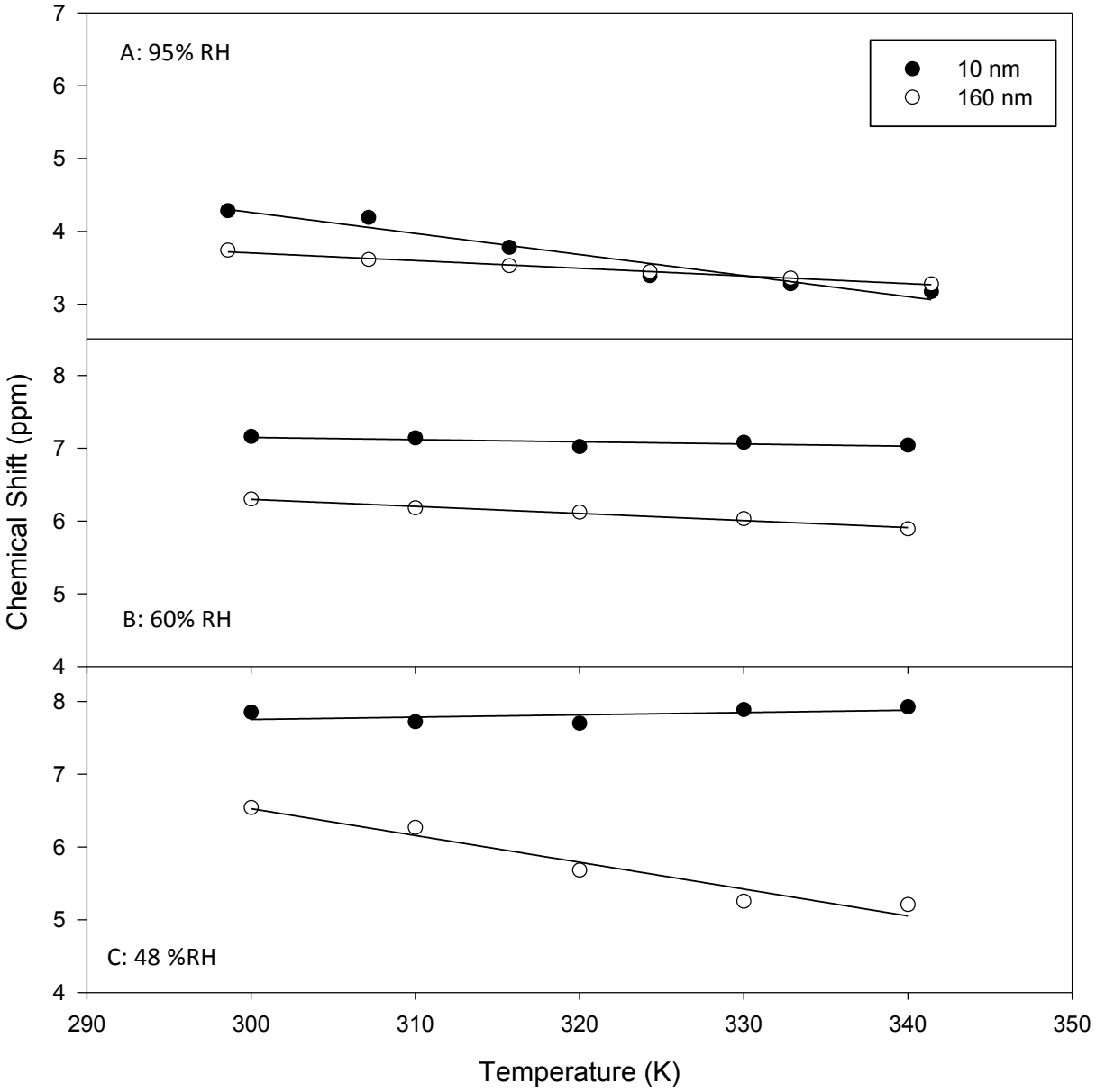

Figure 3.6: Chemical shift trends for ^{1}H MAS NMR spectra of humidified thin and ultra-thin Nafion films.acquired under 800 Hz MAS, using 7 mm rotors. A) Equilibrated to 95% RH B) Equilibrated to 60% RH C) Equilibrated to 48% RH.

3.4 Conclusion

^{1}H solid-state NMR was applied for the first time to nanothin Nafion films, humidified under controlled conditions, and acquired under slow MAS. These results demonstrate the viability of ^{1}H NMR under such challenging conditions, and open the door to further measurements of ionomers within fuel cell catalyst layers, where loadings are extremely low. Intriguingly, conductivities differed greatly between ultra-thin and thin Nafion films, attributable to either differences in local dynamics or limitations in long-range transport. Using solid-state ^{1}H NMR, it was shown that T_2 remained constant within error for both film thicknesses and under all humidity and temperature conditions, consistent with fast ^{1}H exchange within the H-bonded domains. The largest contrast between the ultra-thin and thin Nafion films was detected for the ^{1}H chemical shifts measured at low humidity. The thin film portrayed temperature dependent behaviour consistent with changes in the H-bonded network as proton conductivity increased. This behavior is consistent with other data, which demonstrated that the thin films have performance and properties equivalent to those determined for standard Nafion membranes. The hydrophobic surfaces, together with the thermally activated proton dynamics, are consistent with a picture of an internal phase-segregated structure with continuous channels for proton transport. In contrast, it was shown that the ultra-thin film at low humidity exhibited temperature independent ^{1}H chemical shifts, indicating that there were no additional changes to the H-bonded network. This observed behaviour could be interpreted as a set of isolated pools of conductive domains on the hydrophilic surface of the ultra-thin films, where increasing temperature cannot further enhance proton mobility at the local scale. We speculate that the ultra-thin film has limited ability

to structurally rearrange in order to achieve a contiguous network for long-range conductivity, causing a lower overall conductivity and higher activation energy for macroscopic transport in spite of the high level of water uptake on the surface. This hypothesis is supported by recent GISXAS and TEM analysis of ultra-thin/thin films where no characteristic ionomer domain in 4-10 nm films were observed.[5] This may be due to the influence of surface-polymer interactions, which become dominant as the film becomes thinner, prompting ongoing studies of the role of the substrate.

3.5 References

(1) Mauritz, K. A.; Moore, R. B. State of Understanding of Nafion. *Chem. Rev.* **2004**, *104*, 4535–4585.

(2) Carrette, L.; Friedrich, K. A.; Stimming, U. Fuel Cells - Fundamentals and Applications. *Fuel Cells* **2001**, *1*, 5–39.

(3) Holladay, J. D.; Hu, J.; King, D. L.; Wang, Y. An Overview of Hydrogen Production Technologies. *Catal. Today* **2009**, *139*, 244–260.

(4) Tailoka, F.; Fray, D. J.; Kumar, R. V. Application of Nafion Electrolytes for the Detection of Humidity in a Corrosive Atmosphere. *Solid State Ion.* **2003**, *161*, 267–277.

(5) Paul, D. K.; Karan, K.; Docoslis, A.; Giorgi, J. B.; Pearce, J. Characteristics of Self-Assembled Ultrathin Nafion Films. *Macromolecules* **2013**, *46*, 3461–3475.

(6) Modestino, M. A.; Paul, D. K.; Dishari, S.; Petrina, S. A.; Allen, F. I.; Hickner, M. A.; Karan, K.; Segalman, R. A.; Weber, A. Z. Self-Assembly and Transport Limitations in Confined Nafion Films. *Macromolecules* **2013**, *46*, 867–873.

(7) Eastman, S. A.; Kim, S.; Page, K. A.; Rowe, B. W.; Kang, S.; DeCaluwe, S. C.; Dura, J. A.; Soles, C. L.; Yager, K. G. Effect of Confinement on Structure, Water

Solubility, and Water Transport in Nafion Thin Films. *Macromolecules* **2012**, *45*, 7920–7930.

(8) James, P. J.; Antognozzi, M.; Tamayo, J.; McMaster, T. J.; Newton, J. M.; Miles, M. J. Interpretation of Contrast in Tapping Mode AFM and Shear Force Microscopy. A Study of Nafion. *Langmuir* **2001**, *17*, 349–360.

(9) Siroma, Z.; Kakitsubo, R.; Fujiwara, N.; Ioroi, T.; Yamazaki, S.; Yasuda, K. Depression of Proton Conductivity in Recast Nafion (R) Film Measured on Flat Substrate. *J. Power Sources* **2009**, *189*, 994–998.

(10) Paul, D. K.; Fraser, A.; Karan, K. Towards the Understanding of Proton Conduction Mechanism in PEMFC Catalyst Layer: Conductivity of Adsorbed Nafion Films. *Electrochem. Commun.* **2011**, *13*, 774–777.

(11) Paul, D. K.; Karan, K. Conductivity and Wettability Changes of Ultrathin Nafion Films Subjected to Thermal Annealing and Liquid Water Exposure. *J. Phys. Chem. C* **2014**, *118*, 1828–1835.

(12) Eikerling, M.; Kornyshev, A. A.; Kuznetsov, A. M.; Ulstrup, J.; Walbran, S. Mechanisms of Proton Conductance in Polymer Electrolyte Membranes. *J. Phys. Chem. B* **2001**, *105*, 3646–3662.

(13) Schmidt-Rohr, K.; Chen, Q. Parallel Cylindrical Water Nanochannels in Nafion Fuel-Cell Membranes. *Nat. Mater.* **2008**, *7*, 75–83.

(14) Kühne, R. O. Study of Transient Chemical Reactions by NMR. Fast Stopped-Flow Fourier Transform Experiments. *J. Magn. Reson. 1969 35*, 39–67.

(15) Hahn, E. L. Spin Echoes. *Phys. Rev.* **1950**, *80*, 580–594.

(16) Graf, R. New Proton Conducting Materials for Technical Applications: What Can We Learn from Solid State NMR Studies? *Solid State Nucl. Magn. Reson.* **2011**, *40*, 127–133.

(17) Dishari, S. K.; Hickner, M. A. Antiplasticization and Water Uptake of Nafion Thin Films. *Acs Macro Lett.* **2012**, *1*, 291–295.

(18) Modestino, M. A.; Kusoglu, A.; Hexemer, A.; Weber, A. Z.; Segalman, R. A. Controlling Nafion Structure and Properties via Wetting Interactions. *Macromolecules* **2012**, *45*, 4681–4688.

(19) Bain, A. D. Chapter 2 Chemical Exchange. *Annu. Rep. NMR Spectrosc.* **2008**, *63*, 23–48.

(20) Jameson, C. J. Understanding of Chemical Shifts. *Annu. Rev. Phys. Chem.* **1996**, *47*, 135–169.

(21) Ye, G.; Janzen, N.; Goward, G. R. Solid-State NMR Study of Two Classic Proton Conducting Polymers: Nafion and Sulfonated Poly(ether Ether Ketone)s. *Macromolecules* **2006**, *39*, 3283–3290.

(22) Paul, D. K.; McCrery, R.; Karan, K. *J. Electrochem. Soc.* **2014**, 161 (14), F1395-F1402.

(23) Sone, Y.; Ekdunge, P.; Simonsson, D. Proton Conductivity of Nafion 117 as Measured by a Four-Electrode AC Impedance Method. *J. Electrochem. Soc.* **1996**, *143*, 1254–1259.

(24) Zawodzinski, T. A.; Derouin, C.; Radzinski, S.; Sherman, R. J.; Smith, V. T.; Springer, T. E.; Gottesfeld, S. Water Uptake by and Transport Through Nafion® 117 Membranes. *J. Electrochem. Soc.* **1993**, *140*, 1041–1047.

Chapter 4
Double Quantum NMR Investigation of Motion in Solid Acids for Proton Exchange Membrane Fuel Cells

Currently, the most popular proton exchange membrane (PEM) for fuel cell applications is Nafion. However, it is not sufficiently conductive at high temperatures due to its dependence on–water for proton transport. To access the desired high operational temperature, a family of solid acids was investigated. Cations with known dynamics were paired with anions to make an overall acidic salt. Solid acids of interest here include imidazole paired with trifluoromethanesulfuric acid as well as imidazole, benzimidazole and adenine paired with methanesulfonic acid. Solid state NMR was utilized to show the relative mobility of protons through double quantum filter (DQF) experiments. The POST C7 homonuclear dipolar recoupling scheme was paired with DUMBO for ^{1}H homonuclear decoupling to produce a double quantum coherence buildup curve. When the maximum in the build up curve is reached at short recoupling times, this indicates strong dipole-dipole coupling, and is interpreted to indicate limited dynamics of the H-bonded protons. In contrast, when the build-up curve is stretched out, only reaching a maximum at longer recoupling times, it is inferred that such H-bonded protons (in an otherwise similar structure) are associated with proton transport which reduces their local dipolar coupling. The buildup curves have been simulated in Spin Evolution®, utilizing up to 8 pairs of homonuclear dipolar couplings within a sphere of 3.5 Å.[1] This was performed relative to the central H-bonded proton to extract the characteristic build-up curves. Bulk proton conductivity measurements were compared to DQF measurements to understand proton conduction within these materials.

This chapter has been submitted to Physical Chemistry Chemical Physics and the co-authors of this paper are K.J. Harris and G.R. Goward. K.J. Harris aided in setting up the pulse

sequence on our spectrometer and coding the simulation input file and G.R. Goward assisted in discussions and editing this draft. I synthesized the salts, performed EIS, NMR and simulations on all the samples and prepared the draft of this paper.

4.1 Introduction

Proton electrolyte fuel cells (PEFCs) are promising energy carriers for both automobiles and stationary applications. Current PEFCs use Nafion® as an electrolyte due to its chemical resistance, durability and high proton conductivity.[2] Nafion conducts protons via a vehicle mechanism utilizing water as a proton carrier. Thus PEFCs constructed with Nafion are optimal for operation only at temperatures <80°C due to their dependence on water.[3] Unfortunately, these low temperatures are also where the catalyst is most susceptible to carbon monoxide poisoning.[4] For increased catalyst longevity, operational temperatures above 120°C have been recommended.[5]

Promising alternatives to Nafion include inorganic and organic solid acids due to their temperature and electrochemical stability.[6–10] These solid acid systems utilize the Grotthuss mechanism for proton conduction instead of the vehicle mechanism, which may enable anhydrous high temperature operating conditions.[11] Inorganic solid acids were first introduced by Haile et al. using $CsHSO_4$ which was shown to provide high proton conductivity for up to 80 hours at 250°C.[6]

Other solid acid conductors employ heterocyclic cations with organophosphorus or organosulfur anions to produce an organic solid acid.[7] These organic solid acids have demonstrated modest proton conductivity under anhydrous high temperature conditions. Benzimidazolium and imidazolium phosphonates have been reported to retain proton conductivities on the order of $1x10^{-6}$ to $1x10^{-5}$ S/cm under anhydrous, high-temperature

conditions;[12] however, polymerization of the phosphate groups was found to limit long term stability.[13] Sulfonate groups are more resistant to polymerization and as such represent a promising alternative. Our results on proton conductivity, stability, and local proton dynamics in adenine-, benzimidazolium- and imidazolium-methanesulfonate, and imidazolium-trifluoromethanesulfonate, are thus presented.

Electrochemical impedance spectroscopy is the industry standard for measurement of proton conductivity for ionic conductors; however, this technique provides a bulk average conductivity, which is influenced by variety of factors at different length scales. It does not unambiguously provide insight into the molecular-level processes, which govern this proton transport. Solid-state ^{1}H NMR is well known for its sensitivity to local hydrogen bonded geometries. Moreover, the degree of local mobility can be measured in a site-specific fashion using homonuclear dipolar recoupling schemes, which allows for an insightful description of proton conduction pathways. By comparing these NMR findings with conductivity data, we demonstrate here how the dipolar coupling characteristics can be mapped onto bulk conductivity properties, and provide a tool for investigation of solid acid conduction pathways.

4.2 Solid-State NMR Theory

Solid-state ^{1}H NMR is utilized to probe hydrogen bonding environments, as observed via the chemical shift itself, and dynamics on a molecular scale, as probed via the dipolar couplings of the H-bonded protons.[14] Dipole-dipole coupling interactions depend on the gyromagnetic constant (γ_i and γ_j) of the nuclei (I and S), the distance (r) and orientation (θ) between them through the well-known Hamiltonian for homonuclear dipolar coupling as seen in **Equation 4.1**.[15]

$$H_D = -\sum_{i>j}\left(\frac{\mu_o}{4\pi}\right)\left(\frac{\gamma_i\gamma_j\hbar}{r_{ij}^3}\right) * \frac{1}{2}(3\cos^2\theta - 1)[\hat{I}_z\hat{S}_z] \quad \textbf{(4.1)}$$

The inherently strong homonuclear dipolar couplings create broad spectra in ^{1}H solid-state NMR spectra of organic solids. To enhance the resolution of proton spectra in the solid-state two methods are commonly employed. Ultra-fast magic angle spinning (MAS), with currently accessible spinning speeds ranging from the routine 25 kHz to more recent achievements of up to 100 kHz, are often sufficient to achieve reasonable spectral resolution through averaging of the spatially-dependent portion of **Equation 1**. Secondly, decoupling CRAMPS (combined rotation and multiple-pulse spectroscopy) techniques are robust and readily implementable in combination with other pulse sequence building blocks. This method utilizes rf pulses to synchronize rotations of nuclear spins about the magic angle, together with moderate speed MAS to achieve dramatic line narrowing averaging the spin portion of **Equation 1**. There are several well-known CRAMPS sequences, such as frequency-switched Lee-Goldburg (FSLG), phase-modulated Lee-Goldburg (PMLG) and decoupling under mind boggling optimization (DUMBO).[16–19] For this chapter we use DUMBO for our homonuclear decoupling due to it is a continuous method that utilizes lower power and can operate at higher sample spinning speeds.

Once chemical shift resolution has been achieved, it is useful to extend the NMR study to probe dipolar couplings among resolved ^{1}H sites. This is typically achieved using a double quantum coherence (DQC) excitation scheme, such as POST C7 or back-to-back (BaBa) to recouple homonuclear dipole-dipole couplings.[20–22] A 1D double quantum filter (DQF) experiment would result in attenuation or elimination of sites due to either lack of near neighbors

or mobility. Using a 2D DQF experiment spins pairs can be observed that exhibit a dipole-dipole coupling, which is shown in chapter 2. The efficiency of the recoupling depends on the distance between the protons, as well as the length of the excitation pulse sequence. Here we have utilized the POST C7 sequence, as a function of incremented excitation and reconversion periods, to create DQC buildup curves to probe the homonuclear dipolar couplings for spin pairs within the structures. In particular, we have focused on those couplings that represent inter-molecular contacts between the H-bonded centers and the anion/cation of the solid-acid structures. The dipole-dipole coherences are observed using 2D POST C7 single-quantum: double quantum correlation spectra, where only spin pairs that possess a dipole-dipole coupling would be observed in the 2D spectrum. We have evaluated the spectra and created DQC buildup curves for each spin pair. In each case the steepness of the buildup curves are compared to evaluate the relative strengths of the dipolar interactions, in analogy to previous work by S.P. Brown and co-workers.[23] With all the relative dipole coupling strengths known pathways of proton conduction can be inferred to differentiate between different structures to predict performance.

While ^{1}H NMR provides a local picture of the dynamics in the hydrogen-bonding motif, proton conductivity is obtained via electrochemical impedance spectroscopy (EIS), which probes the bulk transport properties.[24,25] Conductivity measurements will be correlated with NMR data to compare the relative efficiency of proton transport within the organic solid acids of interest here.[9]

4.3 Experimental

4.3.1 Sample Preparation

Adenine methanesulfonate (AMSA) benzimidazolium methanesulfonate (BMSA) and imidazolium methanesulfonate (IMSA) were synthesized by dissolving adenine, benzimidazole or imidazole in minimal amounts of methanol and adding methanesulfonic acid in a 1:1 molar ratio. The solution was left to crystallize the product. Crystals were heated at 80°C for 24 hours to remove any trapped solvent. Imidazolium trifluoromethanesulfonate (IFMS) was purchased from Sigma Aldrich.

4.3.2 Solid-State NMR Experiments

All POST-C7 DQ excitation and reconversion steps were performed under 12.5 kHz MAS using an 87.5 kHz rf field at 11.7 T with a Bruker Avance spectrometer. Samples were packed in 2.5 mm rotors and spectra were referenced to adamantane (1.85 ppm for ^{1}H).[26] Delays set were chosen to be 5 times greater than the T_1 of the sample ranging from 10-45 s. DUMBO homonuclear decoupling was achieved using an optimized rf field of just under 100 kHz. A set of 2D POST-C7 DQ experiments with DUMBO decoupling were collected over a series of DQ excitation and reconversion periods, where these two periods were varied symmetrically. Blocks of 1 to 10 POST-C7 DQ pulse sequence elements were used to generate these DQ excitation and reconversions.

Experiments performed under a 21.1T external field were performed at the National Ultrahigh-Field Solid-State NMR Facility, in Ottawa, Canada. These experiments were conducted with a specially built single-frequency probe, which employs rotors of 0.85 mm diameter and achieves spinning speeds of 100 kHz. 2D DQ-SQ correlation spectra acquired under ultrafast MAS used two rotor periods (22 μs) for DQ excitation and reconversion using the

BaBa sequence with a 100 kHz rf field.[21,28] Under ultrafast MAS conditions, no homonuclear decoupling pulse sequence was found necessary for high-resolution spectra.

Simulations of the POST-C7 DQ experiments were conducted using the SPINEVOLUTION software package. Each particular ^{1}H nucleus of interest was investigated using simulations including that proton and all others appearing inside a sphere with a 7 Å diameter within the crystal structure. Chemical shift anisotropy was not considered, as it has been shown to have a negligible effect on DQ buildup curves for protons in organic systems under moderate external field strengths.[23] Experimentally, the frequency of the SQ coherences have to be measured during the direct dimension to separate the signal into contributions from the various nuclei; in contrast, simulations are easily arranged to directly report the intensity of the SQ coherence after the DQ to SQ reconversion. Accordingly, the 2D experiments were rapidly investigated using 1D simulations that are equivalent to one slice of the indirect dimension of the experiment at the frequency of the SQ coherence for the spin of interest. These 1D spectra were simulated using a rotor-synchronized dwell period and 64 data points, and the frequency of each peak within them were used to identify the nuclear spin that is coupled to the spin of interest. In all simulations, dipolar couplings were set to zero during the DQ evolution period, and 60 crystallites arranged over a sphere were used to model the powder. A series of such 1D simulations, with different lengths of POST-C7 DQ excitation and reconversion blocks, were used to generate the Figures shown below.

4.3.3 Macroscale Techniques

Clear and colorless single crystals were grown via slow evaporation from a saturated methanol solution. Single crystal X-ray experiments were obtained by making a saturated solution of the salt in methanol. All crystals obtained were clear and colourless. X-ray

diffraction measurements were conducted at 100 K with a Bruker D8 diffractometer equipped with a SMART6000 CCD detector. The radiation source was a Cu K-α with a wavelength of 1.54178 Å.

Electrochemical impedance spectroscopy was carried out with a Gamry Interface 1000 potentiostat. Pure salts were pressed into pellets with 5000 psi of pressure, sintered at 130°C overnight and covered in 30 nm of gold on both sides for through-plane conductivity measurements. The cell was equilibrated in an oven under anhydrous conditions for one hour before conductivity measurements at 25°C. Experiments were conducted at a DC voltage of 0.5 V, amplitude of 50 mV, and a frequency sweep from 1.0×10^6 to 1.0×10^3 Hz.

4.4 Results and Discussion

Organic solid acids are promising materials for PEMFCs due to their high electrochemical stability in high temperature anhydrous conditions. Solid-state NMR is used here to probe locally hydrogen-bonded sites. The relative mobility of each H-bonding motif, probed by measuring DQC buildup curves and their simulations, is correlated with the efficiency of that solid-acid structure in achieving bulk proton transport.

4.4.1 Electrochemical Impedance Spectroscopy

Previous studies have shown that the increase in conductivity as a function of temperature can be correlated to the melting point of the salt. Melting point determinations were conducted using differential scanning calorimetry where the melting point of AMSA is >300°C whereas, BMSA, IMSA and IFMS melt at 240°C, 191°C, and 189°C respectively. Based on the melting points it is predicted that IFMS would possess the highest proton conductivity among the salts, at a given temperature (less than the melting points). **Table 4.1** lists the bulk proton conductivities of four organic solid acid salts measured at 25°C, i.e., the same conditions used in

the solid-state NMR experiments. Of the three structures that include the methylsulfonic acid anion, AMSA has the lowest room temperature conductivity at $2.7\pm0.1\times10^{-10}$ S/cm. The other two methylsulfonic acid analogues, BMSA and IMSA, have similar conductivities at $5.5\pm0.2\times10^{-10}$ and $5.7\pm0.1\times10^{-10}$ S/cm respectively. It is interesting to note that the conductivity BMSA possesses is similar to IMSA, in spite of the larger benzimidazolium cation. This indicates that the rotation of the cation is not rate limiting for proton transport in these two salts.[29] The fourth solid acid structure is analogous to IMSA, where the methyl group has been replaced with a fluorinated methyl group. The result is a more open structure for IFMS, which was confirmed crystallographically where IFMS has the highest cell volume of 1633.56 $Å^3$ compared to AMSA, BMSA and IMSA, which possess cell volumes of 960.77 $Å^3$, 984.54 $Å^3$ and 1419.59 $Å^3$ respectively. This created a material that possesses the highest proton conductivity of the group by a small margin. However, when measuring conductivities of salts, grain boundaries throughout the salt can alter overall performance. With different preparation procedures the grain boundaries can be reduced, thus proton conductivity can be increased. For remainder of this chapter we use solid-state NMR to probe mobility in these salts that could otherwise be hidden due to grain boundary resistances in proton conductivity measurements.

Table 4.1: Proton Conductivity of solid acids determined by EIS at 25°C under anhydrous conditions.

Salt	Conductivity (S/cm)
AMSA	$2.7\pm0.1\times10^{-10}$
BMSA	$5.5\pm0.2\times10^{-10}$
IMSA	$5.7\pm0.2\times10^{-10}$
IFMS	$6.4\pm0.2\times10^{-10}$

4.4.2 ^{1}H MAS NMR

Solid-state NMR probes compounds on a localized scale to reveal H-bonded network within the compounds of interest. For organic solid acids we can determine pathways that facilitate proton conduction throughout the structure. In this chapter we utilize a double quantum filter experiment to collect double quantum coherence (DQC) buildup curves through incremented excitation and reconversion times to determine dipole-dipole couplings within solid acids. Integrating the contour in each 2D experiment at these incremented times and plotting how the intensity changes over time constructs the DQC buildup curves. In particular, for this chapter we utilize the 2D POST C7 DUMBO sequence. For each solid acid we report an example 2D correlation spectrum, together with the full build-up curves (experimental and calculated based on crystallographic structure) for each intermolecular ^{1}H-^{1}H pair that includes the H-bonded proton found in the structure.

Before focusing on the solid acids, it is valuable to demonstrate the viability of the pulse sequence and simulation protocol in our hands. The Brown group has demonstrated this strategy for structural analysis for the dipeptide ß-AspAla based on strengths of dipole-dipole coupling.[23] Here, we chose glycine, which has a well-known structure with no significant ion mobility. This provides a robust standard for demonstrating the effectiveness of the pulse sequence. Additionally, it allows for simulation of its DQC buildup curves based on structural data, where local dynamics and their potential damping effect on the buildup curve will not play a role. In **Figure 4.1**, the direct dimension shows the 1D ^{1}H spectrum of glycine that possesses three equivalent proton sites in the NH_3 moiety at 8.1 ppm denoted site B and two inequivalent sites in the CH_2 group at 4.2 and 3.0 denoted A and A' respectively. Site B is baseline-resolved from the CH_2 protons and the CH_2 protons are resolved. This experiment with MAS alone would not

possess this site resolution, however with homonuclear decoupling the three sites are readily observable. For the indirect dimension in **Figure 4.1,** four dipole-dipole couplings result from the three sites in glycine. The dipole-dipole coupled pairs are between A-A', B-A, B-A' and B-B. Both A-A' and B-B represents both the intramolecular autocorrelation that is present within the functional groups (~1.8 Å) and intermolecular interactions between the same functional groups (~2.5 Å). The autocorrelation is a weighted average of both of these distances, with the shorter distance having a higher impact due to relationship between distance to dipole coupling. B-A and B-A' represent the bonding that exists between different functional groups both intramolecularly (~2.5 Å) and intermolecularly (~3.3 Å). Distances between the atoms were determined from the x-ray signal crystal structure. The structure for glycine first reported by Gustav et al, was used for the analysis of the DQC buildup curves.[30]

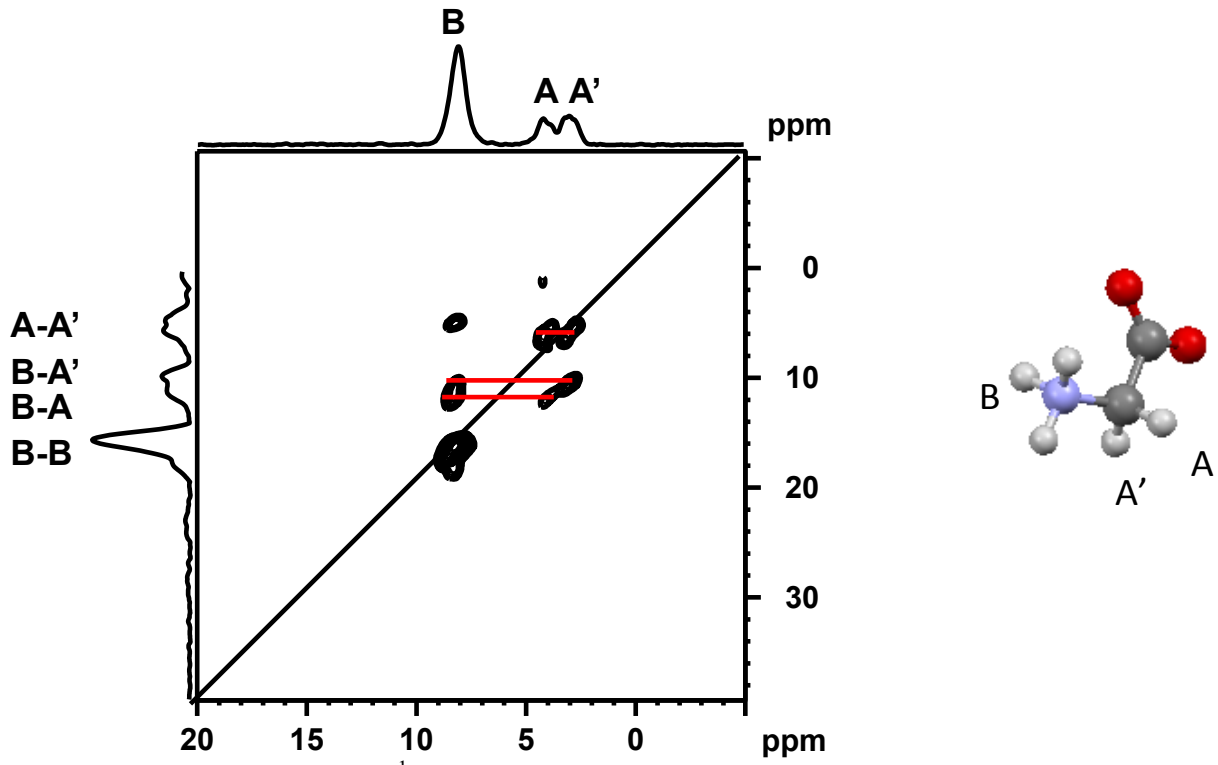

Figure 4.1: On the left is a 2D ^{1}H 12.5 kHz MAS POST C7-DUMBO using a supercycle with 2 loops of recoupling of Glycine collected on a 500 MHz at room temperature. There are three resonances observed in the direct signal quantum with four dipole-dipole coupled seen in the indirect double quantum dimension. On the right is the structure of glycine.

When comparing DQC buildup curves there are two main things to keep in mind; the time that is required to reach the maximum and the slope of the buildup. The shorter the time required to reach the maximum indicates strong dipole-dipole coupling. Longer times correlate to a weaker dipole-dipole coupling. Therefore, with initial inspections relative strengths of dipole-dipole coupling can be made. A similar comparison can be made with the slopes, the steeper the slope the stronger the dipole-dipole coupling and the gentler the slope the weaker the coupling. Since these structures are hydrogen rich, up to 10 spins were included in the simulations, to include all pairs that contribute to the pair of interest.

In **Figure 4.2A**, shows the DQC buildup curves for three of the spin pairs, A-A', B-B and B-A. For A-A' and B-B signals, both the DQC buildup curves rise steeply indicating strong

dipole coupling as expected from the short intramolecular distances that occur for both spin pairs. For B-A spin pair the intramolecular distance increases causing the DQC buildup to be slower than the shorter atomic distances that are present between B-B and A-A' sites. The simulations (**Figure 4.2B**) match the DQC buildup curves well for A-A' and B-B as both the slopes are steep and both simulations possess the same maximum. For B-A the slopes of the experimental and simulated DQC buildup curve were 0.0029±0.0005 s^{-1} and 0.0020±0.0007 s^{-1} respectively. Considering that the experimental and simulated DQC buildup curves possess similar maxima and their slopes are within error of each other, the simulated DQC buildup curves were determined to match well with the experimental DQC curve. Since the experimental data match the simulated data based on the crystal structure of glycine, the DUMBO-POST C7 method was utilized on solid acid structures to investigate the hydrogen bonded network and evaluate how efficiently different proton conduction pathways dampen the recoupling response.

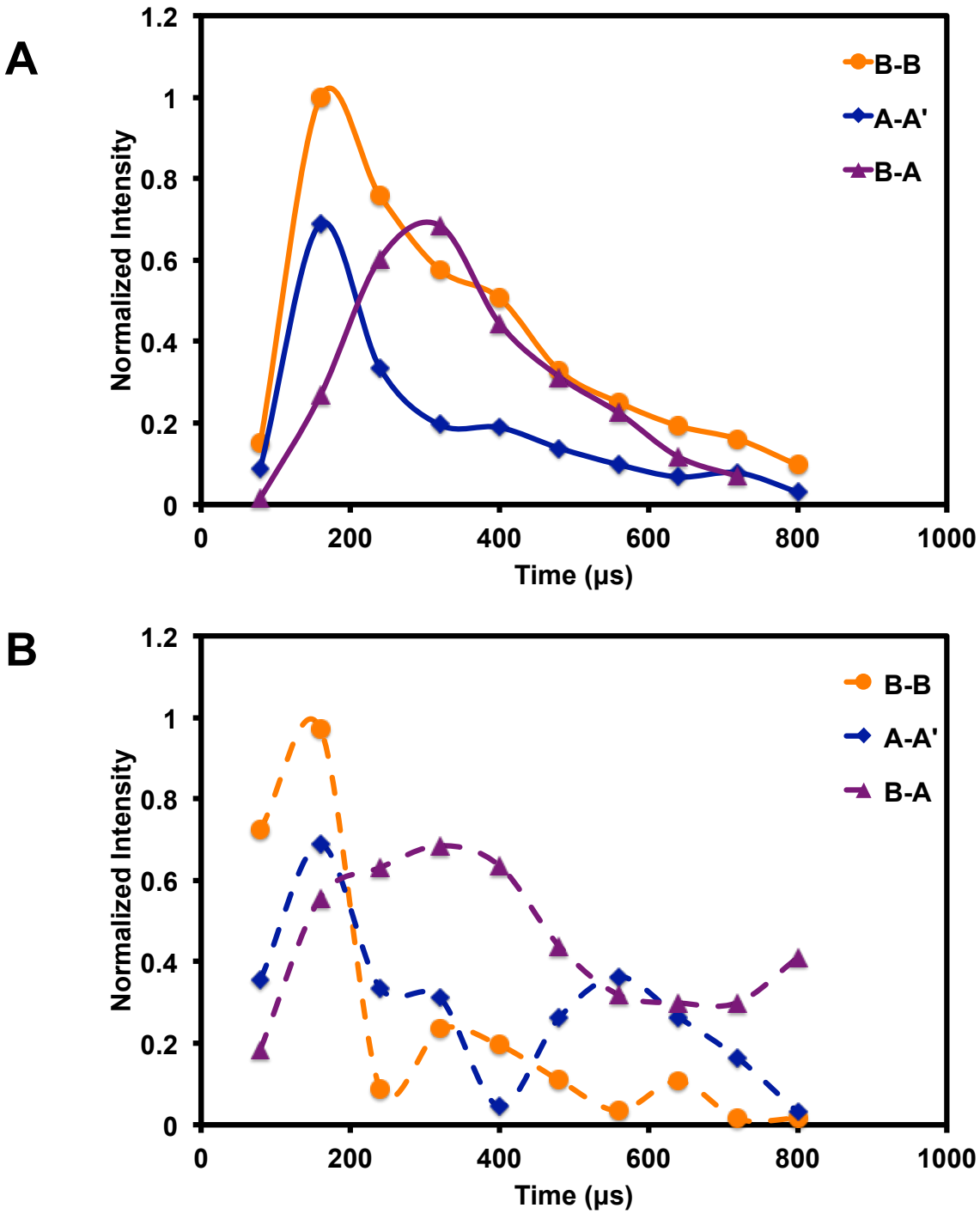

Figure 4.2: POST C7 DQC buildup curves of Glycine. A) Experimental buildup curves obtained from 2D POST C7 DUMBO collected at incremented delays B) Simulated DQC buildup curves of Glycine, which match generally well with experimental indicating there is no additional motion on this timescale.

The remainder of this section will be focused on the solid acids and the influence of their ion dynamics on the DQ measurements, as compared with simulations based on their known crystal structures. For BMSA, IMSA and IFMS their crystal structure details are included in a previous study.[10] For AMSA the crystal structure was determined for this study and its details are presented below. The first solid acid of interest is BMSA, which possesses one hydrogen-bonded peak, observed at 13 ppm (A), three aromatic peaks at 8 ppm (B), 6 ppm (C) and 4 ppm (D) and one aliphatic site at 3 ppm (E) as seen in **Figure 4.3** in the direct dimension. There are three homonuclear dipole-dipole coupled pairs in the BMSA salt as seen in the indirect dimension of **Figure 4.3**, which are labeled A-B, B-D and E-E. The DQC buildup curves for BMSA are seen in **Figure 4.4A**, where each dipole-dipole coupled pair has a similar buildup curve, as the evaluation of the slopes shows them to be equivalent within error. The simulated DQC buildup curves (**Figure 4.4B**) possess the same maximum as the experimental and initial slopes of experimental and simulated DQC buildup curves are within error to each other as seen in **Table 4.2**. Since all the DQC buildup curves and simulations are similar for all dipole-dipole couplings, we can conclude that for this structure the dipole-dipole couplings are the same for each pair, and that there is no motional averaging of the dipolar interaction in this case.

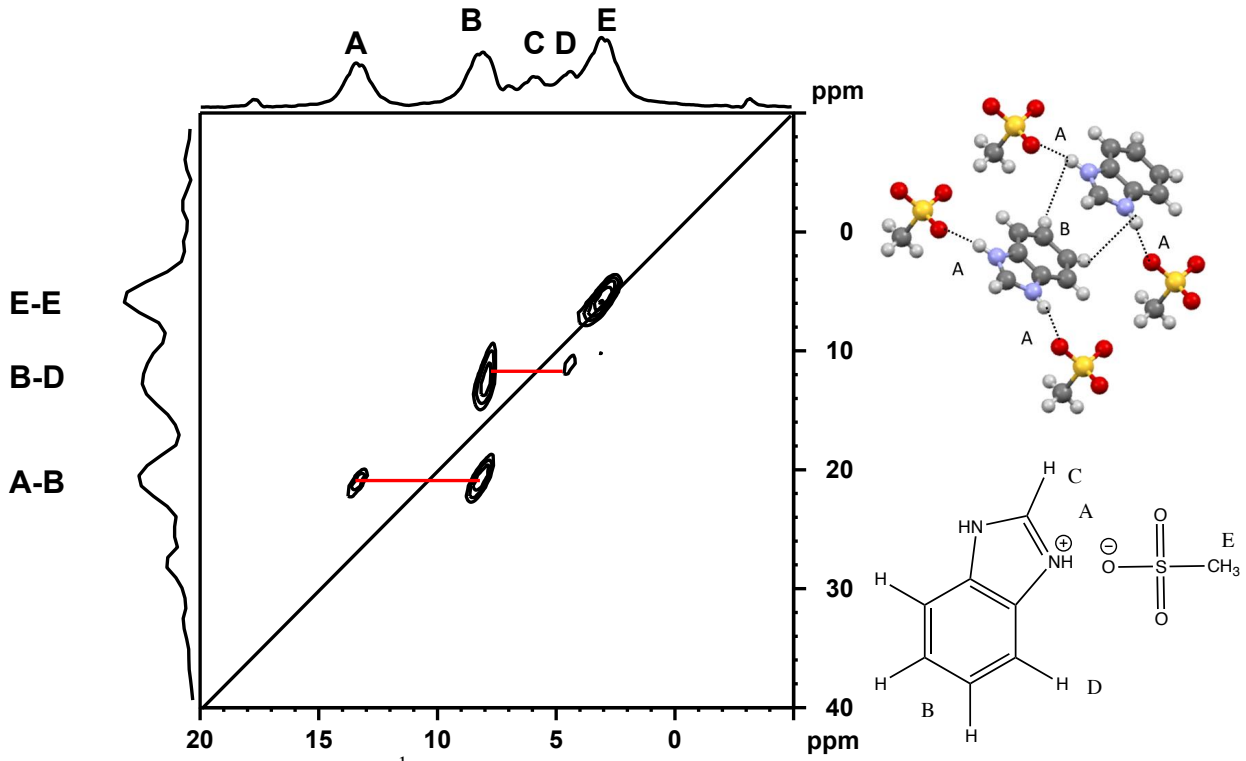

Figure 4.3: On the left is a 2D ^{1}H 12.5 kHz MAS POST C7-DUMBO using a supercycle with 2 loops of recoupling of BMSA collected on a 500 MHz at room temperature. There are five resonances observed in the direct dimension with three dipole-dipole coupled seen in the indirect double quantum dimension. On the right is an excerpt from the single crystal structure of BMSA, highlighting the intermolecular couplings of interest.

Table 4.2: Slopes of DQC Buildup Curves for BMSA, IMSA and IFMS Spin Pairs ($x10^{-3}$)

BMSA		
Pair	Experimental	Simulation
E-E	2.6±0.8 s^{-1}	2.3±0.1 s^{-1}
B-D	3.4±0.7 s^{-1}	3.7±0.2 s^{-1}
A-B	2.0±0.2 s^{-1}	1.8±0.1 s^{-1}
IMSA		
Pair	Experimental	Simulation
A-B	1.8±0.2 s^{-1}	1.8±0.2 s^{-1}
A-C	1.8±0.2 s^{-1}	1.3±0.3 s^{-1}
B-D	1.8±0.2 s^{-1}	1.5±0.6 s^{-1}
IFMS		
Pair	Experimental	Simulation
A-B	1.5±0.2 s^{-1}	2.4±0.1 s^{-1}
A-C	1.4±0.2 s^{-1}	2.3±0.4 s^{-1}
C-B	1.0±0.1 s^{-1}	1.7±0.1 s^{-1}

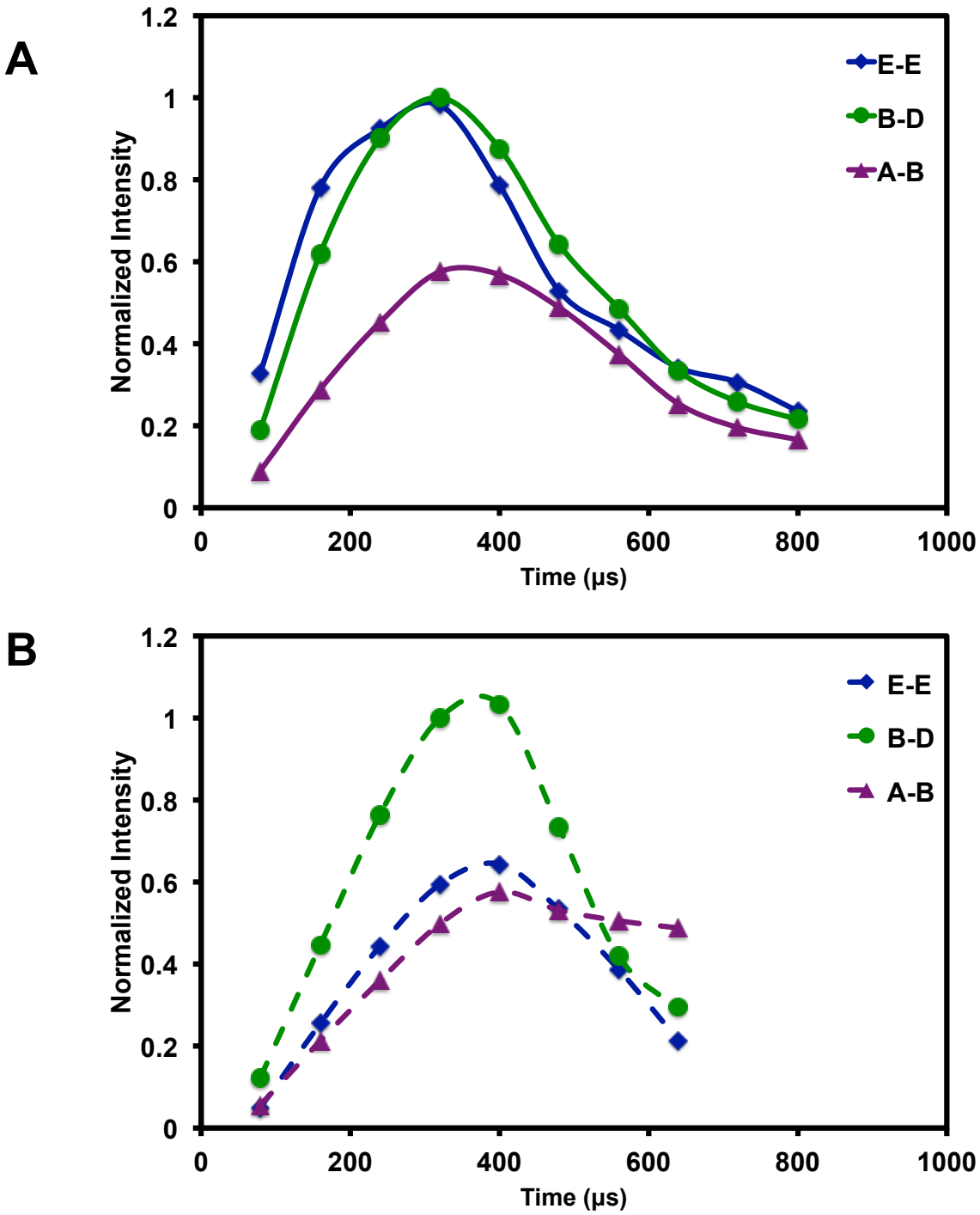

Figure 4.4: POST C7 DQC buildup curves of BMSA. A) Experimental buildup curves obtained from 2D POST C7 DUMBO collected at incremented delays B) Simulated DQC buildup curves of BMSA, which match generally well with experimental indicating there is no additional motion on this timescale.

The second solid acid of interest is IMSA, where the direct ^{1}H NMR spectrum (**Figure 4.5**) shows four proton resonances including the hydrogen-bonded peak at 13.0 ppm (A), the aromatic peaks at 7.6 ppm (B) and 9.1 ppm (C) and the aliphatic peak at 1.7 ppm (D). The IMSA structure contains five short-range proton homonuclear dipole-dipole couplings as seen in the indirect dimension of the 2D DQC spectrum in **Figure 4.5**, which are D-D, B-D, B-B, A-B and A-C. For this structure, all the dipole-dipole coupled pairs possess similar DQC buildup curves as seen in **Figure 4.6A**, therefore for simplicity only three dipole-dipole coupled pairs will be shown in this chapter, which will be B-D, A-B and A-C. In **Figure 4.6B**, the simulated DQC buildup curves possess the same maximum and the initial slopes of both DQC buildup curves are the same within error as seen in **Table 4.2**. The DQC buildup curves for BMSA and IMSA possess similar slopes and maximums for all the curves, and thus possess similar dipole-dipole couplings. This shows that BMSA and IMSA should possess similar proton conductivities, which supports the proton conductivity values obtained.

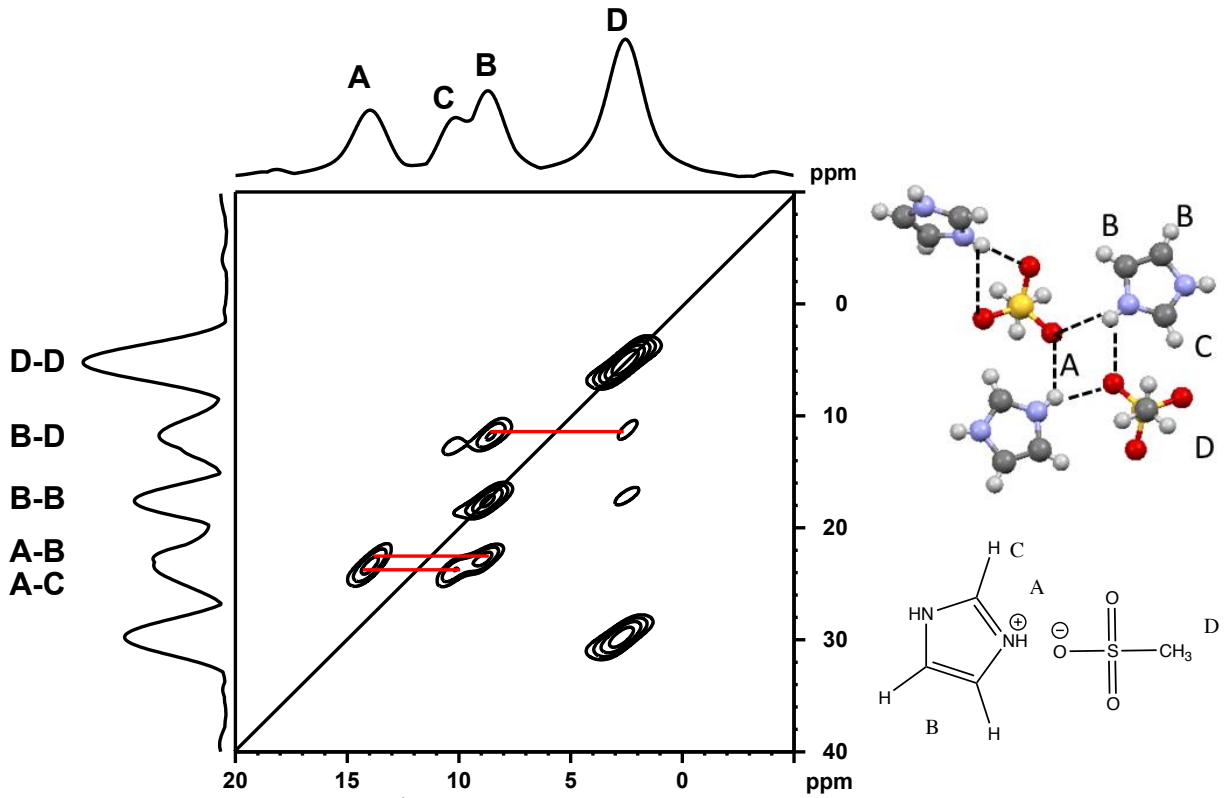

Figure 4.5: On the left is a 2D ^{1}H 12.5 kHz MAS POST C7-DUMBO using a supercycle with 2 loops of recoupling of IMSA collected on a 500 MHz at room temperature. There are four resonances observed in the direct dimension with five dipole-dipole coupled seen in the indirect double quantum dimension. On the right is the single crystal structure of IMSA.

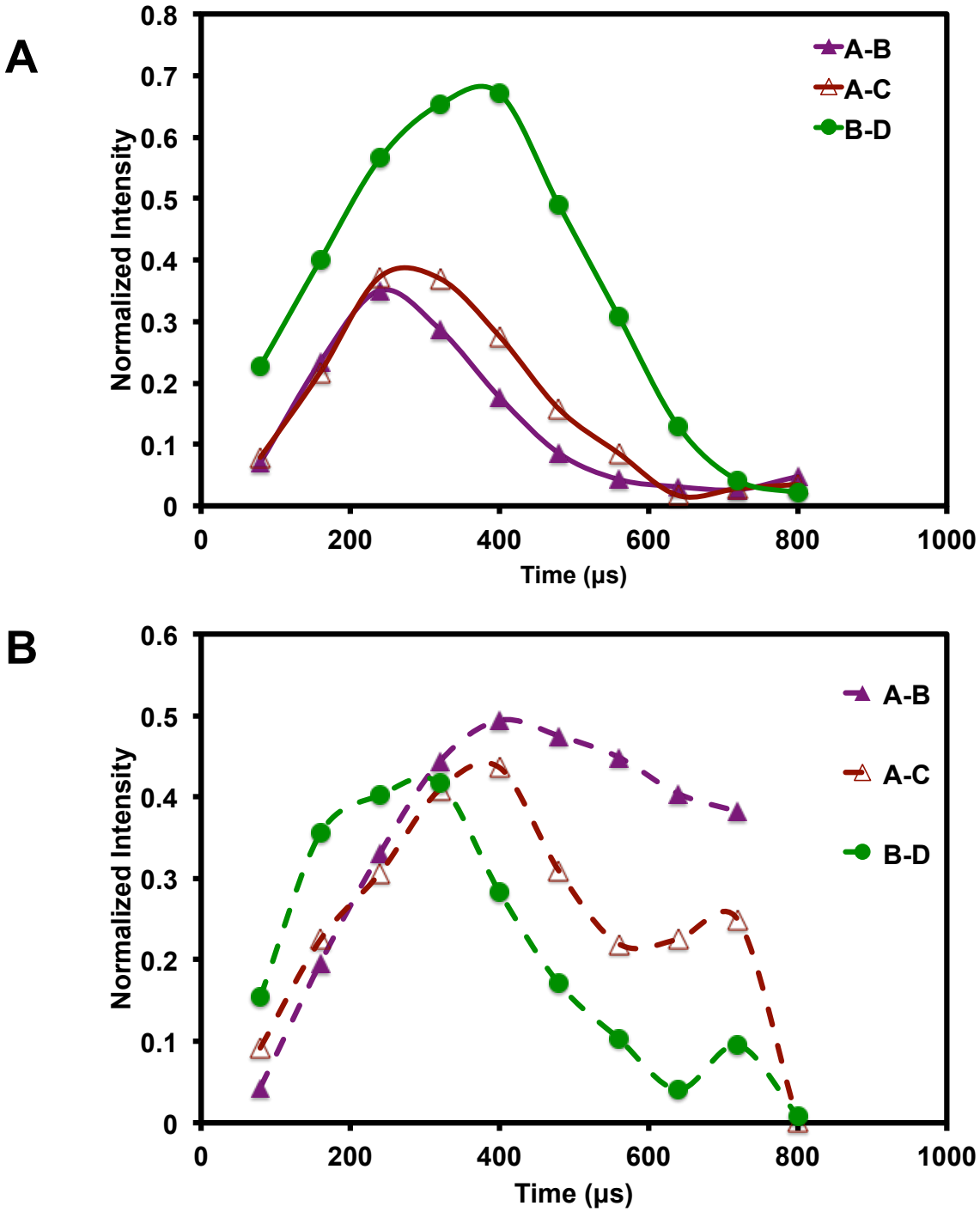

Figure 4.6: POST C7 DQC buildup curves of IMSA. A) Experimental buildup curves obtained from 2D POST C7 DUMBO collected at incremented delays B) Simulated DQC buildup curves of IMSA, where all buildup curves match well.

The third solid acid structure of interest, IFMS has three protons shifts 11.4 ppm for the hydrogen-bonded peak (A), 8.1 ppm for the first aromatic proton (C) and 7.1 ppm for the second aromatic proton (B). There are four homonuclear dipole-dipole coupling pairs in this compound, A-B, A-C, C-B and B-B as seen in **Figure 4.7**. The intermolecular distances for IFMS are similar to BMSA and IMSA, however the DQC buildups of IFMS are slower as seen in **Figure 4.8A** from longer recoupling times and gentler slopes. The simulated DQC buildup curves for IFMS do not fit the experimental from the DQC maxima in do not correspond as seen in **Figure 4.8B**. The simulated DQC buildup curves are predict a stronger dipole-dipole coupling (**Table 4.2**) from the steeper slope observed for the simulated DQC buildup curve compared to the experimental. Since the simulated curves predict stronger dipole-dipole couplings within the structure this suggests that there are additional dynamics within the structure on this timescale, the shallow slope of the experimental DQC buildup curve confirms this. Therefore, the similar proton conductivity obtained for IFMS compared to BMSA and IMSA is artificially low due to grain boundary resistance. This shows that the molecular level ion dynamics are not limiting the rate of transport, and that macroscopic processing may be able to take advantage of this to improve performance.

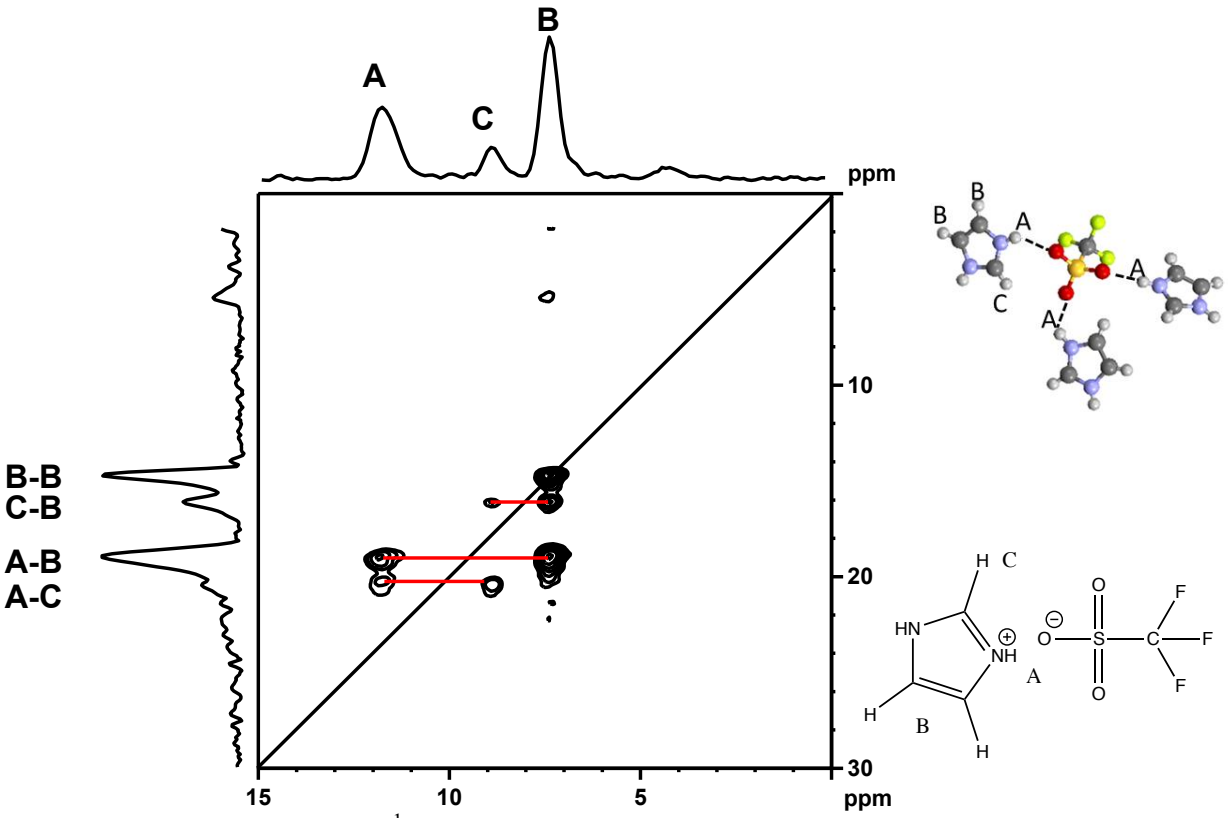

Figure 4.7: On the left is a 2D ^{1}H 12.5 kHz MAS POST C7-DUMBO using a supercycle with 2 loops of recoupling of IFMS collected on a 500 MHz at room temperature. There are three resonances observed in the direct dimension with four dipole-dipole coupled seen in the indirect double quantum dimension. On the right is the single crystal structure of IFMS.

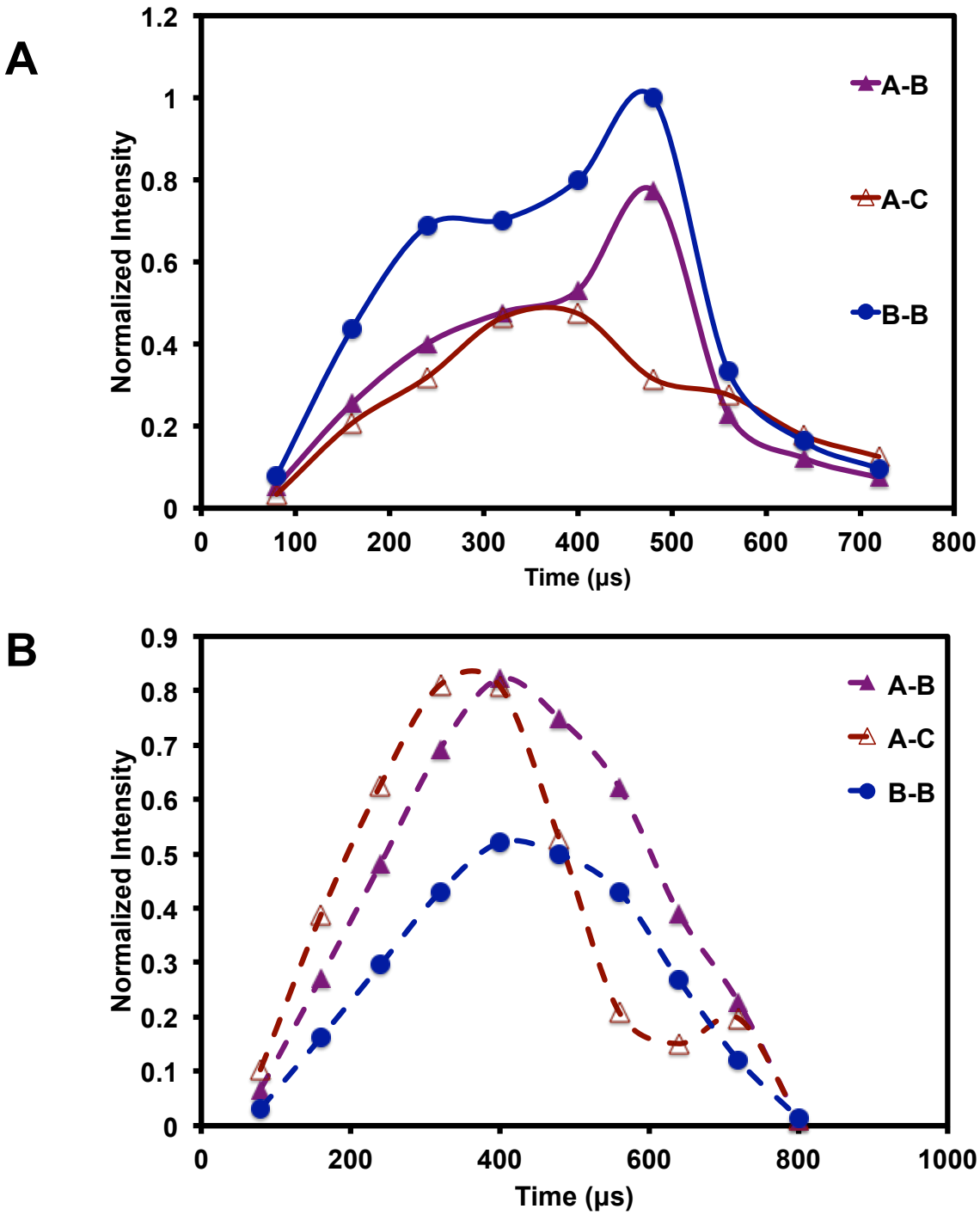

Figure 4.8: POST C7 DQC buildup curves of IFMS. A) Experimental buildup curves obtained from 2D POST C7 DUMBO collected at incremented delays B) Simulated DQC buildup curves of IFMS. For all the spin pairs observed for IFMS the simulated DQC buildup curves show a slower buildup compared to the experimental curves indicating that there is additional dynamics occurring in IFMS on this timescale.

AMSA as stated above is not a proton conductor, however since it possesses numerous hydrogen-bonded sites it is an interesting salt to study from its structure. AMSA depicted in **Figure 4.9C** has a space group of P 2_1/c with cell lengths of a 7.2162(8) Å, b 14.6646(15) Å and c 9.1094(10) Å. This crystal structure has a cell volume of 960.774 $Å^3$ with a R-Factor of 3.19%, which is the smallest cell volume for all the solid acids of interest (BMSA: 984.54 $Å^3$, IMSA: 1419.59 $Å^3$ and IFMS: 1633.56 $Å^3$). This structure is compact, with short distances between cation and anion. These constraints are thought to prevent the cation rotation about the C2 axis. The anion has sufficient space to allow rotation; however it must simultaneously break six hydrogen-bonded pairs to achieve rotation. AMSA was predicted to be a promising material due to multiple hydrogen-bonded sites, however its compact, strongly H-bonded structure is found to impede reorientation and thus limit proton conductivity.

The range of bond lengths indicated by the X-ray structure of AMSA suggested that a wide range of buildup curves would be observed. The 2D DUMBO-POSTC7 can be seen in **Figure 4.9A**, where initially it was observed that the spectral resolution was substantially worse than for glycine and the other organic solid acids presented here. This is attributed to the dense H-bonded network, resulting in stronger net homonuclear dipolar couplings within this solid. From the set of 2D DUMBO-POST C7 with the varied excitation and reconversion times it was not possible to obtain consistent integrations within reasonable error. Therefore, an attempt at higher resolution was pursued through ultrafast MAS at 100 kHz to determine whether better resolution could be obtained.

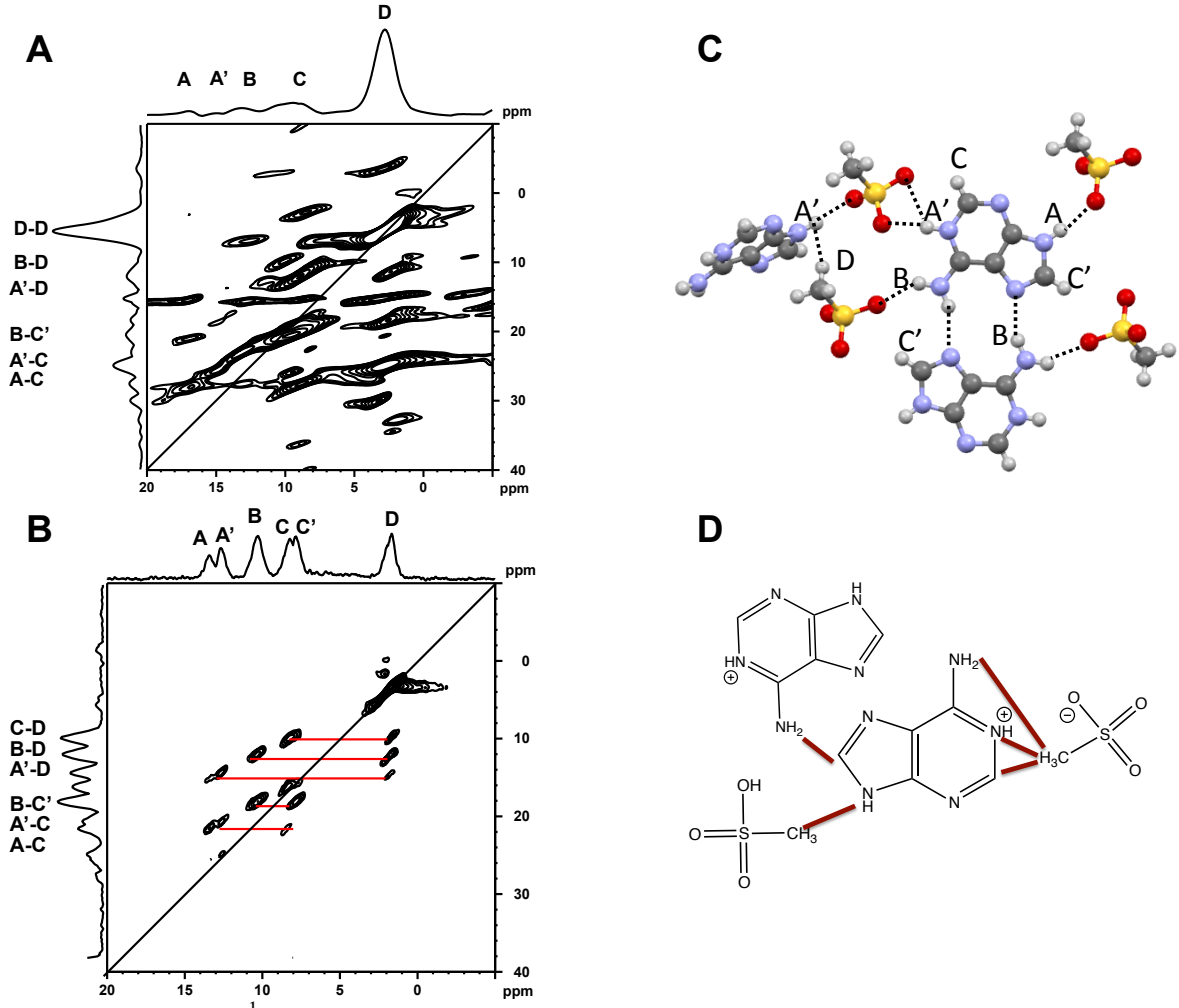

Figure 4.9: A) 2D ^{1}H 12.5 kHz MAS POST C7-DUMBO using a supercycle with 2 loops of recoupling of AMSA collected on a 500 MHz at room temperature. There are five resonances observed in the direct dimension with six dipole-dipole coupled seen in the indirect double quantum dimension. B) 2D ^{1}H 100 kHz MAS back-to-back of AMSA collected on a 900 MHz spectrometer at room temperature using a 0.85 mm probe. C) Single crystal x-ray of AMSA. D) AMSA structure with the spin pairs highlighted on the structure.

4.4.2.1 Ultra-fast Spinning Back-to-Back of AMSA

In most solid-state NMR labs spinning to 30 kHz is performed routinely and spinning at 100 kHz can be rarely achieved. To put this in perspective, ten years ago ultra-fast spinning used to be considered to be 50-60 kHz and it is now over 100 kHz.[31,32] To obtain higher resolution simply increasing the MAS rotation frequency was implemented. For POST C7 measurements

the strength of the pulse is required to be equal to seven times the spinning speed (as explained in Chapter 2), therefore this pulse sequence is not feasible at ultra-fast spinning speeds. This limits the upper MAS rate to 12.5 kHz to have the largest bandwidth from pulse strength. Here the *back-to-back* DQ recoupling sequence is chosen, as it is not correlated between pulse power levels and spinning speed, such that higher MAS speeds may be used.

Figure 4.9B shows the 2D ^{1}H 100 kHz MAS BaBa of AMSA. At high spinning speeds six different proton sites are revealed in the single quantum dimension. There is one aliphatic site at 1.7 ppm the methyl group on the anion, two aromatic sites can be observed at 7.9 and 8.3 ppm that represents each side of the aromatic ring. Three hydrogen-bonded sites are observed at 10.3, 12.7 and 13.5 ppm that can participate in proton conduction throughout this salt. The 2D double quantum spectrum depicts seven homonuclear dipole-dipole coupled spin pairs as seen in **Figure 4.9D**. The sites that are involved with proton conduction are the hydrogen-bonded sites. In this salt, there are three hydrogen bonded sites which are labeled A, A' and B. All three sites participate in a homonuclear dipole-dipole coupling with either the aromatic or the methyl group. Both protons on the aromatic ring possess dipole-dipole coupling to themselves; a sign that the aromatic rings are close in space and thus may not conduct protons via a ring flip mechanism. There are three dipole-dipole coupled pairs from the methyl group on the anion to the cation. These hydrogen bonds prevent the anion from rotating freely to aid in proton conduction. DQC buildup curves could not obtained due to the timing that was required for the pulse sequence. However, we can infer that the dipole-dipole couplings are very strong due to the fact they appear even with 100 kHz of spinning since at this spinning speed the sample temperature approaches 60°C. This is also confirmed from the short intermolecular distances that AMSA possesses, which are ~2.5 Å.

To understand the local and macroscale mobility for BMSA, IMSA and IFMS the hydrogen bonded protons involved in proton conduction are compared using both the DQC buildup curves and their proton conductivities. The experimental and simulated DQC buildup curves are shown in **Figure 4.10A** and **Figure 4.10B**. The comparisons between the simulated and experimental datasets show that the IFMS DQ response is the most attenuated relative to its simulation based on a rigid lattice. From this we conclude that the local dynamics within the H-bonded network of IFMS are faster than that observed in the corresponding IMSA and BMSA data sets. Since the conductivities are similar for BMSA, IMSA and IFMS the higher dynamics observed for IFMS from NMR have a significant impact showing that improved pellet formation; higher proton conductivities can be obtained. The DQC buildup curves for IFMS indicate all the sites behaving similar to BMSA and IMSA, thus indicating that the pathway is the same but the mechanism occurs at a higher rate to explain the higher proton conductivity.

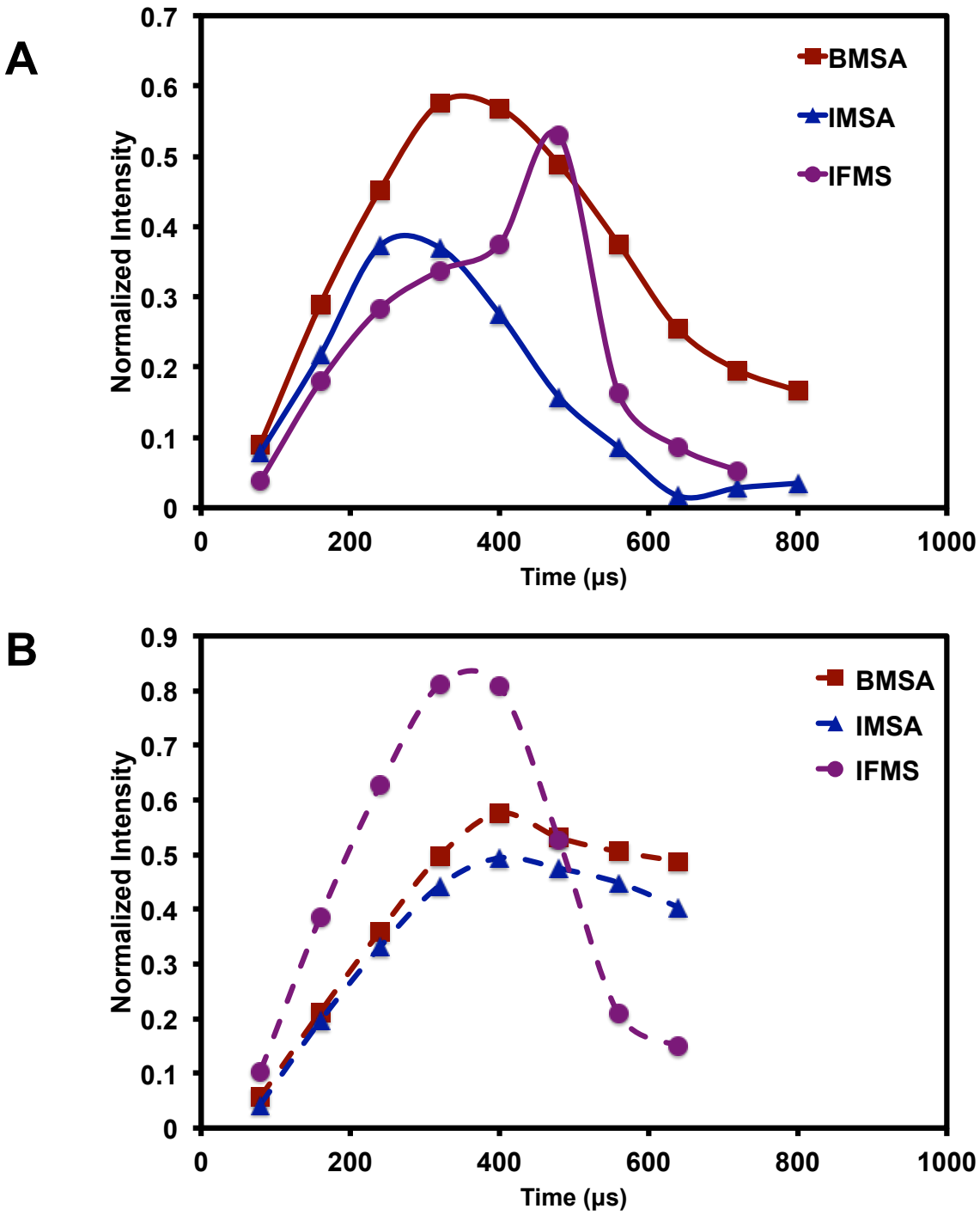

Figure 4.10: A) Experimental and B) Simulation: Dipole-dipole coupled spin pairs to conductive protons in solid acid salts. IMSA and BMSA have similar dipolar buildup curves and also similar proton conductivity. IFMS possesses the highest proton conductivity and has the slowest DQC buildup experimentally and the simulated DQC buildup is steeper than the experimental indicating additional dynamics on this timescale.

4.5 **Conclusion**

Predictions of proton conductivity and pathways can be concluded from POST C7 DQC buildup curves. For AMSA the proton conductivity was too low to be relevant and possessed the highest dipole-dipole coupling. With BMSA, IMSA and IFMS all have a dipolar coupling with the hydrogen-bonding site (A, responsible for proton conduction) with their aromatic rings. All three A-B dipole-dipole coupled pairs in all the salts possess similar intermolecular distances. BMSA and IMSA have similar proton conductivity at room temperature and their DQC buildup curves are also similar. For IFMS the proton conductivity obtained from EIS is an order of magnitude greater than that measured for BMSA and IMSA. The IFMS buildup curve is shallower than IMSA and BMSA depicting the additional mobility that the salt possesses, which allows for the higher proton conductivity at room temperature that can be obtained.

4.6 References

1. M, V. & RG, G. -SPINEVOLUTION: a powerful tool for the simulation of solid and liquid state NMR. *J Magn Reson* **178,** (2006).
2. Mauritz, K. A. & Moore, R. B. State of understanding of Nafion. *Chem. Rev.* **104,** 4535–4585 (2004).
3. Carrette, L., Friedrich, K. A. & Stimming, U. Fuel Cells - Fundamentals and Applications. *Fuel Cells* **1,** 5–39 (2001).
4. Baschuk, J. J. & Li, X. Carbon monoxide poisoning of proton exchange membrane fuel cells. *Int. J. Energy Res.* **25,** 695 (2001).

5. Li, Q., He, R., Jensen, J. O. & Bjerrum, N. J. Approaches and Recent Development of Polymer Electrolyte Membranes for Fuel Cells Operating above 100 °C. *Chem. Mater.* **15,** 4896–4915 (2003).
6. Haile, S. M., Boysen, D. A., Chisholm, C. R. I. & Merle, R. B. Solid acids as fuel cell electrolytes. *Nature* **410,** 910–913 (2001).
7. Noda, A. *et al.* Bronsted acid-base ionic liquids as proton-conducting nonaqueous electrolytes. *J. Phys. Chem. B* **107,** 4024–4033 (2003).
8. Jones, D. J. & Rozière, J. in *Fuel Cells I* (ed. Scherer, G. G.) 219–264 (Springer Berlin Heidelberg, 2008). at <http://link.springer.com/chapter/10.1007/12_2008_150>
9. Yan, Z. B., De Almeida, N. E., Traer, J. W. & Goward, G. R. Dynamics of benzimidazole ethylphosphonate: a solid-state NMR study of anhydrous composite proton-conducting electrolytes. *Phys. Chem. Chem. Phys.* **15,** 17983–17992 (2013).
10. De Almeida, N. E. & Goward, G. R. Proton Dynamics in Sulfonated Ionic Salt Composites: Alternative Membrane Materials for Proton Exchange Membrane Fuel Cells. *J. Power Sources* **268,** 853–860 (2014).
11. Agmon, N. The Grotthuss mechanism. *Chem. Phys. Lett.* **244,** 456–462 (1995).
12. Traer, J. W. & Goward, G. R. The proton dynamics of imidazole methylphosphonate: an example of cooperative ionic conductivity. *Phys. Chem. Chem. Phys.* **12,** 263–272 (2010).
13. Atkins, P. *et al. Inorganic Chemistry*. (W.H. Freeman and Company, 2006).
14. Maricq, M. M. & Waugh, J. S. NMR in rotating solids. *J. Chem. Phys.* **70,** 3300–3316 (1979).
15. Chandrakumar, N. in *Annual Reports on Nmr Spectroscopy, Vol 67* (ed. Webb, G. A.) **67,** 265–329 (2009).

16. Madhu, P. K. High-resolution solid-state NMR spectroscopy of protons with homonuclear dipolar decoupling schemes under magic-angle spinning. *Solid State Nucl. Magn. Reson.* **35,** 2–11 (2009).
17. Bielecki, A. Frequency-switched pulse sequences: Homonuclear decoupling and dilute spin NMR in solids. *Chem. Phys. Lett.* **155,** 341–346 (1989).
18. Vinogradov, E. High-resolution proton solid-state NMR spectroscopy by phase-modulated Lee–Goldburg experiment. *Chem. Phys. Lett.* **314,** 443–450
19. Sakellariou, D., Lesage, A., Hodgkinson, P. & Emsley, L. Homonuclear dipolar decoupling in solid-state NMR using continuous phase modulation. *Chem. Phys. Lett.* **319,** 253–260 (2000).
20. Hohwy, M., Jakobsen, H. J., Eden, M., Levitt, M. H. & Nielsen, N. C. Broadband dipolar recoupling in the nuclear magnetic resonance of rotating solids: A compensated C7 pulse sequence. *J. Chem. Phys.* **108,** 2686–2694 (1998).
21. Brown, S. P. & Spiess, H. W. Advanced solid-state NMR methods for the elucidation of structure and dynamics of molecular, macromolecular, and supramolecular systems. *Chem. Rev.* **101,** 4125–4155 (2001).
22. Ye, G., Janzen, N. & Goward, G. R. Solid-state NMR study of two classic proton conducting polymers: Nafion and sulfonated poly(ether ether ketone)s. *Macromolecules* **39,** 3283–3290 (2006).
23. JP, B., C, T., C, F. & SP, B. Determining relative proton-proton proximities from the build-up of. *Phys Chem Chem Phys* **11,** 6941 (2009).
24. Yuan, X., Wang, H., Colinsun, J. & Zhang, J. AC impedance technique in PEM fuel cell diagnosis—A review. *Int. J. Hydrog. Energy* **32,** 4365–4380 (2007).

25. Springer, T. E., Zawodzinski, T. A., Wilson, M. S. & Gottesfeld, S. Characterization of polymer electrolyte fuel cells using AC impedance spectroscopy. *J. Electrochem. Soc.* **143,** 587–599 (1996).

26. HA, S. & Hayamizu, K. Chemical shift standards in high-resolution solid-state NMR (1) 13C, 29Si, and 1H nuclei. *NOTES* **64,** 685–687 (1991).

27. Freeman, R. & Hill, H. D. W. Fourier Transform Study of NMR Spin--Lattice Relaxation by ``Progressive Saturation''. *J. Chem. Phys.* **54,** 3367–3377 (1971).

28. Tycko, R. & Dabbagh, G. Double-quantum filtering in magic-angle-spinning NMR spectroscopy: an approach to spectral simplification and molecular structure determination. *J. Am. Chem. Soc.* **113,** 9444–9448 (1991).

29. Traer, J. W., Britten, J. F. & Goward, G. R. A Solid-State NMR Study of Hydrogen-Bonding Networks and Ion Dynamics in Benzimidazole Salts. *J. Phys. Chem. B* **111,** 5602–5609 (2007).

30. Albrecht, G. & Corey, R. B. The Crystal Structure of Glycine. *J. Am. Chem. Soc.* **61,** 1087–1103 (1939).

31. Cahill, L. S. *et al.* 6Li NMR Studies of Cation Disorder and Transition Metal Ordering in Li[Ni1/3Mn1/3Co1/3]O2 Using Ultrafast Magic Angle Spinning. *Chem. Mater.* **17,** 6560–6566 (2005).

32. Traer, J. W. *et al.* Unraveling the Complex Hydrogen Bonding of a Dual-Functionality Proton Conductor Using Ultrafast Magic Angle Spinning NMR. *Chem. Mater.* **18,** 4747–4754 (2006).

Chapter 5
Proton Dynamics in Sulfonated Ionic Salt Composites: Alternative Membrane Materials for Proton Exchange Membrane Fuel Cells

This chapter has been published in the Journal of Power Sources 268, 853-860, (2014). The only other co-author is G.R. Goward. The manuscript was initially prepared by me and revised with G.R. Goward and myself for submission. My contribution to this paper includes: sample preparation of the salts and salt-composites, solid-state NMR studies, EIS to determine dynamics in the salts themselves versus composites.

This chapter compares dynamics through solid-state NMR and EIS to demonstrate how an inert polymer host impacts the salts performance. Here, several solid-acids are characterized, both as pristine salts, and as polymer composites. Materials of interest include benzimidazolium trimethanesulfonate (BMSA), imidazolium trimethanesulfonate (IMSA), and imidazolium triflouromethanesulfate (IFMS). The proton dynamics of these solid acids are characterized as pure salts, and as composites, embedded into porous Teflon, by solid-state magic angle NMR. It was determined that spin lattice (T_1) relaxation of the composites are systematically lower than that of the pure salt, indicating that local dynamics are enhanced in the composites. Spin-spin relaxation (T_2*) was measured as a function of temperature to determine the activation energy for local mobility for each salt and composite. Here again, the activation energy for local proton mobility in each salt decreased after being inserted into porous Teflon. Finally, the long-range ion transport of both the salts, and the composites, were characterized using impedance spectroscopy. The IFMS-Teflon composite possessed the lowest activation energy for local proton mobility, the highest thermal stability, and the most favourable proton conductivity, among the investigated materials.

5.1 Introduction

Proton exchange membrane fuel cells (PEMFCs) are promising energy carriers for portable and automotive applications. Several limitations prevent widespread use of PEMFCs such as cost, lifetimes, and availability of infrastructure. PEMFCs which are able to operate at higher temperatures would prevent carbon monoxide poisoning of the platinum catalyst, and yield higher current densities.[1–3] Perfluorosulfonic acid ionomers such as Nafion are the most widely used PEMs due to their inherent durability, chemical stability and high proton conductivity. However, in contrast to optimal conditions for the platinum catalyst, Nafion operates optimally under humid, low temperature (<80°C) conditions.[4–6]

Nafion composites have been widely studied in literature.[7,8] A common approach is to add components to Nafion to enhance performance at higher temperatures by maintaining water within the membrane. Therefore, hygroscopic additives are inserted to enhance water retention properties under high temperature and low humidity conditions. Examples of additives include SiO_2 and TiO_2 which have been shown to maintain water content but do not contribute to proton conductivity.[9–12]

Alternatively, electrolyte materials that can operate under anhydrous conditions would be ideal to mitigate water management issues. The mechanism of anhydrous proton transport has been studied by molecular dynamics simulations, and occurs through the Grotthuss mechanism.[13,14] A class of electrolytes that fits these criteria is solid acids, which are chemically, thermally and electrochemically stable and transport protons under anhydrous conditions.[15–18] Research in this area first focused on $CsHSO_4$, however drawbacks were identified, including narrow operational temperature ranges and

significant hydration difficulties.[19,20] Previously studied organic solid acids utilized phosphate functional groups, paired with large heterocyclic cations, where it was shown that these systems have good conductivity in anhydrous conditions.[21] Phosphates possess substantial proton conductivity; however high temperatures can promote their condensation into pyrophosphates. The resultant P-O-P linkages between neighboring phosphate groups decreases proton conductivity irreversibly.[22] In contrast, sulfonate functional groups are chemically, stable and have been used within membranes under harsh environments, such as fuel cells, with great success and do not condense at high temperatures.

In this paper sulfonate-functionalized solid acids were investigated. Solid acids were synthesized using organic heterocycles such as imidazole and benzimidazole, paired with sulfonic acid derivatives to form acidic salts. However, the salts themselves do not possess the mechanical properties necessary to be formed into thin films for fuel cell and require a polymer support to be relevant for fuel cell applications.

It has been shown that ionic salts can be incorporated into polymers to provide the necessary mechanical support.[23] One example of a polymer support is polyvinylidenefluoride (PVDF), however the salt does not insert homogenously into the host polymer causing numerous non-conductive pathways. Porous Teflon is an alternative host candidate, which behaves similarly to PVDF, and when the salt was inserted a homogenous film was obtained.[24] The properties of the sulfonic acid salts, and their Teflon-composites are investigated here using a series of ^{1}H solid-state nuclear magnetic resonance (SSNMR) experiments, paired with impedance spectroscopy measurements of the proton conductivity.

5.2 Methodology

Solid state NMR is capable of probing dynamics on a localized scale. In the solid state broad ^{1}H line widths are expected due to the strong homonuclear dipole-dipole interactions, arising from the lack of molecular rate in solid samples.[25] Dipole-dipole interactions are based on the gyrometric constant (γ_i and γ_j) of the relevant nuclei (I_i, and I_j) and the distance ® and orientation (θ) between them as seen in **Equation 5.1**, where the Hamiltonian for the dipolar interaction, H_D, includes two spatially dependent terms, and a third, spin-dependent term.[26] The first two terms are based on constants, and together form the dipolar coupling constant, D_{ij}.

$$H_D = -\sum_{i>j}\left(\frac{\mu_o}{4\pi}\right)\left(\frac{\gamma_i\gamma_j\hbar}{r_{ij}^3}\right) * \frac{1}{2}(3\cos^2\theta - 1)\left[\hat{I}_z\hat{S}_z\right] \qquad \textbf{(5.1)}$$

Dipole-dipole interactions can be averaged with the use of fast magic angle spinning (MAS), which generates significant line narrowing. However by averaging these effects valuable structural information is removed. In particular, the strength of the dipole-dipole couplings can be used to determine the relative mobility of protons in a hydrogen-bonded structure. Therefore, selectively retrieving these couplings can provide unique, site-specific insight into the local dynamics. Pulse sequences such as *Back-to-Back* (BaBa) are used to recouple homonuclear dipole-dipole coupling over the timescale of the rotor period.[27,28] Strong dipole-dipole couplings will be fully excited on timescale of 2τ, where τ is equal to the rotor period (25 kHz = 40μs), whereas the signals of mobile protons will be attenuated or removed from the spectrum due to the inefficient excitation of the double-quantum coherence. In this sense, only strongly dipolar coupled signals pass through the double quantum filter (DQF). It is important to note that the lack of a DQ signal can be attributed to either to fast molecular tumbling (averaging θ or r) or long

distance (r) between the protons. Therefore, the DQ data presented here are evaluated for the relative mobility, keeping in mind the crystal lattice, and density of protons within each structure.

Spin lattice relaxation (T_1) has several different mechanisms such as dipolar, scalar, quadrupolar and chemical shift anisotropy. In this case it is assumed that dipolar relaxation is the dominate mechanism that contributes to spin lattice relaxation.[29] Investigation of salts and salt-composites will be performed here, and a change in spin lattice relaxation will be interpreted as indicative of dipole-dipole coupling changes. This interpretation is valid for the protons in these materials, as there are negligible quadrupolar or chemical shielding anisotropy interactions present.

Variable temperature (VT) MAS NMR is a routinely used technique to probe dynamics at a molecular scale. To establish linewidth trends, the full width half max (FWHM) of the individual peaks are determined. The T_2* can be calculated, from FWHM (**Equation 5.2**), and is indicative of T_2 relaxation coupled with the effect of field inhomogeneity.[30,31] The behaviour of T_2* as a function of temperature follows an Arrhenius relationship, and can be used to estimate the activation of proton mobility on a localized scale.

$$FWHM = \frac{1}{\pi T_2^*} \tag{5.2}$$

Additionally, in fast exchange the chemical shift is observed trend to lower ppm values with increasing temperature. In this case, the higher thermal energy in hydrogen bonded network causes less electron shielding at the ^{1}H nucleus, and thereby lowers chemical shift.[28,32]

While ^{1}H NMR provides a local picture of the dynamics in the hydrogen bonding motif, proton conductivity is more frequently obtained *via* electrochemical impedance spectroscopy (EIS), which probes the bulk transport properties.[33] Measurements are conducted with an in-plane (composites) or through-plane (salts) conductivity cell to determine the impedance of a sample and thus its conductivity.[33,34] This is a macroscale measurement of the performance of a material as an electrolyte for fuel cell systems. Conductivity measurements can be correlated with NMR data to describe the mechanism of proton transport within the composites.[21]

5.3 Experimental

Benzimidazolium methanesulfonate (BMSA) and imidazolium methanesulfonate (IMSA) were synthesized by dissolving benzimidazole or imidazole in minimal amounts of methanol and adding methanesulfonic acid to maintain a 1:1 molar ratio. The solution was left to crystallize the product. Crystals were heated at 80°C oven for 24 hours to remove any trapped solvent. Imidazolium trifluoromethanesulfonate (IFMS) was purchased from Sigma Aldrich. Porous Teflon was purchased from Millipore with 0.45 μm pores and 47 μm in thickness. To produce composites porous Teflon was soaked in a salt solution for 24 hours. IMSA and IFMS were made into 1 M salt solutions and the BMSA was made into a 0.5 M salt solution due to solubility limitations. The composite was placed into an 80 °C oven for 24 hours. The salts are referred to by their acronyms and the corresponding composites as, for example, BMSA-Teflon, indicating the salt embedded in the Teflon membrane.

Differential scanning calorimetry was performed on a Mettler Toledo FP90 TA Cell heating 20°C/min from 30°C to 300°C under atmospheric conditions. Heat flow was

calibrated using indium metal. All samples were packed into aluminum pans with approximately 10 mg of material before placing into instrument. Thermogravimetric analysis (TGA) was performed on a NETZSCH STA 409 PC/PG instrument referenced with Al_2O_3 with a 5°C temperature ramp from 35°C to 700°C under air.

NMR experiments were performed on a Bruker Avance 500 spectrometer, equipped with an 11.7 T magnet. All samples were referenced to adamantane (1.85 ppm for ^1H).[35] For salt samples NMR was conducted with a 2.5 mm diameter rotor spinning at 25 kHz. Solid state ^1H NMR spectra were acquired with a 90° pulse length of 2.5 μs. Delays set were chosen to be 5 times greater than the T_1 of the sample. T_1 measurements were obtained using a saturated recovery method.[36] Composite samples were measured with a 4 mm diameter rotor spinning at 10 kHz. Solid state ^1H NMR spectra were acquired with a 90° pulse length of 5 μs. Fitting of the NMR peaks to determine their full width half max (FWHM) was performed in Mathematica (Version 8).[37]

Double quantum experiments were obtained with the *back-to-back* sequence (BaBa). Experiments were performed on a 2.5 mm rotor spinning at 25 kHz that was rotor synchronized for 2τ (80 μs periods). Experiments were collected with 16 scans to complete the full phase cycle.

Variable temperature bearing gas was heated for all variable temperature experiments and conducted in the 300-350 K range. Temperatures were calibrated using a $SmSn_2O_7$ temperature calibration.[38]

Single crystal X-ray experiments were obtained by first dissolving the salt in saturation in methanol. All crystals obtained were clear and colourless. X-ray diffraction

measurements were conducted with Bruker D8 diffractometer with a SMART6000 CCD detector. The radiation source was a Cu K-α with a wavelength of 1.54178 Å.

Electrochemical impedance spectroscopy was obtained on a Gamry Reference 600 potentiostat. Pure salts were pressed into pellets, sintered at 130°C overnight and covered in a 30 nm of gold on both sides for through-plane conductivity measurements. Composites samples were analyzed using an in-plane conductivity cell. The samples were cut into 0.5x2 cm to be placed into the conductivity cell. The cell was placed in an oven with anhydrous conditions to equilibrate for one hour before proton conductivity measurements with a temperature range of 80°C to 120°C. Experiments were conducted at a DC voltage of 0.5 V with amplitude of 50 mV with frequency sweep from $1.0x10^6$ to $1.0 x10^3$ for pure salts and $1.0 x10^5$ to 1 Hz for composites.

5.4 Results and Discussion

Producing anhydrous salt-host composites for fuel cells would be beneficial to increase the longevity of the catalyst layer, enhance proton conductivity and minimize water issues within the cell. Sulfonated salts were investigated by themselves and within a Teflon host for the applicability as an electrolyte for fuel cell applications. Here these salts and composites were studied on a molecular scale by solid state NMR to observe proton mobility. This information can be used to explain how the proton conductivity is affected by the hydrogen-bonded network within the salts and composites.

5.4.1 Single Crystal X-Ray Diffraction

Single crystal x-ray diffraction was performed to identify the H^+ transport pathways by fully describing the hydrogen bonding motifs, unit cell coordinates and space group. The resulting structural data, including space group unit cell parameters are

reported in **Figure 5.1** and **Table 5.1**. As seen in **Figure 5.1A** the BMSA salt structure has two hydrogen bonds of the same length and the same local environment. The cation rotation may be inhibited, due the size of the heterocycle whereas the anion appears to have the ability to freely rotate, due to the labile nature of the two attached hydrogen bonds. Therefore, proton conduction is proposed to occur in this salt *via* the rotation of the anion. In contrast, as shown in **Figure 5.1B,** the cation and the anion in the IMSA salt have space to freely rotate. In **Figure 5.1C** the ions in the IFMS salt structure are spaced comparatively further apart, creating ample space for rotation of the cation. The anion experiences steric hindrance between the fluorinated methyl groups which may inhibit its reorientation. Only the sulfonate group appears spatially able to exhibit free rotation in IFMS; however it must break three hydrogen bonds in order to participate in proton conductivity. These structural constraints will be further considered in the context of the conductivity and local mobility, as assessed by solid state NMR.

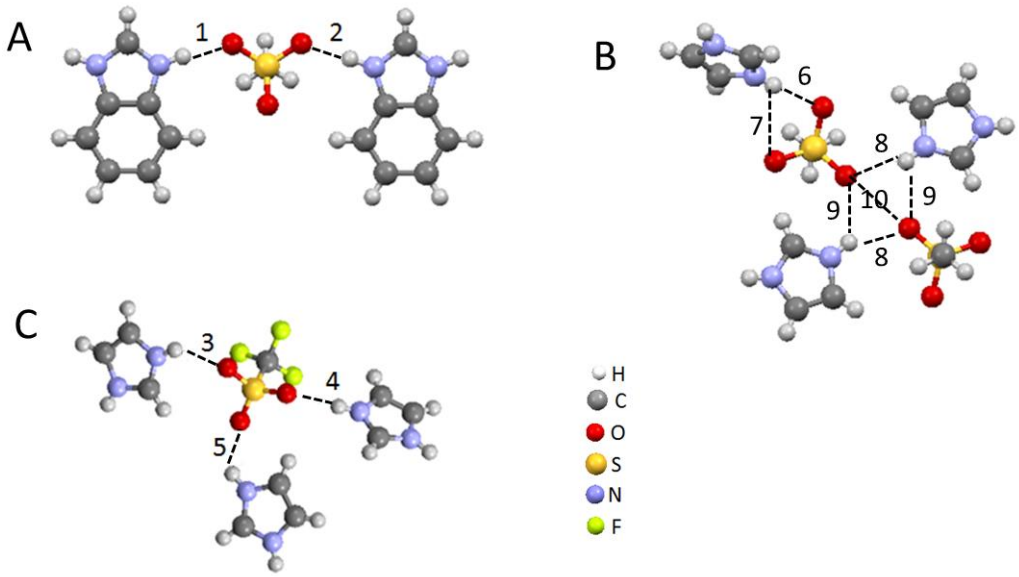

Figure 5.1: Single Crystal X-ray from saturated salt methanol solutions A) BMSA, B) IMSA and C) IFMS

Table 5.1: Lengths of bonds for BMSA (space group: P2_1 2_1 2_1), IFMS (space group: P4_3 2_12) and IMSA (space group: P*bca*) Single Crystal X-ray.

Compound Name	Bond Number	Length (Å)	a (Å)	b (Å)	c (Å)
BMSA (A)	1	2.710(4)	5.665(3)	9.604(4)	18.096(9)
	2	2.701(4)			
IFMS (B)	3	2.841(3)	8.100(3)	8.100(3)	24.898(2)
	4	2.965(3)			
	5	2.837(3)			
IMSA (C)	6	2.802(2)	7.959(2)	11.038(3)	16.159(5)
	7	2.831(2)			
	8	2.842(2)			
	9	3.045(2)			
	10	3.049(2)			

5.4.2 Thermogravmetric Analysis

The structures of the three solid-acids of interest are shown in **Figure 5.1**, as excerpts from the crystal structures. Initial analysis of the BMSA, IMSA and IFMS, salts was performed with DSC. The melting points for BMSA, IMSA and IFMS were determined to be 240°C, 191°C, and 189°C respectively. Based on the relative melting points, IFMS was predicted to show an onset of proton dynamics at the lowest temperature. For salt-polymer composite samples, salt loadings were determined by TGA. It was found that the salt loadings for BMSA-Teflon, IMSA-Teflon and IFMS-Teflon, and were 28%, 34% and 44% respectively as seen in **Figure 5.2**. The salt loadings are not equivalent for the three composites due solubility limits of each salt in methanol. Teflon swells in methanol allowing the pores to expand to host the salt in solution and remain in the pores when Teflon was dried resulting in a composite. Salts in the composites possessed a higher thermal stability than the salts themselves, as shown by the relative inflection points of the TGA curves. The inflection points for BMSA-Teflon, IMSA-Teflon and IFMS-Teflon, were 278°C, 301°C and 370°C respectively. IFMS-Teflon possesses the highest salt loading and the highest thermal stability

compared to the other salt-Teflon composites. Previous studies by Yan et al. investigated organic solid acids in Teflon composites with scanning electron microscopy (SEM).[24] It was shown that the salt formed as a phase-separated microstructure that incorporated throughout the Teflon pores.

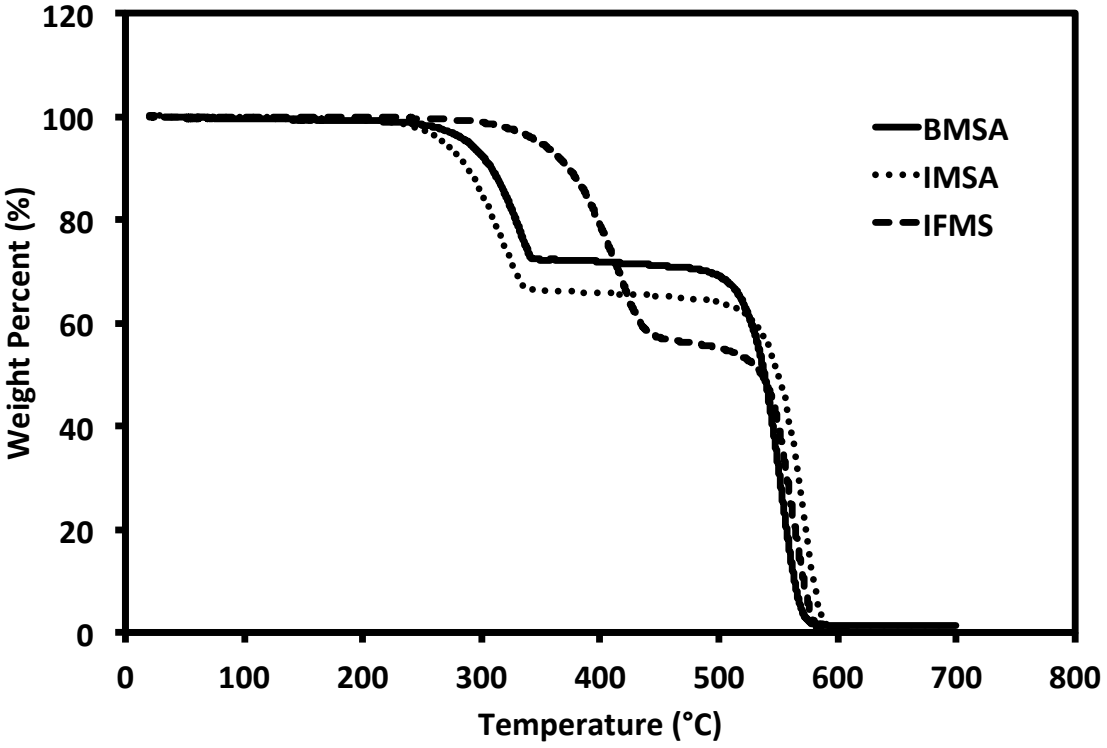

Figure 5.2: TGA of BMSA-Teflon, IFMS-Teflon and IMSA-Teflon in air, 10°C/min heating rate

5.4.3 ^{1}H MAS NMR of Organic Solid Acids

The ^{1}H MAS NMR spectra (above) and ^{1}H DQF NMR spectra (below) of the three compounds are shown in **Figure 5.3.** Spectra were acquired at 25kHz MAS, and exhibited no significant spinning sideband intensity. The spectra can be divided into three regions of interest; hydrogen-bonded (16-9 ppm), aromatic (9-5 ppm) and the aliphatic (5-0 ppm).

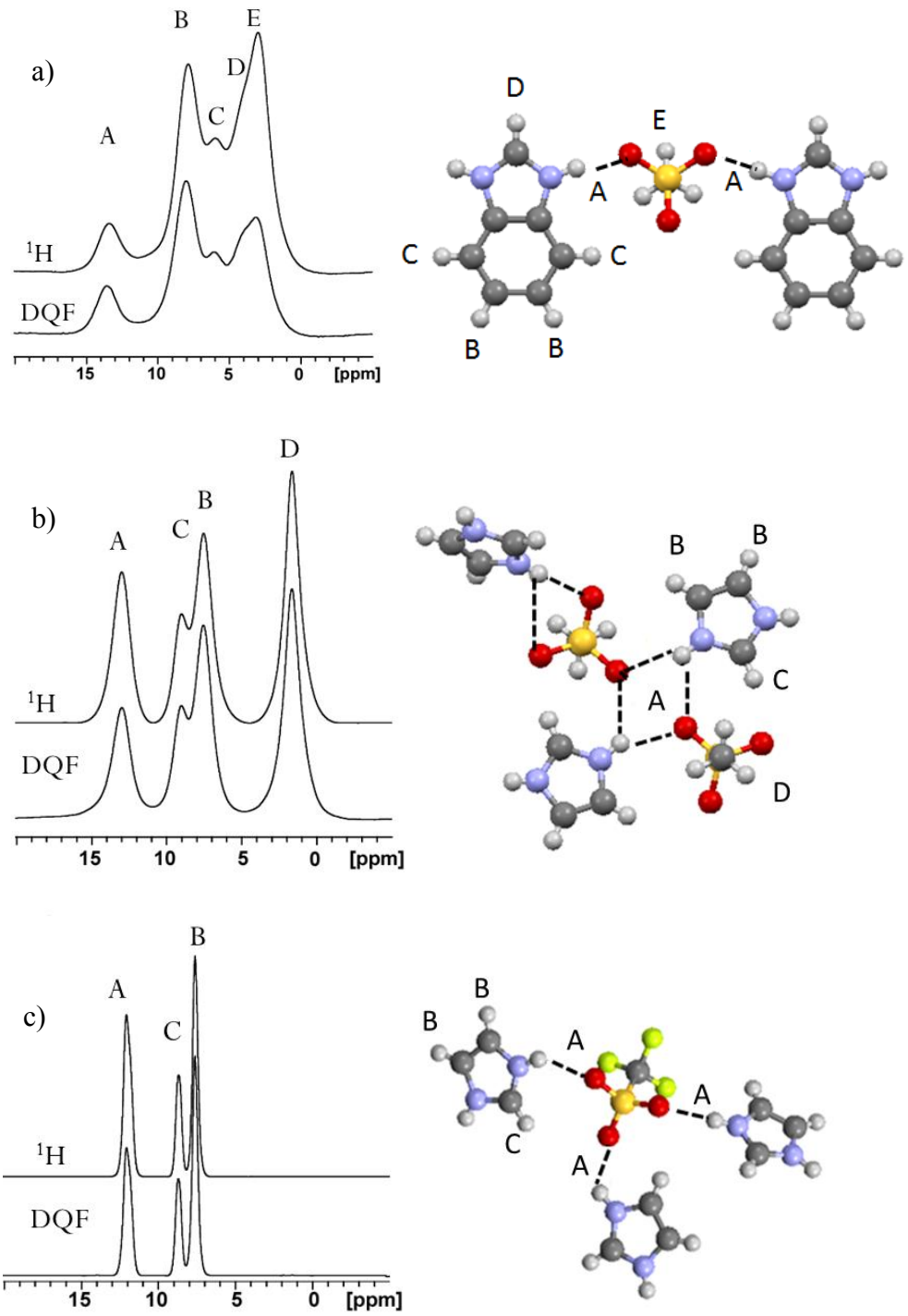

Figure 5.3: ^{1}H MAS NMR spectra @ 25kHz (4 scans) and ^{1}H DQF NMR (16 scans) of a) BMSA all peaks attenuate by the same degree b) IMSA hydroxyl peak has decreased intensity suggesting dynamics c) IFMS hydroxyl peak attenuates slightly more than remainder of peaks suggesting dynamics

5.4.3.1 BMSA: In BMSA salt one hydrogen-bonded peak is observed at 13ppm (A), three aromatic peaks at 8 ppm (B), 6 ppm (C) and 4 ppm (D) and one aliphatic proton at 3 ppm (E). Variable temperature NMR indicates dynamics at hydrogen-bonded peak, which narrows as a function of temperature (**Figure 5.4**). The ^{1}H NMR spectra of the BMSA salt exhibit line narrowing as a function of temperature, indicative of local dynamics. The FWHM was correlated to T_2* to determine the activation energy of proton mobility, which was 9.7±0.1 kJ/mol as seen in **Table 5.2**.

Table 5.2: Activation Energies acquired from Arrhenius analysis of T_2^* data for IMSA, BMSA and IFMS Salts and Composites acquired under Variable Temperature ^{1}H MAS NMR.

Compound	Activation Energy (kJ/mol)	
	NMR	EIS
BMSA	9.7±0.1	29.5±1.5
IMSA	7.4±0.1	21.2±0.1
IFMS	5.5 ±0.6	29.6±0.8
BMSA-Teflon	5.6±0.2	N/A
IMSA-Teflon	4.0±0.1	29.8±0.9
IFMS-Teflon	3.6±0.2	21.4±0.6

Another approach to observe proton mobility was to perform a VT ^{1}H DQF NMR study. The ^{1}H DQF NMR data shown in **Figure 5.3** for BMSA none of the peaks are completely removed by the double quantum filter (under recoupling = $2\tau_r$) , however they are attenuated significantly, relative to the direct-excitation spectrum, (over 90%) which is attributed to local mobility. As the temperature increased from 300-350 K the intensity from the hydrogen-bonded proton decreased substantially due to increasing mobility. This qualitative method to determine how the hydrogen-bonded proton attenuates compared with the attenuation of the aliphatic region. The relative degree of attenuation

at the hydrogen-bonded proton, as compared to the other (covalently bound) protons was 30±2% and 15±2% respectively. Therefore, the hydrogen-bonded proton is inferred to possess a higher degree of mobility on a timescale of 80 μs. This statement is based on the assumption that the static (low temperature) homonuclear dipolar couplings for all protons in the structure would be approximately equivalent when summed over the proton-rich structure. Full simulation of the multi-spin-dynamics is beyond the scope of this study.[39]

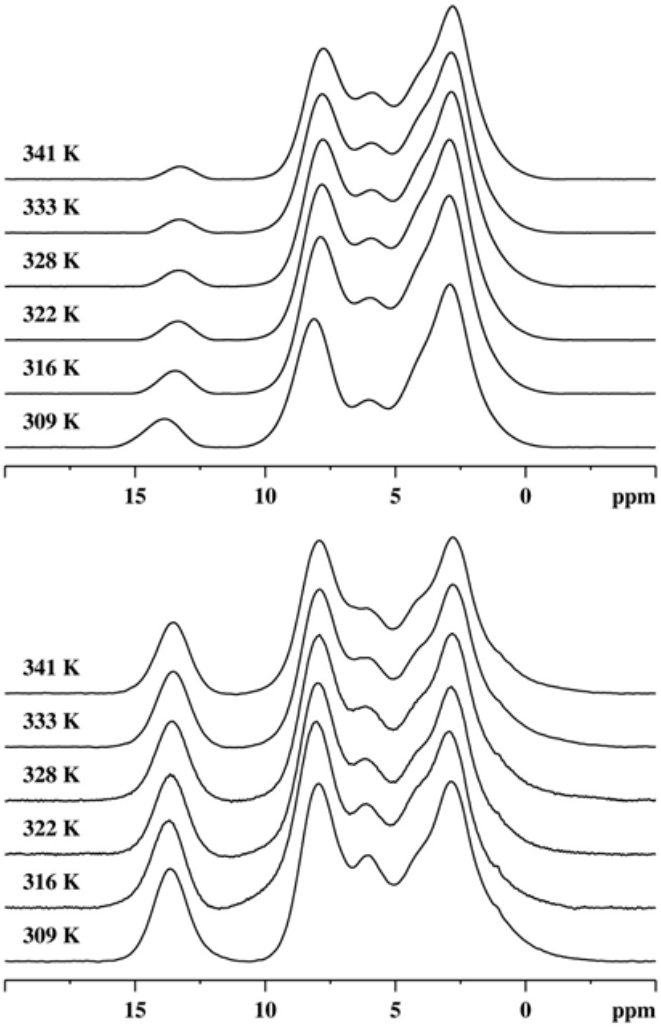

Figure 5.4: VT ^{1}H MAS NMR, 25 kHz, 500 MHz, 2.5 mm probe A) BMSA salt and B) BMSA-Teflon composite

5.4.3.2 IMSA: The ^{1}H NMR spectrum of IMSA has four main proton resonances including the hydrogen-bonded peak at 13.0 ppm (A), the aromatic peaks at 7.6 ppm (B) and 9.1 ppm (C) and the aliphatic peak at 1.7 ppm (D) as seen in **Figure 5.5**.[40] The hydrogen-bonded peaks in IMSA and BMSA have equivalent chemical shifts, indicating similar environments around the protons. IMSA hydrogen-bonded and aromatic protons have attenuated the same degree and the aliphatic region attenuated by the greatest amount. A similar result was also observed by Traer et al.[40] This is typical of the rapidly rotating methyl groups, which are inherently decoupled through this mobility.[41] With VT ^{1}H MAS NMR the hydrogen-bonded proton shifts to lower frequency as expected, which is consistent with a Grotthuss mechanism of proton transport.[42] Additionally, the FWHM decreased as a function of temperature and the activation energy of proton mobility in IMSA was 7.4±0.1 kJ/mol, which is lower than BMSA, consistent with the structural interpretation above. Also, with the ^{1}H DQF NMR VT the hydrogen-bonded proton attenuated significantly, a total of 68±2%, whereas the aromatics were attenuated by only 10±1%. Since the hydrogen-bonded proton attenuated significantly compared to the other protons in the system that it can be concluded it possesses higher degree of mobility. However, this degree of mobility could be due to a rapid local dynamics or a long-range transport contributing to proton conductivity. To confirm whether this local mobility of the H-bonds leads to long-range ion transport, the bulk ion transport properties are measured (below).

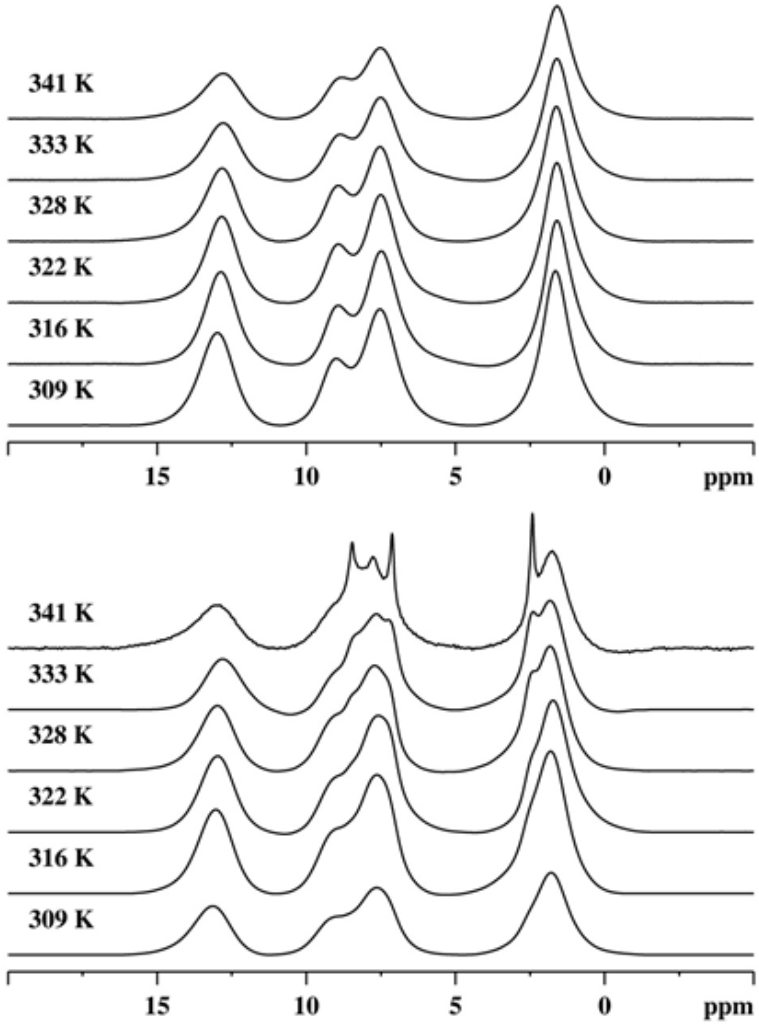

Figure 5.5: VT ^{1}H 25 kHz MAS NMR A) IMSA salt and B) IMSA-Teflon composite

5.4.3.3 IFMS: The third structure of interest, IFMS has three protons shifts 11.4 ppm for the hydrogen-bonded peak (A), 8.1 ppm for the first aromatic proton (C) and 7.1 ppm for the second type of aromatic proton (B). The peaks in this spectrum are significantly narrower than BMSA and IMSA. This is attributed to the lower homonuclear ^{1}H-^{1}H dipole-dipole coupling in this fluorinated structure, relative to the others. Thus, IFMS has the most dilute homonuclear dipolar-coupling network of the salts considered here. In the variable temperature ^{1}H MAS NMR spectra, all the peaks

narrow uniformly as a function of temperature as seen in **Figure 5.6**. A correlation was determined for the T_2* in an Arrhenius plot. The activation energy was the lowest of the three salts being 5.5±0.6s kJ/mol as seen in **Table 5.2**. In the ^{1}H DQF MAS NMR spectrum the protons have greatly attenuated in all regions suggesting either high mobility in all protons present or the absence of close neighbors (<3.5 Å).[43] VT ^{1}H MAS NMR depicts the aromatic protons decreasing by 14±1% and the hydrogen-bonded region by 19±1%. This was not as a dramatic difference as the other salts however, since the dipole-dipole coupling with IFMS was small initially, large changes are not expected.

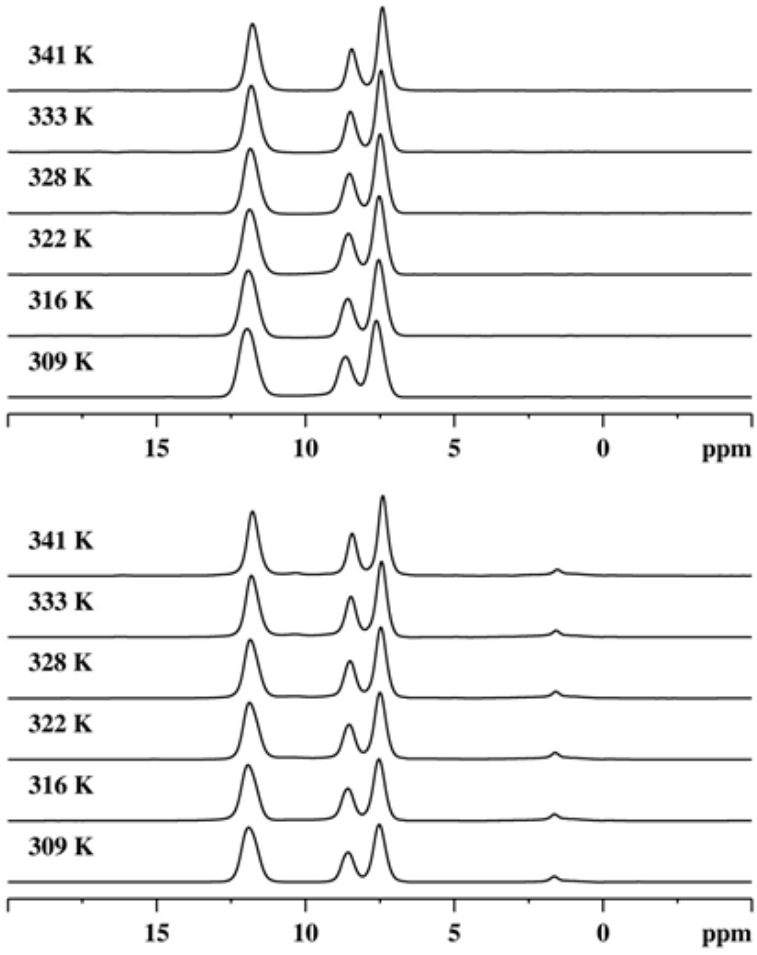

Figure 5.6: VT ^{1}H 25 kHz MAS NMR A) IFMS salt and B) IFMS-Teflon composite

5.4.4 ^{1}H NMR of Salt-Teflon Composites

Further comparison was made in the ^{1}H MAS NMR spectra of the salt-Teflon composites, utilizing the relaxation properties of the salts, as compared to their composites, as a measure of the tightness of the local hydrogen-bonding networks. Spin lattice relaxation decreased from 5.5±0.1s, for the pure BMSA salt, to 4.5±0.3s for BMSA-Teflon composite, indicating that dipole-dipole interactions have decreased modestly from pure salt to composite (**Table 5.3**). This is supported with the change of activation energy from 9.7±0.1 kJ/mol to 5.6±0.2 kJ/mol for the BMSA salt and BMSA-Teflon respectively as seen in **Table 5.2**. Here, shortened T_2 relaxation times depicts higher local mobility, which is expected from the interaction between salt and Teflon, due to the lack of long-range crystallinity, imposed by the membrane pore structure. A shorted T_2* relaxation does not uniquely imply more rapid proton-transport processes. Nevertheless, it was expected that additional dynamics would occur while inserted into the polymer support, as defects in the packing-structure are thought to enable Grotthuss-mechanism transport.[44]

Table 5.3: T_1 Relaxation Times for BMSA, IMSA and IFMS Salts and Composites.

	BMSA	IMSA	IFMS
Salt	5.5s ± 0.1s	2.1s ± 0.1s	8.1s ± 0.1s
Composite	4.5s ± 0.3s	0.30s ± 0.02ms	5.1s ± 0.1s

The IMSA-Teflon composite exhibited a decrease in spin relaxation of 2.1±0.1s to 0.30±0.01s, where the difference between salt and membrane is larger than between BMSA and BMSA-Teflon (**Table 5.3**). This larger difference is attributed to a more substantial decrease in the strength of dipole-dipole coupling, due to proton dynamics.

The activation energy lowered as well from 7.4±0.1 kJ/mol to 4.0±0.1 kJ/mol. The activation energy of IMSA-Teflon is significantly lower than BMSA-Teflon composite.

As observed from previous composites, the IFMS-Teflon spin lattice relaxation decreased significantly from pure IFMS salt from 8.1±0.1s to 5.1±0.1s as seen in **Table 5.3**. The activation energies behaved in with the same trend as previous salts and composites of 5.5±0.6 kJ/mol and 3.6±0.2 kJ/mol for IFMS salt and IFMS-Teflon respectively. This composite thus exhibits the lowest activation energy for proton motion, of all of the composites studied here. Comparing this trend in local mobility, as assessed by ^{1}H NMR with bulk properties of charge transport will allow conclusions to be drawn, regarding the proton transport mechanism.

5.5 Proton Conductivity

Bulk proton conductivity measurements were conducted between 80°C to 120^{o}C under anhydrous conditions. Trends are established between the salts and their composites, and among the pristine salts. All of the pristine salts exhibited proton transport throughout the temperature range of interest with similar conductivities as seen in **Figure 5.7**. Activation energies were obtained for the salts through the Arrhenius plot of proton conductivity were 29.5±1.5, 21.2±0.1 and 29.6±0.8 for BMSA, IMSA and IFMS respectively. The activation energies are higher with bulk proton conductivity measurements than ^{1}H MAS NMR as is often observed.[24,28] This is the result of the influence of grain boundaries on long-range conductivity, whereas ^{1}H MAS NMR measures localization motion. Nevertheless, the trends in local dynamics and conductivity are reflected in the salt versus the corresponding composites, where both are observed to increase upon incorporation into the polymer host.

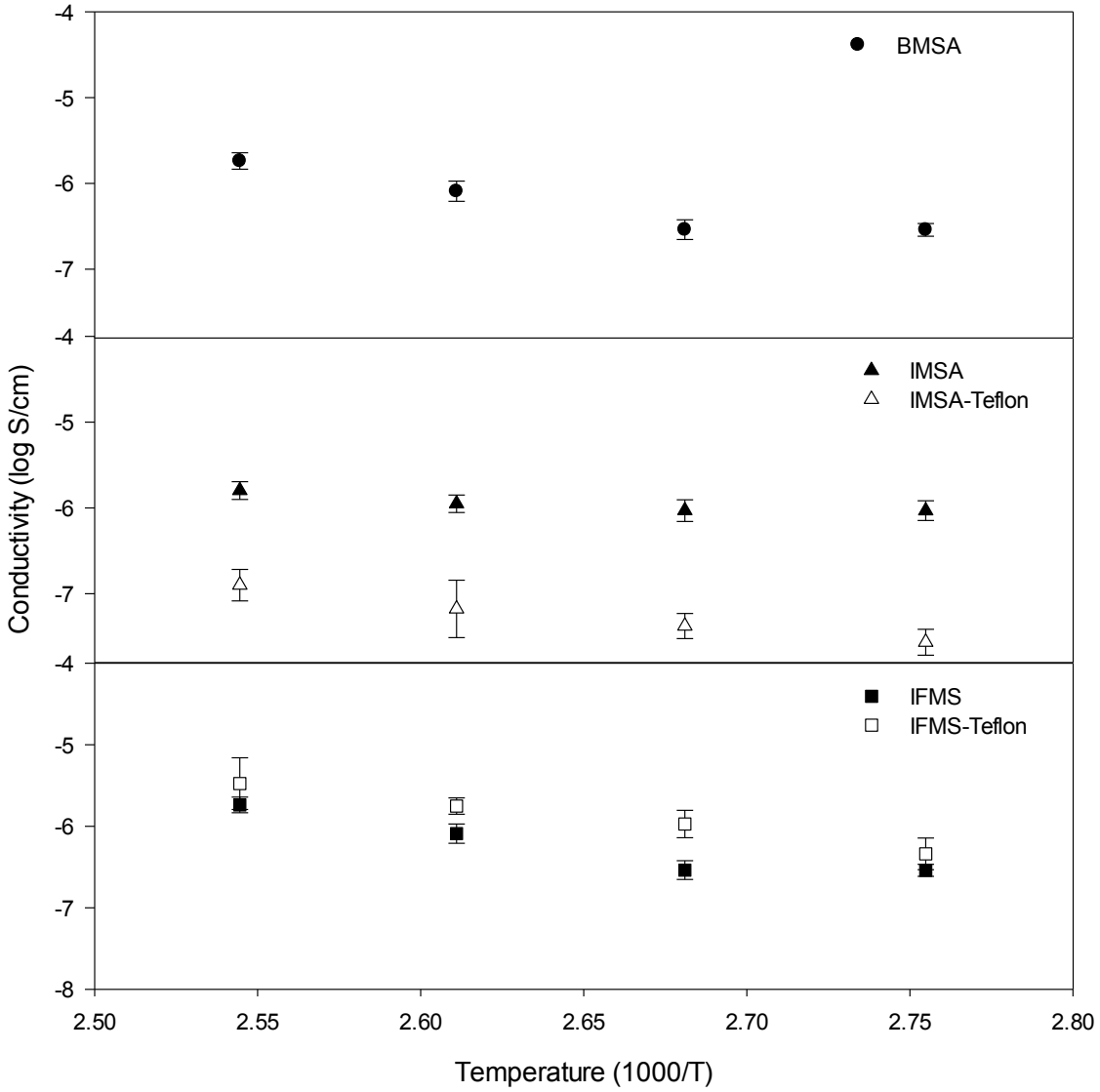

Figure 5.7: Proton conductivity data of BMSA, IMSA, IMSA-Teflon, IFMS and IFMS-Teflon under anhydrous conditions, acquired by impedance spectroscopy.

The composites exhibited some variability in their conductivities. Surprisingly, the BMSA-Teflon composite did not exhibit bulk ionic conductivity, although the parent salt had modest H^+ transport. The non-conductive behaviour is attributed to the lower salt loading, which was substantially lower than the other two composites. For IMSA-Teflon the proton conductivity is lower than the pristine salt. This could be again due to the

packing arrangement within Teflon inhibiting long-range transport due to a low salt loading within the host. Having a low salt content within Teflon reduces the number of charge carriers, and the connectivity within the hydrogen-bonded network, reducing the overall conductivity. This is confirmed by the proton conductivity activation energy for IMSA-Teflon of 29.8±0.9 kJ/mol the increase in activation energy is due to the spacing of the salt in the Teflon host that reduced the proton conductivity. This is found for the first two composites, despite indications of enhanced local mobility from the NMR studies described above.

The best performance was measured for the IFMS-Teflon composite. In this case, the conductivity is higher than the pristine salt, which is attributed to the higher salt loading facilitating long-range transport as well as the mechanical support of the host to facilitate proton transport. Thus, for the third composite, the combination of enhanced local dynamics, as revealed by NMR, and sufficient salt loading, resulted in a successful synergy between the salt and the host, and an overall improvement of the long-range ion transport in the resulting material. This is confirmed by the proton conductivity activation energy of the IFMS-Teflon to 21.4±0.6 kJ/mol which was lower than the pure salt of 29.6±0.8 kJ/mol. This material still does not compete with Nafion fully hydrated with proton conductivity 0.1 S/cm however at high temperature in anhydrous conditions IFMS-Teflon is competitive with Nafion, where its conductivity drastically decreases to $1.5x10^{-8}$ S/cm.[7]

5.6 Conclusion

Solid-state NMR showed that the T_1 relaxation is uniformly decreased when salts are incorporated into a Teflon polymer host. Similarly, the activation energy for local

proton mobility, derived from the ^{1}H line-narrowing trends of the hydrogen-bonded proton, decreased when the solid-acid salts were placed into the Teflon framework. Variable temperature ^{1}H DQF NMR depicted higher attenuation of the hydrogen bonded proton in composite form than the salt itself showing that dynamics are increased in the polymer framework. The three pristine solid-acids demonstrated similar bulk proton conductivities, however different conductivities were achieved when inserted into the Teflon membrane support. BMSA-Teflon did not conduct ions, due to the low salt loading that it possessed. IMSA-Teflon conductivity was lower than the pristine salt, again because of the salt loading and packing arrangement in the host. IFMS-Teflon possessed higher conductivity than the salt itself by possessing the highest salt loading and thermal stability and the polymer is facilitating proton transport. These competitive conductivities were achieved in anhydrous conditions.

5.8 References

1. Baschuk, J. J. & Li, X. Carbon monoxide poisoning of proton exchange membrane fuel cells. *Int. J. Energy Res.* **25,** 695 (2001).
2. Services, E. T. *Fuel Cell Handbook*. (U.S. Department of Energy, 2004).
3. Hwang, K. S., Yang, M. C., Zhu, J., Grunes, J. & Somorjai, G. A. The molecular mechanism of the poisoning of platinum and rhodium catalyzed ethylene hydrogenation by carbon monoxide. *J. Mol. Catal. Chem.* **204,** 499–507 (2003).
4. Mauritz, K. A. & Moore, R. B. State of understanding of Nafion. *Chem. Rev.* **104,** 4535–4585 (2004).

5. Li, Q., He, R., Jensen, J. O. & Bjerrum, N. J. Approaches and Recent Development of Polymer Electrolyte Membranes for Fuel Cells Operating above 100 °C. *Chem. Mater.* **15,** 4896–4915 (2003).
6. Jung, D. H., Cho, S. Y., Peck, D. H., Shin, D. R. & Kim, J. S. Performance evaluation of a Nafion/silicon oxide hybrid membrane for direct methanol fuel cell. *J. Power Sources* **106,** 173–177 (2002).
7. Anantaraman, A. V. & Gardner, C. L. Studies on ion-exchange membranes .1. Effect of humidity on the conductivity of Nafion(R). *J. Electroanal. Chem.* **414,** 115–120 (1996).
8. Smitha, B., Sridhar, S. & Khan, A. A. Solid polymer electrolyte membranes for fuel cell applications—a review. *J. Membr. Sci.* **259,** 10–26 (2005).
9. Miyake, N., Wainright, J. S. & Savinell, R. F. Evaluation of a Sol-Gel Derived Nafion/Silica Hybrid Membrane for Proton Electrolyte Membrane Fuel Cell Applications: I. Proton Conductivity and Water Content. *J. Electrochem. Soc.* **148,** A898 (2001).
10. Shao, Y., Yin, G., Wang, Z. & Gao, Y. Proton exchange membrane fuel cell from low temperature to high temperature: Material challenges. *J. Power Sources* **167,** 235–242 (2007).
11. Rodgers, M. P., Berring, J., Holdcroft, S. & Shi, Z. Q. The effect of spatial confinement of Nafion (R) in porous membranes on macroscopic properties of the membrane. *J. Membr. Sci.* **321,** 100–113 (2008).

12. Peighambardoust, S. J., Rowshanzamir, S. & Amjadi, M. Review of the proton exchange membranes for fuel cell applications. *Int. J. Hydrog. Energy* **35,** 9349–9384 (2010).

13. Susan, M. A. B. H., Noda, A., Mitsushima, S. & Watanabe, M. Brønsted acid–base ionic liquids and their use as new materials for anhydrous proton conductors. *Chem. Commun.* 938–939 (2003). doi:10.1039/B300959A

14. Peng, Z., Morin, A., Huguet, P., Schott, P. & Pauchet, J. In-Situ Measurement of Electroosmotic Drag Coefficient in Nafion Membrane for the PEMFC. *J. Phys. Chem. B* **115,** 12835–12844 (2011).

15. Noda, A. *et al.* Bronsted acid-base ionic liquids as proton-conducting nonaqueous electrolytes. *J. Phys. Chem. B* **107,** 4024–4033 (2003).

16. Sekhon, S. S. *et al.* Morphology Studies of High Temperature Proton Conducting Membranes Containing Hydrophilic/Hydrophobic Ionic Liquids. *Macromolecules* **42,** 2054–2062 (2009).

17. Watanabe, M., Tsurumi, K., Mizukami, T., Nakamura, T. & Stonehart, P. ACTIVITY AND STABILITY OF ORDERED AND DISORDERED CO-PT ALLOYS FOR PHOSPHORIC-ACID FUEL-CELLS. *J. Electrochem. Soc.* **141,** 2659–2668 (1994).

18. Lu, W. *et al.* Use of ionic liquids for pi-conjugated polymer electrochemical devices. *Science* **297,** 983–987 (2002).

19. Haile, S. M., Boysen, D. A., Chisholm, C. R. I. & Merle, R. B. Solid acids as fuel cell electrolytes. *Nature* **410,** 910–913 (2001).

20. Haile, S. M., Chisholm, C. R. I., Sasaki, K., Boysen, D. A. & Uda, T. Solid acid proton conductors: from laboratory curiosities to fuel cell electrolytes. *Faraday Discuss.* **134,** 17 (2007).

21. Traer, J. W., Britten, J. F. & Goward, G. R. A Solid-State NMR Study of Hydrogen-Bonding Networks and Ion Dynamics in Benzimidazole Salts. *J. Phys. Chem. B* **111,** 5602–5609 (2007).

22. Atkins, P. *et al. Inorganic Chemistry*. (W.H. Freeman and Company, 2006).

23. Martinelli, A. *et al.* Physical properties of proton conducting membranes based on a protic ionic liquid. *J. Phys. Chem. B* **111,** 12462–12467 (2007).

24. Yan, Z. B., De Almeida, N. E., Traer, J. W. & Goward, G. R. Dynamics of benzimidazole ethylphosphonate: a solid-state NMR study of anhydrous composite proton-conducting electrolytes. *Phys. Chem. Chem. Phys.* **15,** 17983–17992 (2013).

25. Maricq, M. M. & Waugh, J. S. NMR in rotating solids. *J. Chem. Phys.* **70,** 3300–3316 (1979).

26. Chandrakumar, N. in *Annual Reports on Nmr Spectroscopy, Vol 67* (ed. Webb, G. A.) **67,** 265–329 (2009).

27. Brown, S. P. & Spiess, H. W. Advanced solid-state NMR methods for the elucidation of structure and dynamics of molecular, macromolecular, and supramolecular systems. *Chem. Rev.* **101,** 4125–4155 (2001).

28. Ye, G., Janzen, N. & Goward, G. R. Solid-state NMR study of two classic proton conducting polymers: Nafion and sulfonated poly(ether ether ketone)s. *Macromolecules* **39,** 3283–3290 (2006).

29. Torrey, H. C. Bloch Equations with Diffusion Terms. *Phys. Rev.* **104,** 563–565 (1956).

30. Hahn, E. L. Spin Echoes. *Phys. Rev.* **80,** 580–594 (1950).

31. Every, H. A., Zhou, F., Forsyth, M. & MacFarlane, D. R. Lithium ion mobility in poly(vinyl alcohol) based polymer electrolytes as determined by 7Li NMR spectroscopy. *Electrochimica Acta* **43,** 1465–1469 (1998).

32. Ye, G., Hayden, C. A. & Goward, G. R. Proton dynamics of nafion and Nafion/SiO2 composites by solid state NMR and pulse field gradient NMR. *Macromolecules* **40,** 1529–1537 (2007).

33. Yuan, X., Wang, H., Colinsun, J. & Zhang, J. AC impedance technique in PEM fuel cell diagnosis—A review. *Int. J. Hydrog. Energy* **32,** 4365–4380 (2007).

34. Springer, T. E., Zawodzinski, T. A., Wilson, M. S. & Gottesfeld, S. Characterization of polymer electrolyte fuel cells using AC impedance spectroscopy. *J. Electrochem. Soc.* **143,** 587–599 (1996).

35. Hayashi, S. & Hayamizu, K. Chemical Shift Standards in High-Resolution Solid-State NMR (2) ¹⁵N Nuclei. *Bull. Chem. Soc. Jpn.* **64,** 688–690 (1991).

36. Freeman, R. & Hill, H. D. W. Fourier Transform Study of NMR Spin--Lattice Relaxation by ``Progressive Saturation''. *J. Chem. Phys.* **54,** 3367–3377 (1971).

37. Wolfram Research, I. *Mathematica*. (Wolfram Research, Inc., 2010).

38. Vanmoorsel, G. J. M. P., Vaneck, E. R. H. & Grey, C. P. Pr2Sn2O7 and Sm2Sn2O7 as High-Temperature Shift Thermometers in Variable-Temperature 119Sn MAS NMR. *J. Magn. Reson. A* **113,** 159–163 (1995).

39. Ochsenfeld, C. *et al.* A study of a molecular tweezer host-guest system by a combination of quantum-chemical calculations and solid-state NMR experiments. *Solid State Nucl. Magn. Reson.* **22,** 128–153 (2002).

40. Traer, J. W. & Goward, G. R. The proton dynamics of imidazole methylphosphonate: an example of cooperative ionic conductivity. *Phys. Chem. Chem. Phys.* **12,** 263–272 (2010).

41. Spiess, H. W. Molecular dynamics of solid polymers as revealed by deuteron NMR. *Colloid Polym. Sci.* **261,** 193–209 (1983).

42. Goward, G. R., Schuster, M. F. H., Sebastiani, D., Schnell, I. & Spiess, H. W. High-resolution solid-state NMR studies of imidazole-based proton conductors: Structure motifs and chemical exchange from H-1 NMR. *J. Phys. Chem. B* **106,** 9322–9334 (2002).

43. Brown, S. P., Schnell, I., Brand, J. D., Müllen, K. & Spiess, H. W. A 1H double-quantum magic-angle spinning solid-state NMR investigation of packing and dynamics in triphenylene and hexabenzocoronene derivatives. *J. Mol. Struct.* **521,** 179–195 (2000).

44. Kreuer, K. D., Fuchs, A., Ise, M., Spaeth, M. & Maier, J. Imidazole and pyrazole-based proton conducting polymers and liquids. *Electrochimica Acta* **43,** 1281–1288 (1998).

Chapter 6
Homogeneous and Heterogeneous Sulfonated Functionalized Hosts for Organic Solid Acids for Anhydrous High Temperature Proton Exchange Membrane Fuel Cells

This chapter investigates the use of host materials that are functionalized with sulfonate groups to incorporate organic solid acids. The two polymers used were sulfonated polyetheretherketone (sPEEK) and sulfonated polysulfone (sPSU). These two polymer hosts were chosen because sPEEK sulfonates heterogeneously and sPSU sulfonates homogeneously from their sulfonation reactions. This chapter will investigate whether the homogeneity of the sulfonation and/or sulfonation of the polymer host would improve proton conduction in the subsequently formed anhydrous salt/polymer composite. The organic solid acid of choice for this study was imidazole trifluoromethanesulfonate (IFMS) due to its high proton conductivity with the Teflon composites as shown in the previous chapter relative to the other salts studied in this thesis.

Macroscale proton conductivity measurements are compared to local scale characterization through solid-state NMR. Solid-state ^{1}H NMR is used to contrast how sulfonated-functionalized hosts aid in proton conductivity, depending on the choice of polymer. Static ^{2}H NMR is also implemented to determine the hopping rates and the mechanism of proton conduction of the hydrogen-bonded proton in the polymer, IFMS and the IFMS-polymer composite.

6.1 Introduction

Proton exchange membrane fuel cells (PEMFCs) have been extensively researched to optimize their components for use in automobiles and portable applications.[1] Several limitations prevent widespread use, such as cost and operation conditions.[2] Current

operating conditions are 80°C with high humidity which leaves the platinum catalyst highly susceptible to poisoning by an irreversible reaction with carbon monoxide.[3,4] The proton exchange membrane (PEM) is the main reason for low temperature high humidity operation. The most widely used PEM is Nafion® for its chemical resistance, durability and high proton conductivity.[5] Nafion utilizes a vehicular mechanism for proton conduction, in this case water, which necessitates high humidity and low temperatures to achieve its best possible fuel cell operation. The goal of this research is to increase the operating temperature to preserve the Pt catalyst and also obtain higher energy densities by synthesizing PEMs that can operate in high temperatures and low relative humidity.

Solid acids are a promising class of materials for use in fuel cells. These materials utilize a Grotthuss mechanism for proton conduction that involves the breakage and formation of hydrogen bonds as the proton is passed through the material.[6,7] Solid acids have gained interest recently due to their high electrochemical stability, ideal melting points and high proton conductivity under anhydrous conditions.[8,9] Research in this area first focused on $CsHSO_4$; however drawbacks were identified, including narrow operational temperature ranges and significant hydration difficulties.[10,11] In this chapter organic solid acids were investigated and were prepared by combining an organic heterocycle, to act as base, with an acidic anion to produce an overall acidic salt. Organic cations that have exhibited dynamics (imidazole) and that have participated in Grotthuss-style proton transport are combined with sulfonic acids to form organic solid acid salts.[12,13] However, these organic solid acids do not possess the mechanical properties to form thin films thus a polymer support is required for these materials to be suitable for fuel cell operation.

Several solid acid-polymer composites have been synthesized where proton conductivity was increased after insertion into Teflon or PVDF.[12,14–17] However, such inert polymer supports may allow the conducting salt to leach out of the polymer due to the lack of covalent, or ionic interactions between host and salt. Therefore, combining organic solid acids with a sulfonated-functionalized hydrocarbon host has the advantage that the solid acid is coulombically interacting with the polymer through a hydrogen-bonded network to prevent the salt from leaching out of the composite as well as assisting in proton conductivity. Hydrocarbon polymers such as polybenzimidazole (PBI), sulfonated polysiloxane (sPS) and sulfonated polyetheretherketone (sPEEK) have been studied previously, to form composites and are excellent candidates for a host.[18,19] The challenge for sulfonate-functionalized hydrocarbon polymers is with higher functionalization, that increases proton conductivity, increase swelling of the polymer.[20] Unfortunately, simply operating such polymers under anhydrous high temperature conditions does not solve the problem; these polymers fail due to their dependence on water for proton conduction. We proposed here to create a novel composite, able to overcome the challenges of the pristine materials (organic solid acid, or sPEEK) themselves, achieving a synergistic interaction between polymer and salt, able to operate at ideal fuel cell conditions (120°C and no added humidity). Previously used salt hydrocarbon polymer composites were $CsHSO_4$-PVDF and SiO_2-sPEEK, however these composites were still studied in humidified conditions often with acid doping.[21,22] In the literature, there are numerous articles that discuss the sulfonation of polymers in homogeneous or heterogeneous media that affects the resultant polymer. However, there are few direct comparisons in the literature that discuss which sulfonation method yields

better performance. In this chapter, two polymer hosts will be investigated sPEEK, which sulfonates in heterogeneous media and sPSU, which sulfonates in homogeneous media. These polymer hosts will be combined with imidazolium trifluoromethanesulfonate to observe their proton conduction properties, both macroscopically, and at the molecular level, using ^{1}H solid-state NMR.

6.2 Solid-State NMR Theory

In solid-state NMR broad linewidths are observed due to the lack of fast molecular tumbling that occurs in solution-state NMR. This is due to strong dipole-dipole couplings as seen in **Equation 6.1** where, μ_o is the space permeability constant, γ is the gyromagnetic constant (fundamental to all nuclei), r is the distance between spins i and j, θ the angle dependence, I is the observed spin and S is the non-observed spin.

$$H_D = -\sum_{i>j}\left(\frac{\mu_o}{4\pi}\right)\left(\frac{\gamma_i\gamma_j\hbar}{r_{ij}^3}\right) * \frac{1}{2}(3\cos^2\theta - 1)\left[\hat{I}_z\hat{S}_z\right] \qquad \textbf{(6.1)}$$

To achieve narrow lineshapes magic angle spinning is employed by physically rotating the sample at 57.74 to average the spatially dependent portion in **Equation 6.1**. However, dipole-dipole coupling contains useful information to explain structure and mobility within a sample. By reintroducing the dipole-dipole coupling in a controlled manner these dipole-dipole couplings can be observed to infer structure and mobility on a localized scale. These couplings were reintroduced using a double quantum filter (DQF) experiment will be used called back-to-back (BaBA). This pulse sequence will filter signals that do not participate in dipole-dipole coupling due to either the lack of close neighbors or by possessing high mobility on the timescale of the experiment. In this

instance, the ^{1}H DQF method provides only a qualitative measure of local mobility. For this reason, we turned to ^{2}H static NMR to quantify the local motion.

To determine the hopping rate of the hydrogen-bonded proton, involved with proton conduction, ^{2}H static NMR is utilized. Deuterium is a spin 1 nucleus that possesses two spin state transitions from its quadrupolar nucleus. From these two spin transitions two horns are observed in a ^{2}H static NMR lineshape, where the horn splitting is on the order of 140-220 kHz, and is therefore sensitive to motion on this timescale, which corresponds to the molecular motion of organic solids.[23–25] Therefore, the lineshapes can change as a function of temperature if mobility on this timescale is occurring. These lineshapes can be fitted with a program called EXPRESS to extract hopping rates.[26] Another advantage of using ^{2}H NMR is that the proton conducting sites can be easily and selectively exchanged for deuterium, therefore only the site of interest is observable when using this technique.

6.3 Experimental

Polyetheretherketone (obtained from Victrex®) was sulfonated by dissolving 20 g of PEEK into 300 mL of H_2SO_4 at 60°C overnight to obtain a high degree of sulfonation (>90%) as seen in **Figure 6.1A**. The polymer was precipitated in water and rinsed with water until the pH was neutral. The polymer was dried in a vacuum oven at 60°C overnight then 120°C for one day. Acid treatment was performed on the polymer by soaking the polymer in a 1M H_2SO_4 solution; the polymer was then rinsed to pH neutral, and was dried at 80°C for one day.

A

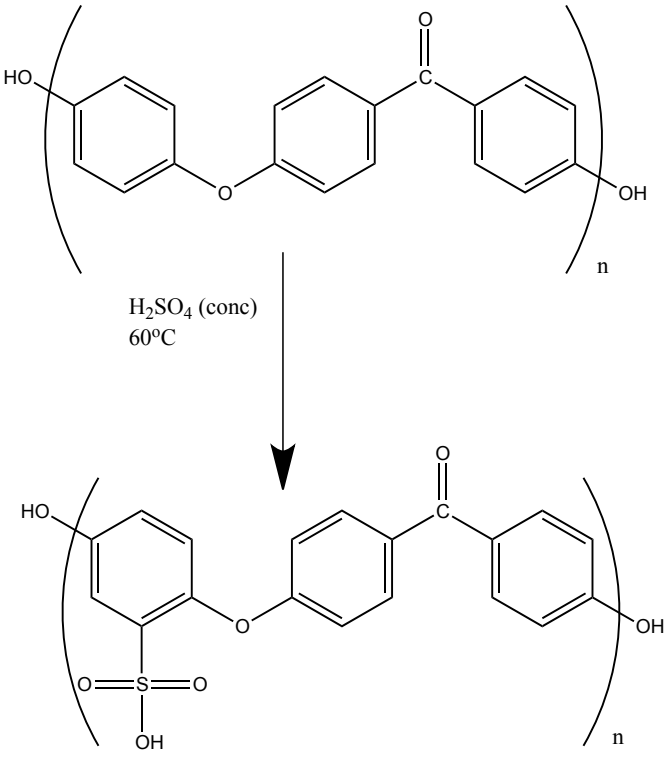

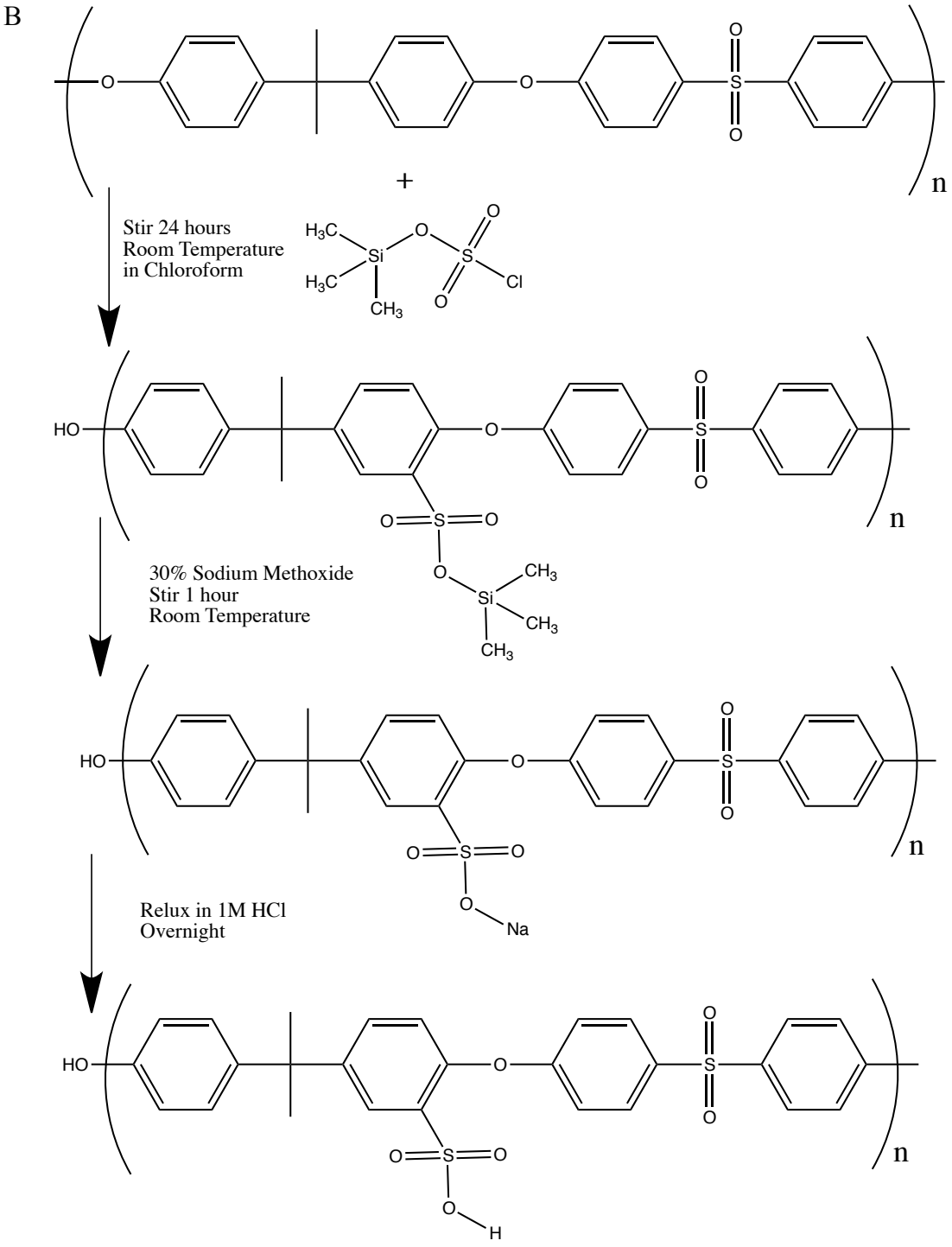

Figure 6.1: Sulfonation synthetic schemes of A) sPEEK[27] B) sPSU[28]

Polysulfone was purchased from Sigma-Aldrich dissolved in purified dried chloroform and then was sulfonated by adding trimethylsilylchlorosulfonate drop wise in a 1:2 molar ratio under nitrogen (**Figure 6.1B**). The mixture was stirred at room temperature for 24 hours. Then 2 mL of 30% sodium methoxide in methanol was added to the mixture and stirred for 1 hour. After an hour 1 mL of ethanol was added to the mixture to restabilize the chloroform. The mixture was exposed to air and the solvents were removed by rotovap. The resultant polymer was then washed 3 times in minimal amounts of ethanol and 3 times in minimal amounts of water. The polymer was dried for 24 hours at 110°C. After drying, the polymer was protonated via reflux in 1 M HCl and was then rinsed to pH neutral with water. The polymer was casted by making a 10% polymer solution in N, N dimethylacetamide and poured onto a Petri dish and dried under vacuum for 24 hours at 60°C then at 110°C for another 24 hours.

Imidazolium trifluoromethanesulfonate (IFMS) was purchased from Sigma-Aldrich. Composites of IFMS and sPEEK were prepared by first dissolving sPEEK in a 10% by weight with N, N dimethylacetamide. To obtain different loadings of IFMS in sPEEK, IFMS was dissolved into the sPEEK solution in varied weight ratios. IFMS-sPEEK solutions were stirred overnight then casted and dried for 24 hours at 60°C under vacuum. Composites of IFMS and sPSU were prepared by first dissolving sPSU in a 10% by weight into N, N dimethylacetamide. To obtain different loadings of IFMS in sPSU, IFMS was dissolved into the sPSU solution in varied weight ratios. The solutions were allowed to gel while being stirred at 60°C. Once the solution was viscous the gel was casted and dried first at 60°C under vacuum for 24 hours, then at 80°C for another 24 hours then finally at 110°C overnight.

The degree of sulfonation of the sulfonated polymers was confirmed with solution state NMR on a 200 MHz spectrometer for sPEEK and on a 600 MHz spectrometer for sPSU. The polymers were dissolved into DMSO with TMS as the internal standard. These measurements were conducted at room temperature using a 90° pulse. Here, the degree of sulfonation for the polymers will be shown with brackets, for example sPEEK(90) will depict a sPEEK host possessing a degree of sulfonation of 90%.

Thermogravimetric analysis (TGA) was performed on a NETZSCH STA 409 PC/PG instrument referenced with Al_2O_3 using a 10°C/minute temperature ramp from 35 to 800°C under air. This technique was used to determine salt loadings within the polymer matrix. The notation for the composites will be presented as IFMS(20)-sPEEK(90) denoting that there is a 20% loading of IFMS in sPEEK that has been 90% sulfonated.

Electrochemical impedance spectroscopy was performed on a Gamry Reference 600 potentiostat. Composite samples were analyzed using an in-plane conductivity cell. The samples were cut into 0.5x2 cm strips to be placed into the conductivity cell. The cell was placed in an oven with anhydrous conditions to equilibrate for one hour before proton conductivity measurements. Experiments were conducted at a DC voltage of 0.5 V with an amplitude of 50 mV and a frequency sweep from $1.0x10^5$ to 1 Hz.

^1H MAS NMR experiments were performed on a Bruker Avance 500 MHz spectrometer, equipped with an 11.7 T magnet. All samples were referenced to adamantane (1.85 ppm for ^1H).[29] Samples were packed into a 2.5 mm diameter rotor and magic angle spinning was conducted at 25 kHz. Solid-state ^1H NMR spectra were acquired with a 90° pulse length at 100 kHz of power. Delays were chosen to be five

times greater than the T_1 of the sample. T_1 measurements were obtained using a saturated recovery method.[30]

Double quantum experiments were obtained with the *back-to-back* sequence (BaBa).[31,32] Experiments were performed on a 2.5 mm rotor spinning at 25 kHz on a Bruker Avance 500 MHz spectrometer. BaBa experiments were rotor synchronized for 2τ (80 μs periods) with two loops of recoupling and all 90° pulses were with 100 kHz of power. Experiments were collected with 16 scans to complete the full phase cycle.

Deuteration of IFMS was performed by refluxing IFMS in CD_3OD, under inert atmosphere, the sample was stored in an argon glove box after being recrystallized three times. Deuteration of IFMS was confirmed with ^1H and ^2H 25 kHz MAS, where the deuteration was determined to be ~60%. Deuteration of sPEEK was performed using D_2SO_4 instead of H_2SO_4 as described above and was confirmed to be 100 % successful. The CD_3OD was purchased from Cambridge isotope laboratories and D_2SO_4 was purchased from Sigma Aldrich.

^2H NMR was performed on a wide bore 300 MHz Bruker HD magnet using a 5 mm static probe, where the sample is positioned in the horizontal solenoid coil. To measure ^2H lineshapes a solid echo pulse sequence is used to refocus the pulse to be observed after the pulse itself has fully elapsed. A solid echo (90-τ-90) since quadrupolar lineshapes are broad and the 90° pulse has a larger excitation window. The pulses were calibrated to achieve 22 kHz of power for the two 90° pulses in the sequence, where the delay between the pulses was 50 μs and after the last pulse before acquisition the delay was 15 μs. The free induction decay (FID) obtained was converted from digital to analog

and left shifted by 256 points and 5000 Hz of line broadening was applied. All deuterium NMR spectra were shift referenced to the methyl group in CD_3OD at 3.35 ppm.

Simulations of ^2H lineshapes were performed by a program called EXPRESS written by Vold et al.[26] These simulations were conducted with 1024 points in the FID, 256 powder averaging with the ^2H quadrupolar echo lineshape experiment. The experiment used only one frame since all the sites were fully occupied. All site angles for CSA were set to zero since deuterium does not possess any significant CSA effects. The site angles for EFG were calculated for IFMS from the crystallographic data by rotating each site into the same frame of reference using Euler angles. For sPEEK simulations the EFG angles used were from a stock experiment depicting a three-site rotation. The quadrupolar constants for all samples were calculated from the lineshape after motion was frozen (cold temperature NMR) and fitted using Wsolids to extract the constant value.[33] For all samples the asymmetry parameter was zero as determined by the fitting from Wsolids on the motional frozen samples. For sPEEK the site connectivity used was selected to be chain and for IFMS the connectivity matrix was determined based on the crystallographic data, assuming H-bonding pathways were based on the two-fold ring flip and three-site C_{3v} rotation for the imidazolium and sulfonate groups respectively.

6.4 Results and Discussion

The degree of sulfonation can be quantitatively determined by ^1H solution-state NMR for both polymer hosts. This is because the sulfonate functional group increases the deshielding effect for proton H_A in both polymers (**Figure 6.2**) causing H_A to move to a higher chemical shift than H_B and H_C for sPEEK and H_g and H_f for sPSU.[34,35] Proton H_A can be directly measured to determine the degree of sulfonation. The sulfonate group

proton cannot be observed due to its fast exchange with deuterium in solution. However, the measurement of proton H_A is a direct measure of how many repeat units are sulfonated. To determine the degree of sulfonation for the polymer hosts the ratio of sulfonated repeat units to the total number of units as seen in **Equation 6.2** for sPEEK and **Equation 6.3** for sPSU. **Figure 6.2A** depicts the solution-state NMR of sPEEK which was determined to be 90% DS with this technique and **Figure 6.2B** shows sPSU at 94%.

$$DS = \frac{Area_a}{\frac{\left[Area_{b,b',c,c',d,d',e,e'} + (2 * Area_a)\right]}{12}} * 100 \quad \textbf{(6.2)}$$

$$DS = \frac{16R}{1+2R}, R = \frac{A_a}{A} \quad \textbf{(6.3)}$$

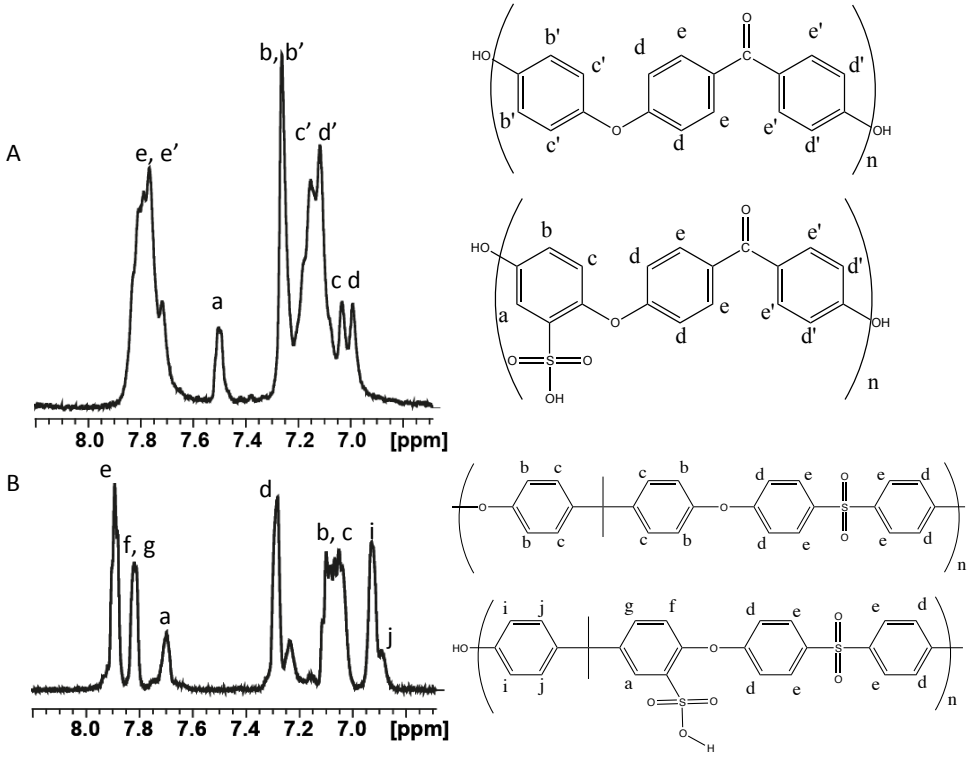

Figure 6.2: ^{1}H solution state NMR with assignments of A) sPEEK, 200 MHz B) sPSU, 600 MHz.

The polymer solution and conditions of casting can impact the morphology of the resultant polymer. For example, when Nafion is dissolved and recast the polymer can exhibit a four-fold decrease in performance.[36] Since PEEK cannot dissolve into solvents it is sulfonated in heterogeneous media with concentrated acid to act as both the solvent and the sulfonating agent.[37] PSU can dissolve into solvents such as chloroform and dichloromethane thus making a homogeneous solution and can be sulfonated with a sulfonating agent.[28] This chapter demonstrates how the sulfonating media affects the resultant polymers and thus its composites with organic solid acids, more specifically IFMS.

For IFMS-polymer composite samples, the loading of IFMS was determined by TGA under air. The weight loss between 300 and 500°C is the region where the sulfonate functional group is combusted. Both polymer hosts and IFMS have these functional groups, which makes the differentiation between polymer and solid acid quite challenging. Therefore, to determine the salt loading the fraction of sulfonate functional groups that correspond to the polymer must be subtracted from the total weight-loss occurring due to sulfonate oxidation to SO_2 that occurs between 300-500°C. This is achieved by calculating the weight loss of polymer based on its degree of sulfonation determined by NMR. The loadings of IFMS that were obtained in sPEEK were 50±5, 40±5, 30±5 and 15±5% as seen in **Figure 6.3A**. The loadings of IFMS in sPSU were 30±1, 40±1 and 50±1% as seen in **Figure 6.3B**. It is important to note that there is a systematically higher error with IFMS-sPEEK composites than IFMS-sPSU from reproducibility of sample loadings. The salt loading will be indicated throughout this

chapter in brackets after the salt, for example IFMS(30)-sPSU(90) would indicate 30% loading of IFMS in sPSU that possesses a degree of sulfonation of 90 %.

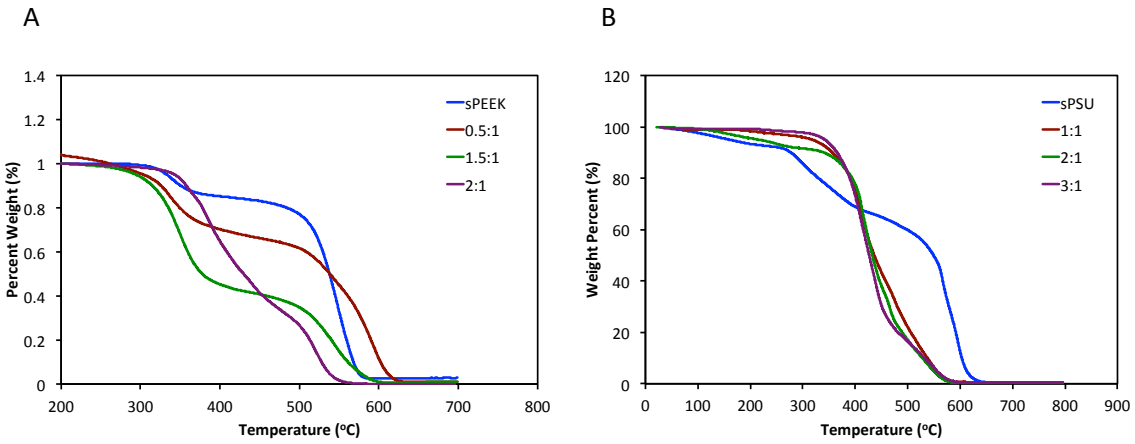

Figure 6.3: TGA under air, 10°C/min A) sPEEK and IFMS-sPEEK composites B) sPSU and sPSU composites.

EIS measurements were conducted to investigate how proton conductivity would be affected by salt loading. **Figure 6.4** depicts conductivity under anhydrous conditions at temperatures between 80-120°C for the IFMS, sPEEK(90) and IFMS-sPEEK composites. sPEEK itself exhibits a poor conductivity due to the lack of water present to support its vehicle mechanism of proton transport.[38] The IFMS(15)sPEEK90 had similar proton conductivity to the pure IFMS salt within error. This is attributed to the low loading level, which results in a non-uniform distribution of salt within the polymer, resulting in a similar conductivity to that of IFMS alone.[16] As more salt is loaded into the polymer the proton conductivity is observed to plateau. IFMS(40)-sPEEK(90) was compared to a IFMS-Teflon composite with similar loadings. All IFMS-sPSU composites (**Figure 6.5**) possessed higher conductivity than the salt itself, however all the composites possessed the same proton conductivity within error. Therefore, for comparison purposes IFMS(40)-sPSU(93) is chosen to match the loadings of the two

other composites. From these comparisons it can be observed that the proton conductivity is significantly improved when the polymer host possesses a sulfonate functional group, however the conductivity is similar between the two polymer hosts.

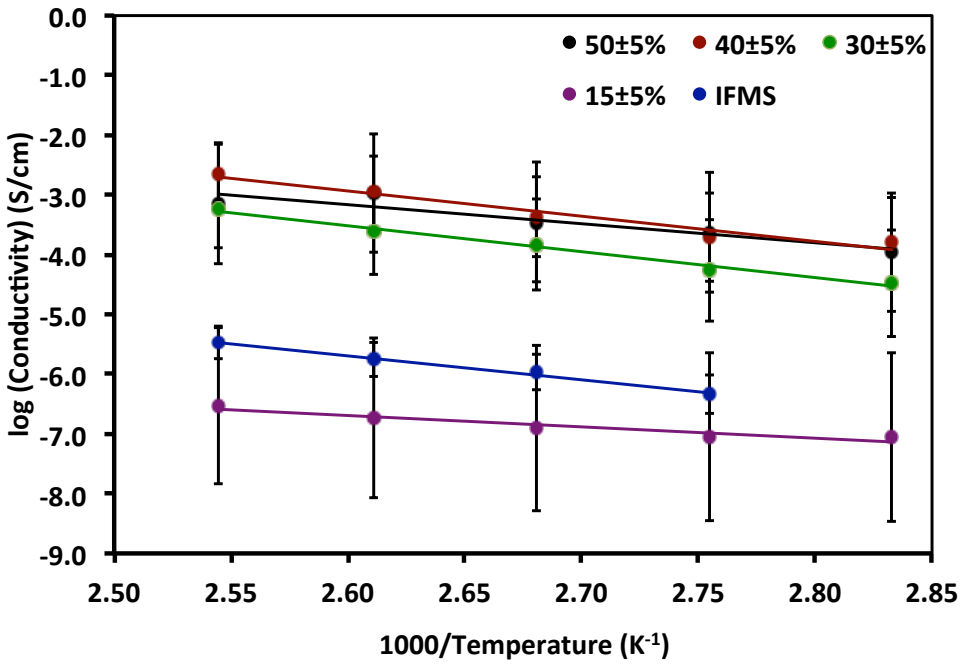

Figure 6.4: Proton conductivity of IFMS, IFMS-sPEEK composites, collected under anhydrous conditions.

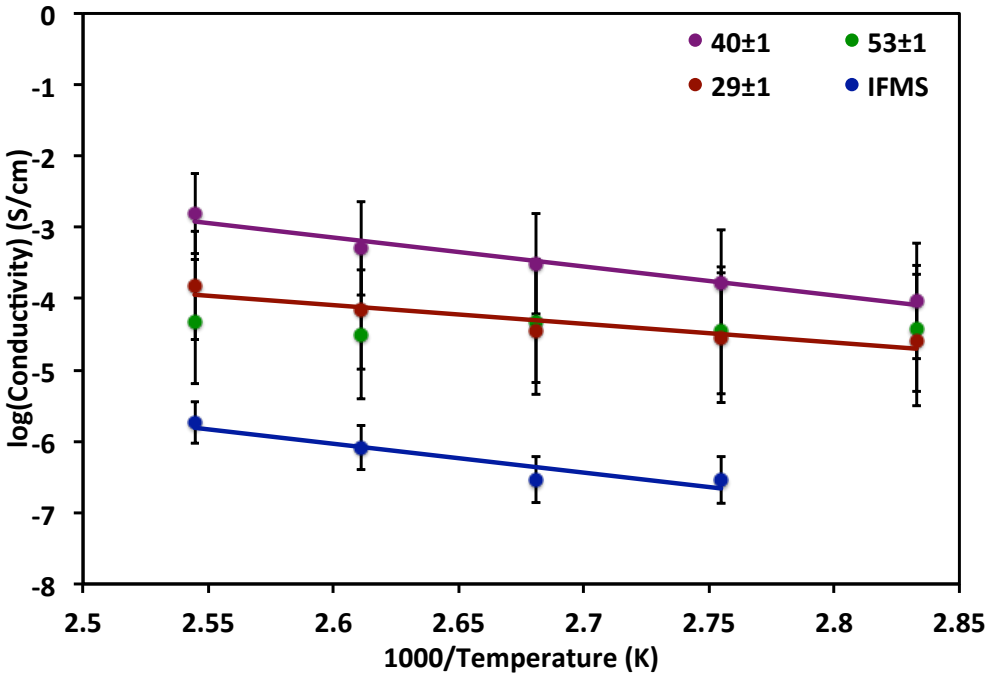

Figure 6.5: Proton Conductivity of IFMS and IFMS-sPSU composites under anhydrous conditions.

Figure 6.6 depicts EIS of various combinations of cation, anion and sPEEK (protonated and non-protonated) at 120°C under dry conditions. The proton conductivity for sPEEK is poor due to the lack of water within the polymer to conduct protons. With the non-protonated polymer, with 40% IFMS, the proton conductivity increases slightly. The salt itself possesses higher proton conductivity than the IFMS(40)Na-sPEEK(90) composite. Proton conductivity is dramatically increased when composites are formed from protonated, sulfonated functionalized polymers. With just the heterocyclic (neutral imidazole) loaded into the protonated polymer, the conductivity is significantly higher than the salt itself (100 times). With the anion of the salt included, IFMS(40)-sPEEK(90), the proton conductivity is slightly higher (the highest for this host), with a value of $5.3\pm3.6\times10^{-4}$ S/cm, where the high error takes into account reproducibility in sample preparation. This implies that both the proton on the polymer and the salt (both cation

and anion) assist in providing the high proton conductivity in anhydrous high temperature conditions. The highest proton conductivity was by IFMS(40)-sPSU(93) which was $1.5\pm1.0\text{x}10^{-3}$ S/cm, which is 10 times greater than IFMS(40)-sPEEK(90) showing that homogeneous sulfonation increases proton conductivity.

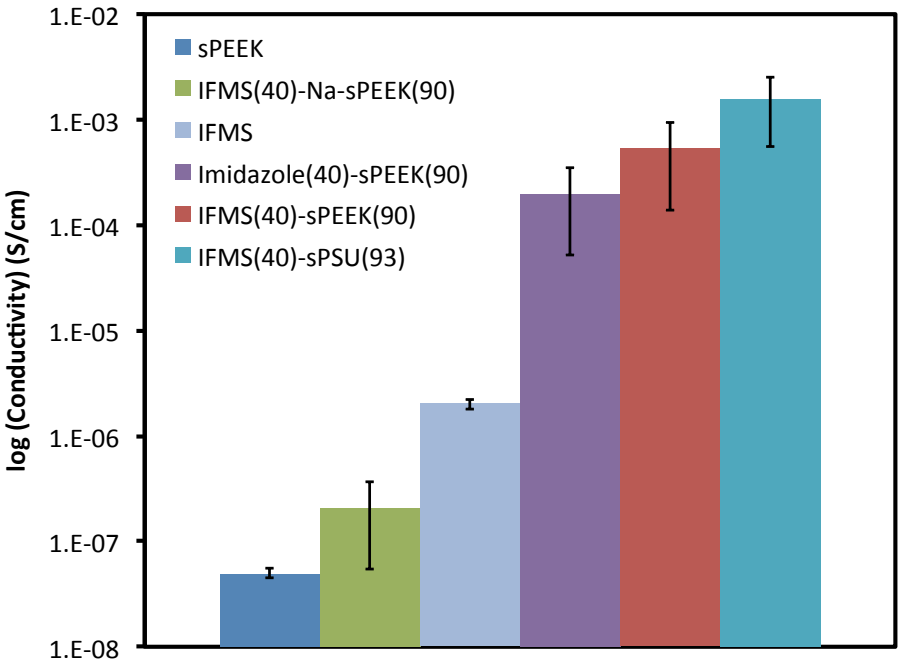

Figure 6.6: Logarithmic scale of proton conductivity at 120°C, anhydrously of sPEEK, IFMS-Na-sPEEK, IFMS, Imidazole(40)-sPEEK(90), IFMS(40)-sPEEK(90) and IFMS(40)-sPSU(93).

6.4.1 ^{1}H Solid-State NMR

For ^{1}H NMR there are three areas of interest: aliphatic (0-5 ppm), aromatic (5-9 ppm) and hydrogen bonded regions (9-16 ppm). All of the ^{1}H MAS spectra were collected at 25 kHz and did not possess any significant spinning sideband intensities.

^{1}H MAS NMR sPEEK: The ^{1}H NMR spectrum for sPEEK has two resonances including the hydrogen-bonded peak at 8.7 ppm (A) and the aromatic peak, representing the backbone of the polymer at 6.7 ppm (B) as seen in **Figure 6.7A**. The resonances observed are broad, indicating strong dipole-dipole coupling that arises from the H-

bonded network. The ^{1}H DQF NMR spectrum shows that the hydrogen-bonded site (A) was completely removed from the spectrum which signifies that the proton is either highly mobile or does not possess any near neighbors (>3.5 Å apart). Ye *et al.* obtained a similar result where they determined that the hydrogen-bonded peak was removed from the spectrum of dehydrated sPEEK due to the large distance between the sulfonic acid sites.[27] This occurs when the polymer is dried and results in the backbone becoming further apart with the sulfonate groups being highly spaced.

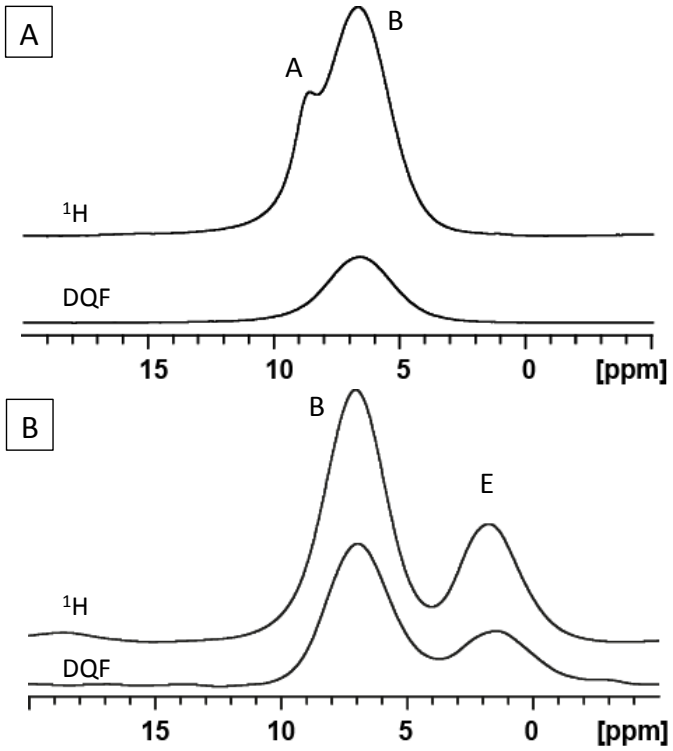

Figure 6.7: ^{1}H 25 kHz MAS NMR and DQF on 2.5 probe, 500 MHz spectrometer of A) sPEEK B) sPSU, where A is the hydrogen-bonded site, B are aromatic sites and E is the methyl group.

^{1}H MAS NMR sPSU: For this polymer host there are two main resonances including the aromatic region at 7.0 ppm and aliphatic region at 2.0 ppm as seen in **Figure 6.7B**. The hydrogen-bonded peak is predicted to be under the broad resonance of the aromatic sites

since the chemical shift environment is similar to sPEEK. The broad resonances indicate strong dipole-dipole coupling within the structure. The DQF spectrum shows high attenuation in the aromatic region (possible removal of the hydrogen-bonded site). As well, the aliphatic site is highly attenuated, which arises from the methyl group being able to rotate freely in the solid, and thereby averaging its homonuclear dipolar coupling.

^{1}H MAS NMR IFMS: The solid acid of interest, IFMS, has three resonances the hydrogen-bonded region at 11.4 ppm and the two aromatic resonances at 8.1 (B) and 7.1 ppm (B') (**Figure 6.8**). The sites are significantly narrower than sPEEK due to the lack of extensive homonuclear ^{1}H-^{1}H dipole-dipole coupling in this fluorinated structure. The ^{1}H DQF NMR depicts all the resonances attenuating by similar degrees suggesting high mobility in all proton sites. This was observed in a previous study performed by De Almeida *et al*.[17]

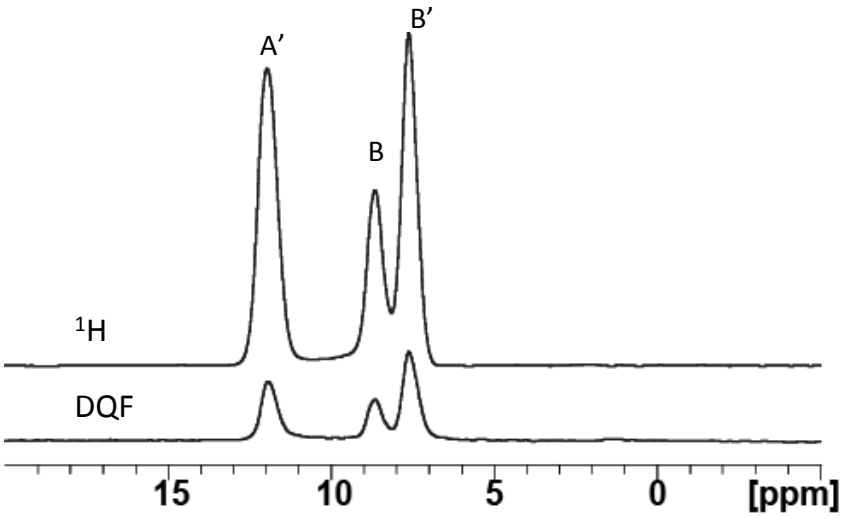

Figure 6.8: ^{1}H 25 kHz MAS NMR and DQF on 2.5 probe, 500 MHz spectrometer of IFMS, where A' is the hydrogen bonded site and B and B' are aromatic sites.

^{1}H MAS NMR of IFMS-sPEEK: After synthesizing the IFMS(40±5%)-sPEEK(90) composite the ^{1}H NMR includes seven resonances, as shown in **Figure 6.9A**. The

hydrogen-bonded sites from sPEEK (A) and IFMS (A') sites are overlapped at 12.2 and 12.0 ppm respectively. The aromatic sites of the composite are at 8.6 ppm (B), 7.5 ppm (C) and 6.7 ppm (D). The site at 4.6 ppm (W) is believed to be residual water and a small aliphatic site at 2.4 ppm (S), corresponding to a small amount of residual solvent that could not be removed. In the ^{1}H NMR of the composite it can be observed that the addition of IFMS has significantly narrowed the polymer peaks. This is due to the to enhanced local dynamics, consistent with a less rigid structure within the polymer. In the ^{1}H DQF spectrum sites, W and S are removed due to their high mobility as seen in previous literature. Aromatic sites B, C and D have attenuated slightly most likely due to mobility because each of the sites has close covalently bound neighbors. Hydrogen-bonded sites A and A' have attenuated more than the aromatic sites, which indicates a high degree of local proton mobility, as measured by the EIS data shown above.

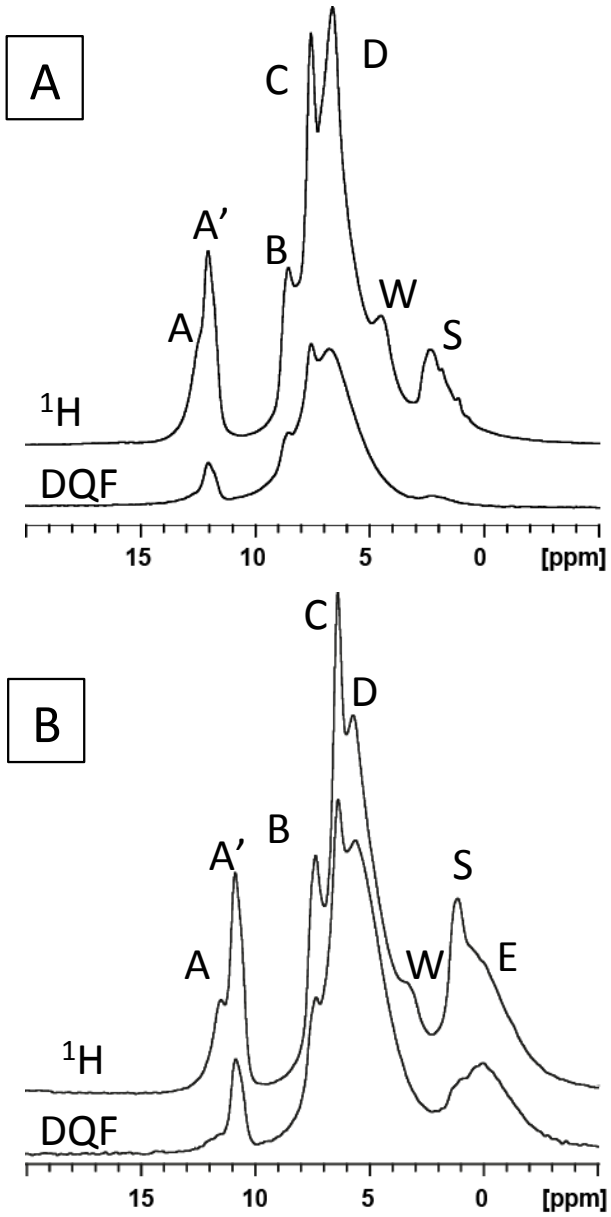

Figure 6.9: ^{1}H 25 kHz MAS NMR and DQF on 2.5 probe, 500 MHz spectrometer of A) IFMS(40)-sPEEK(90) B) IFMS(40)-sPSU(93), where A is the hydrogen-bonded site from the polymer, A' is the hydrogen-bonded site from IFMS, B-D are aromatic sites, E is the aliphatic site (sPSU backbone), W is trace amounts of water and S is the solvent.

^{1}H MAS NMR IFMS-sPSU: With the insertion of IFMS into sPSU there are eight resonances observed in the ^{1}H MAS NMR as seen in **Figure 6.9B**. In the hydrogen-bonded region there are two sites A being from sPSU, which can now be observed, and A' from IFMS. The aromatic region (2.3 to 9.4 ppm) possesses three distant sites (B, C and

D) which are from both the polymer host and the salt. As seen with IFMS(40)-sPEEK(90) this region narrows significantly with the addition of the salt. The aliphatic region shows three sites, where the narrow resonances are due to trapped water (W) and solvent (S) (as seen via TGA to be ~5%) and the broad resonance (E) is due to the methyl functional groups in the backbone of the polymer. In the ^{1}H DQF NMR the hydrogen-bonded region, site A, is almost completely removed from the spectrum and A' is significantly attenuated showing that there are higher dynamics in the composite than sPSU and IFMS by themselves as observed previously with sPEEK composites.

6.4.2 ^{2}H Static NMR

The hydrogen-bonded sites were exchanged for deuterium to study their dynamics with ^{2}H static NMR. Only sPEEK and IFMS-sPEEK were used for this study because ^{1}H MAS spectra have shown that both polymers and salt-polymer composites behave similarly and would produce very similar spectra. Before studying the deuterated composite, sPEEK and IFMS were investigated separately. The ^{2}H static NMR variable temperature (VT) of dried sPEEK is shown in **Figure 6.10A**, where it can be seen that the lineshape does not change as a function of temperature. This lineshape was fitted by EXPRESS (based on a three site rotation) to be in the range of 0 to $1x10^{4}$ Hz (**Figure 6.10B**), this is reported as a range since the features that would indicate a change of hopping rate occur in the center with the horns. However, due to the isotropic site present in the sample, these features cannot be observed and only the horns can be fit and thus the hopping rate must be shown as a range. The features that would be observed are shown in chapter 2.

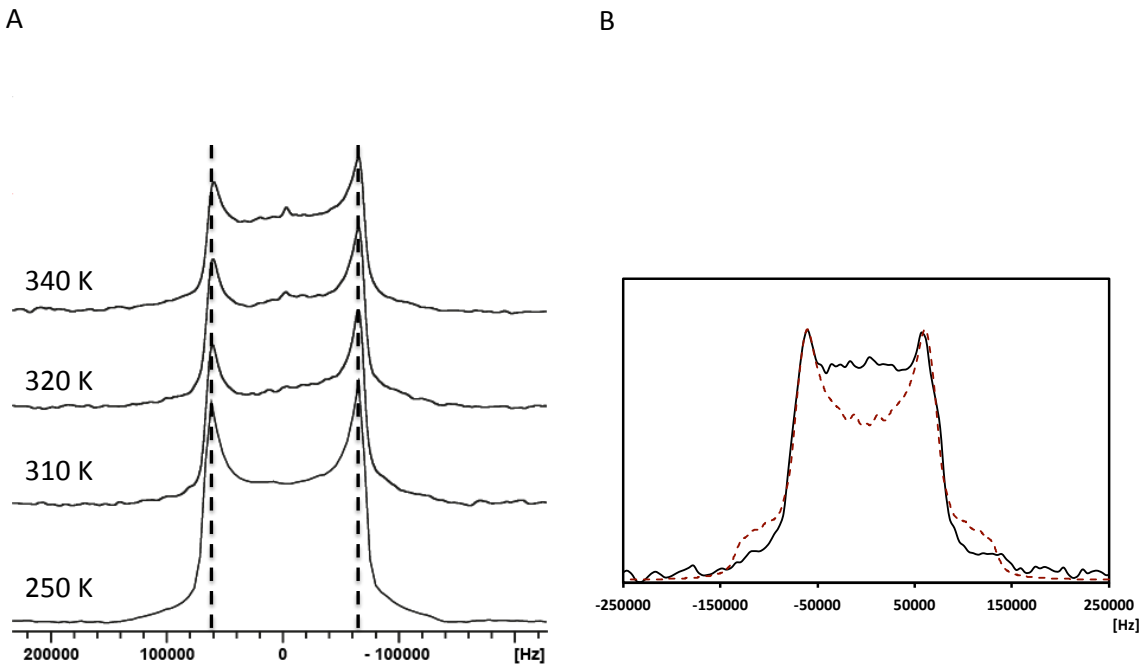

Figure 6.10: ^{2}H Static NMR of sPEEK, 300 MHz, 5mm probe A) Variable temperature stack plot, where the lineshape did not change B) Fit of sPEEK to 0-1x10^{4}Hz. The distance of the horns maintain a constant splitting of 126 kHz.

The ^{2}H static VT NMR for IFMS is shown in **Figure 6.11** (black lines), where the lineshapes have changed drastically as a function of temperature. For the simulations of IFMS the Euler angles must be known for all 16 sites to be in the same frame of reference for the calculations. The Euler angles were calculated for each of the 16 sites where the proton could be present in the structure and is tabulated in **Table 6.1**. It was assumed that the quadrupolar constant (C_q) and the asymmetry parameter did not change as a function of temperature and were kept constant with all the calculations. The quadrupolar constant was determined to be 160 kHz from the 250 K spectrum fitted with Wsolids.[33] The connectivity matrix was performed by measuring distances between cations and anions in the unit cell to propose a path, where proton hopping could be conducted. From the distances measured it is proposed that the proton is passed by an imidazole ring, through a ring flip, to the anion (trifluoromethanesulfonate), undergoing a three-site rotation, to

another imidazole ring in an up and down motion throughout the unit cell. **Figure 6.12** shows a connectivity matrix of how the hydrogen-bonded sites will exchange throughout the structure, where blue indicates exchange due to a ring flip from the cation and red indicates exchange via a three-site rotation from the anion. The fits are shown in **Figure 6.11** (red lines), where, with this model, the rates for cation and anion motion had to be set equal to each other in order for the simulated spectrum to match the experimental. This provided significant new insight into both the rate and the cooperative mechanism of ion transport, which could indeed lead to long-range conductivity. The hopping rates determined for IFMS can be found in **Table 6.2**, which is comparable to motion that has been observed with other polymers such as a polystyrene backbone.[23]

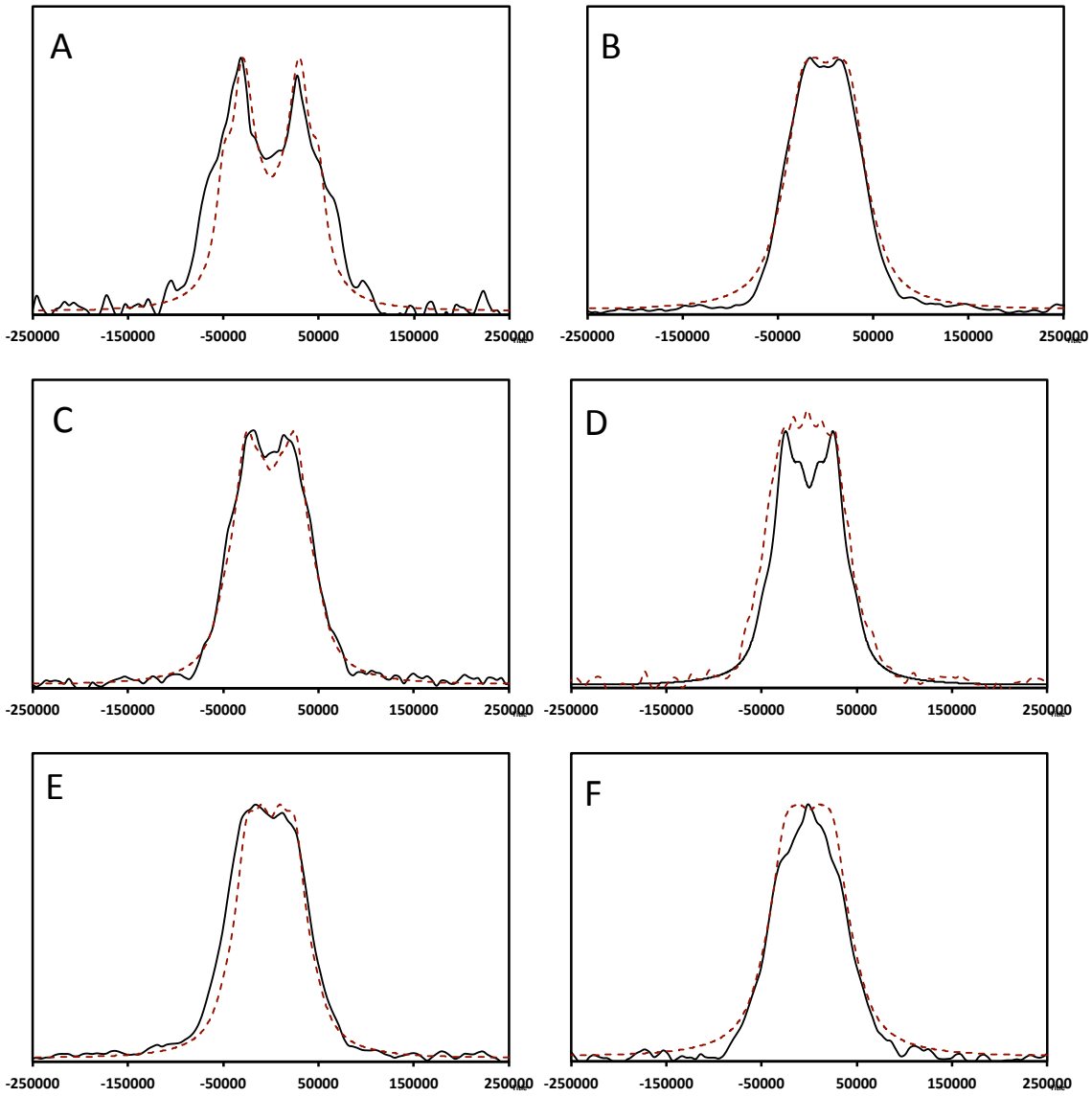

Figure 6.11: ^{2}H static NMR of IFMS collected on 300 MHz, 5 mm probe. Black is experimental and red is the simulated spectrum from EXPRESS A) 300 K fitted to $4x10^{4}$ Hz B) 310 K fitted to $5x10^{5}$ Hz C) 330 K fitted to $8x10^{5}$ Hz D) 340 K fitted to $8.2x10^{5}$ Hz E) 350 K fitted to $9.5x10^{5}$ Hz F) 360 K fitted to $1.0x10^{6}$ Hz.

Table 6.1: Euler Angles of the 16 sites in IFMS.

Site	Beta	Gamma
1	-38.224	123.527
2	-38.2884	-56.4734
3	-38.2884	33.5266
4	-38.2884	-146.473
5	-141.712	56.4733
6	-141.712	-123.527
7	-141.711	146.473
8	-141.712	-33.5266
9	-112.155	-82.7525
10	-122.155	97.2475
11	-112.155	-172.752
12	-112.155	7.24755
13	-67.8451	-97.2475
14	-67.8452	82.7524
15	-67.8451	-7.24747
16	-67.8452	172.752

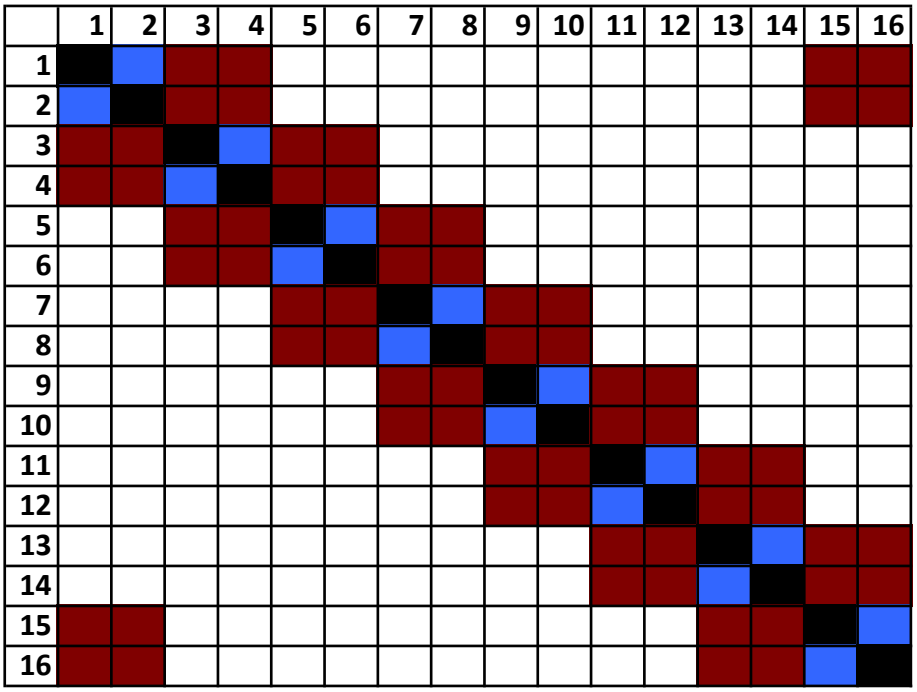

Figure 6.12: Connectivity Matrix of IFMS. Blue is a connection with a ring flip (Imidazolium) and red is a connection with a three-site rotation (trifluoromethanesulfonate).

Table 6.2: Hopping rates determined by EXPRESS to fit ^{2}H static lineshapes collected at various temperatures on a 300 MHz spectrometer with a solid echo.

Temperature (K)	Hopping Rate (Hz)
300	$4.0\pm0.1\text{x}10^4$
310	$5.0\pm0.1\text{x}10^5$
330	$8.0\pm0.1\text{x}10^5$
340	$8.2\pm0.1\text{x}10^5$
350	$9.5\pm0.1\text{x}10^5$
360	$1.0\pm0.1\text{x}10^6$

A deuterated IFMS(40)-sPEEK(90) was synthesized and its ^{2}H static NMR is presented in **Figure 6.13**. At cold temperatures (250 K) a similar powder pattern similar to that of sPEEK and IFMS when no effects of motion were observed in the ^{2}H lineshape, indicating that motion is slower than $1\text{x}10^4$ Hz was observed. As the temperature was increased an isotropic peak gains intensity as the horns powder pattern decrease in intensity. The splitting of the horns is the same as sPEEK (splitting is 126 kHz), where they are significantly further apart than in IFMS itself (splitting is 117 kHz). This indicates that what we are observing is the polymer host possessing motion between 0-$1\text{x}10^4$ Hz, as described above, and an inserted salt that is in the fast motion regime (>160 kHz, hopping rate). However, as the temperature increases the polymer is also averaging into the isotropic site, indicating that the polymer assists in the proton hopping mechanism at higher temperatures as seen with EIS measurements in **Figure 6.4**.

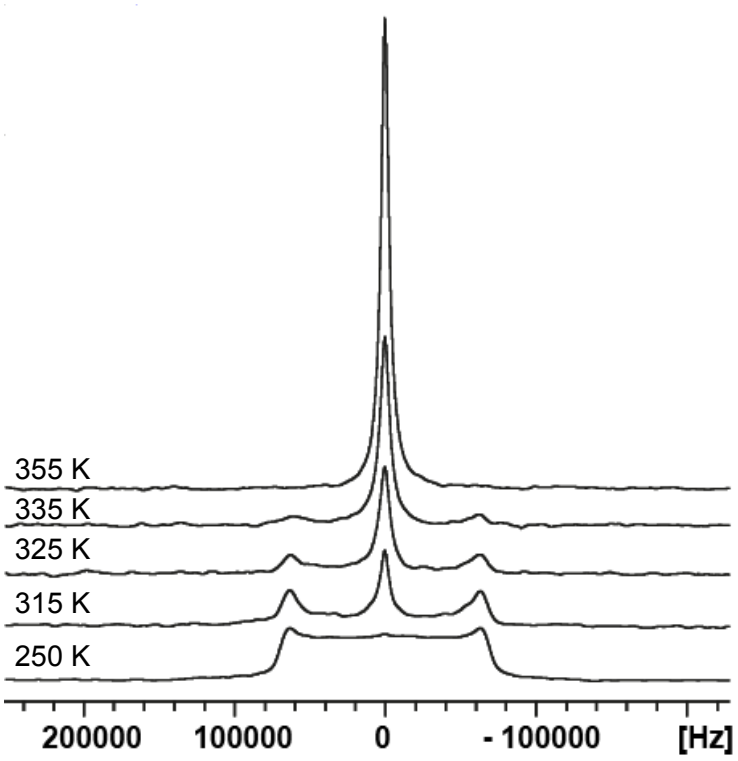

Figure 6.13: ^{2}H static 300 MHz NMR of IFMS(40±5%)-sPEEK(90) collected on 300 MHz, 5 mm probe, 1024 scans.

6.5 Conclusion

^{1}H MAS NMR revealed that additional local mobility was obtained after the addition of IFMS into either sPEEK or sPSU. This is consistent with EIS measurements collected at 120°C in anhydrous conditions that show high proton conductivity of $1.5\pm1.0\text{x}10^{-3}$ S/cm with 40±1% IFMS compared to just the polymer hosts, where the proton conductivity was $5.0\pm0.1\text{x}10^{-8}$ S/cm. EIS demonstrates that both the anion and the cation of the salt are involved in proton conduction within the composite as well as the sulfonate group on the backbone of the polymer. This was confirmed with ^{2}H static NMR, where IFMS was fitted well to a model that consisted of motion from the cation to the anion at the same rate. ^{2}H NMR also showed that the polymer assists with proton conductivity

from all deuterium sites being averaged into a single isotropic site achieving local hopping rates of greater than 160 kHz.

6.6 References

1. Carrette, L., Friedrich, K. A. & Stimming, U. Fuel Cells - Fundamentals and Applications. *Fuel Cells* **1,** 5–39 (2001).
2. Cheng, X. *et al.* A review of PEM hydrogen fuel cell contamination: Impacts, mechanisms, and mitigation. *J. Power Sources* **165,** 739–756 (2007).
3. Ghassemzadeh, L. *et al.* Chemical degradation of proton conducting perflurosulfonic acid ionomer membranes studied by solid-state nuclear magnetic resonance spectroscopy. *J. Power Sources* **186,** 334–338 (2009).
4. Kabasawa, A., Saito, J., Miyatake, K., Uchida, H. & Watanabe, M. Effects of the decomposition products of sulfonated polyimide and Nafion membranes on the degradation and recovery of electrode performance in PEFCs. *Electrochimica Acta* **54,** 2754–2760 (2009).
5. Mauritz, K. A. & Moore, R. B. State of understanding of Nafion. *Chem. Rev.* **104,** 4535–4585 (2004).
6. Peng, Z., Morin, A., Huguet, P., Schott, P. & Pauchet, J. In-Situ Measurement of Electroosmotic Drag Coefficient in Nafion Membrane for the PEMFC. *J. Phys. Chem. B* **115,** 12835–12844 (2011).
7. Dippel, T. & Kreuer, K. D. Proton transport mechanism in concentrated aqueous solutions and solid hydrates of acids. *Solid State Ion.* **46,** 3–9 (1991).
8. Noda, A. *et al.* Bronsted acid-base ionic liquids as proton-conducting nonaqueous electrolytes. *J. Phys. Chem. B* **107,** 4024–4033 (2003).

9. Watanabe, M., Tsurumi, K., Mizukami, T., Nakamura, T. & Stonehart, P. ACTIVITY AND STABILITY OF ORDERED AND DISORDERED CO-PT ALLOYS FOR PHOSPHORIC-ACID FUEL-CELLS. *J. Electrochem. Soc.* **141,** 2659–2668 (1994).

10. Haile, S. M., Boysen, D. A., Chisholm, C. R. I. & Merle, R. B. Solid acids as fuel cell electrolytes. *Nature* **410,** 910–913 (2001).

11. Haile, S. M., Chisholm, C. R. I., Sasaki, K., Boysen, D. A. & Uda, T. Solid acid proton conductors: from laboratory curiosities to fuel cell electrolytes. *Faraday Discuss.* **134,** 17 (2007).

12. Weber, J. Proton Conductivity Enhancement by Nanostructural Control of Poly(benzimidazole)-Phosphoric Acid Adducts. *Adv. Mater.* **20,** 2595–2598

13. Goward, G. Reorientation phenomena in imidazolium methyl sulfonate as probed by advanced solid-state NMR. *Solid State Nucl. Magn. Reson.* **24,** 150–162 (2003).

14. Połtarzewski, Z. Novel proton conducting composite electrolytes for application in methanol fuel cells. *Solid State Ion.* **119,** 301–304

15. Park, Y.-I. High proton conductivity in ZrP-PTFE composites. *J. Mater. Sci. Lett.* **19,** 1735–1738

16. Yan, Z. B., De Almeida, N. E., Traer, J. W. & Goward, G. R. Dynamics of benzimidazole ethylphosphonate: a solid-state NMR study of anhydrous composite proton-conducting electrolytes. *Phys. Chem. Chem. Phys.* **15,** 17983–17992 (2013).

17. De Almeida, N. E. & Goward, G. R. Proton Dynamics in Sulfonated Ionic Salt Composites: Alternative Membrane Materials for Proton Exchange Membrane Fuel Cells. *J. Power Sources* **268,** 853–860 (2014).

18. Xing, P. *et al.* Synthesis and characterization of sulfonated poly(ether ether ketone) for proton exchange membranes. *J. Membr. Sci.* **229,** 95–106 (2004).

19. Manea, C. & Mulder, M. Characterization of polymer blends of polyethersulfone/sulfonated polysulfone and polyethersulfone/sulfonated polyetheretherketone for direct methanol fuel cell applications. *J. Membr. Sci.* **206,** 443–453 (2002).

20. Rozière, J. & Jones, D. J. Non-Fluorinated Polymer Materials for Proton Exchange Membrane Fuel Cells. *Annu. Rev. Mater. Res.* **33,** 503–555 (2003).

21. Boysen, D. A., Chisholm, C. R. I., Haile, S. M. & Narayanan, S. R. Polymer Solid Acid Composite Membranes for Fuel-Cell Applications. *J. Electrochem. Soc.* **147,** 3610–3613 (2000).

22. Jones, D. J. & Roziere, J. Recent advances in the functionalisation of polybenzimidazole and polyetherketone for fuel cell applications. *J. Membr. Sci.* **185,** 41–58 (2001).

23. Jelinski, L. W. Solid State Deuterium NMR Studies of Polymer Chain Dynamics. *Annu. Rev. Mater. Sci.* **15,** 359–377 (1985).

24. Spiess, H. W. Molecular dynamics of solid polymers as revealed by deuteron NMR. *Colloid Polym. Sci.* **261,** 193–209 (1983).

25. Duer, M. J. *Solid State NMR Spectroscopy: Principles and Applications*. (Wiley, 2001).

26. Vold, R. L. & Hoatson, G. L. Effects of jump dynamics on solid state nuclear magnetic resonance line shapes and spin relaxation times. *J. Magn. Reson.* **198,** 57–72 (2009).

27. Ye, G., Janzen, N. & Goward, G. R. Solid-state NMR study of two classic proton conducting polymers: Nafion and sulfonated poly(ether ether ketone)s. *Macromolecules* **39,** 3283–3290 (2006).

28. Lufrano, F., Squadrito, G., Patti, A. & Passalacqua, E. Sulfonated polysulfone as promising membranes for polymer electrolyte fuel cells. *J. Appl. Polym. Sci.* **77,** 1250–1256 (2000).

29. HA, S. & Hayamizu, K. Chemical shift standards in high-resolution solid-state NMR (1) 13C, 29Si, and 1H nuclei. *NOTES* **64,** 685–687 (1991).

30. Hahn, E. L. Spin Echoes. *Phys. Rev.* **80,** 580–594 (1950).

31. Brown, S. P., Schnell, I., Brand, J. D., Müllen, K. & Spiess, H. W. A 1H double-quantum magic-angle spinning solid-state NMR investigation of packing and dynamics in triphenylene and hexabenzocoronene derivatives. *J. Mol. Struct.* **521,** 179–195 (2000).

32. Brown, S. P. & Spiess, H. W. Advanced solid-state NMR methods for the elucidation of structure and dynamics of molecular, macromolecular, and supramolecular systems. *Chem. Rev.* **101,** 4125–4155 (2001).

33. Eichele, K. *Wsolids1*. (Universitat Tubingen, 2013).

34. Guhathakurta, S. & Min, K. Lithium sulfonate promoted compatibilization in single ion conducting solid polymer electrolytes based on lithium salt of sulfonated polysulfone and polyether epoxy. *Polymer* **51,** 211–221 (2010).

35. Robertson, G. P. *et al.* Casting solvent interactions with sulfonated poly(ether ether ketone) during proton exchange membrane fabrication. *J. Membr. Sci.* **219,** 113–121 (2003).

36. Zaluski, C. & Xu, G. Blends of Nafion and Dow Perfluorosulfonated Ionomer Membranes. *Macromolecules* **27,** 6750–6754 (1994).

37. Li, Q., He, R., Jensen, J. O. & Bjerrum, N. J. Approaches and Recent Development of Polymer Electrolyte Membranes for Fuel Cells Operating above 100 °C. *Chem. Mater.* **15,** 4896–4915 (2003).

38. Kreuer, K. D. On the development of proton conducting polymer membranes for hydrogen and methanol fuel cells. *J. Membr. Sci.* **185,** 29–39

Chapter 7: Summary and Outlook

7.1 Summary

Current operating temperatures and high humidity result in poisoning of the catalyst and significant water management issues within the fuel cell. This thesis has investigated several novel materials to target improved properties for PEM materials. To characterize these materials solid-state NMR was employed to understand mobility on a localized scale to explain macroscale performance as assessed through electrochemical impedance spectroscopy.

In chapter 3 Nafion nanothin films were considered since thinner films could uptake additional water to improve water management and increase fuel cell temperatures. Although the polymer was able to take up additional water the conductivity decreased. Signal was obtained using solid-state NMR on Nafion thin and nanothin films, where this technique was never used before on such minute quantities. It was revealed that the protons within both the thin and nanothin films were in fast exchange regime with water at all humidities studied. However, it was the thin film that exhibited thermally activated dynamics as observed through the chemical shift trend to lower frequency at all humidities, where the nanothin polymer only exhibited this behaviour at high humidity. Therefore, it was concluded that the pores of the nanothin film contained the sulfonate group and water in fast exchange but due to long-range transport the protons across the film had a high activation energy barrier.

In chapter 4 solid-state NMR was used to investigate organic solid-acids to characterize their hydrogen-bonded network through double quantum filter experiments. This was performed on samples, where their proton conductivity was performed with

pellets. This type of EIS can possess higher resistances due to the formation of pellet and grain boundaries issues. This has lead to numerous disputes in the literature about how well a certain material can perform. In this chapter there were three solid-acids that showed that they possessed similar proton conductivities and solid-state NMR was conducted to observe if there was mobility differences with these materials that could be hidden with a proton conductivity macroscale technique. 2D ^{1}H DQF NMR using POST C7-DUMBO pulse sequence DQC buildup curves were obtained for each spin pair that exhibited a dipole-dipole coupling. IMSA and BMSA showed similar hydrogen-bonded environments, however with IFMS the DQC buildup curve was significantly shallower than IMSA and BMSA. Also, with the simulations IFMS was predicted to possess stronger dipole-dipole couplings than what was observed with the experiment DQC buildup curves. This indicates that there is additional mobility that can be utilized if the salt can be prepared in way to access its potential. This information otherwise would not be known if we could not probe these organic solid-acids on a localized scale.

For the solid-acids to be suitable for fuel cell application the solid-acids must be inserted into a host. In chapter 5 BMSA, IMSA and IFMS were inserted into a Teflon host. It was shown with T_1 relaxation studies, variable temperature ^{1}H MAS and ^{1}H DQF NMR that the dynamics were increased when the salt was inserted into the host as compared to the salts themselves. However, the overall proton conductivity only increased with IFMS-Teflon due to the limited solubility of the other salts, which prevented effective insertion into Teflon. The promising feature of study was that a polymer host does increase the mobility of the salts even if not enough salt could be inserted into the host, which could only be understood from solid-state measurements.

In chapter 6 IFMS was inserted into sulfonated functionalized hydrocarbon hosts to observe if the ionically conductive polymer could assist in proton conductivity. Two polymers were chosen to study heterogeneously- and homogeneously-sulfonated polymers. The preparation was optimized for the amount of IFMS that would provide the best proton conductivity. The two optimized polymer composites were IFMS(40)-sPEEK(90) and IFMS(40)-sPSU(93), where the proton conductivity was $5.3\pm3.6\text{x}10^{-4}$ and $1.5\pm1.0\text{x}10^{-3}$ S/cm respectively. This is significantly higher than IFMS itself and IFMS-Teflon. The highest proton conductivity obtained was using a homogeneous sulfonated functionalized host. Solid-state NMR was used to observe how IFMS and the sulfonated functionalized host are interacting to achieve this high proton conductivity. This was conducted with ^{1}H MAS, ^{1}H DQF and ^{2}H static NMR. It was shown that dynamics was increased after the salt was inserted into the polymer host from the linewidths decreasing in the ^{1}H MAS NMR and with the ^{1}H DQF showing less dipole-dipole coupling by exhibiting a lower intensity. ^{2}H static NMR was used to determine hopping rates from fitting lineshape changes to determine IFMS and the polymer interacted with each other. ^{2}H lineshape of dried sPEEK did not change as a function of temperature indicating limited dynamics. The hopping rate was determined, which increased with temperatures for IFMS. IFMS(40)-sPEEK(90) showed that the polymer increased IFMS into the fast motion limit, where proton hopping is faster than 160 kHz. The polymer host assists in proton conductivity as the proton as the horns decrease in intensity as the temperature increases, eventually averaging into the fast motion limit peak.

7.2 Outlook

Recently, there has been research in synthesizing an amorphous version of PEEK that would be able to dissolve into solvents like PSU. This would provide a direct comparison between heterogeneous and homogeneous sulfonation with the same polymer backbone. With this we could conclude whether controlling the sulfonation would be required in creating an ideal composite to obtain higher proton conductivity. Another polymer system worth investigating would be making composites with sulfonated hexafluoropolysulfone, where the methyl groups have been replaced with a trifluoromethyl groups. The C-F bond possesses higher stability than the C-H bond and would allow the polymer and resultant composites to be stable for longer at higher temperatures.

Numerous proton exchange membranes utilize acid doping to increase proton conductivity. However, how acid doping assists in proton conductivity mechanistically relatively unknown. Probing this relationship with solid-state NMR could reveal the mechanism of how acid doping aids in proton conduction. ^{2}H static NMR could initially be used to observe how the acid is contributing to the polymer, where this technique would portray if the acid were in a fast motion regime or a slower motion regime and how the polymer is being influenced by the presence of the acid.

Another approach to synthesizing better composites would be to monitor their solutions prior to casting since the casting solution has a great impact on the resulting polymer. Using pulse field gradient NMR the diffusion of the acidic protons can be monitored in different prepared polymer casting solutions (degrees of sulfonation,

solvent, salt loadings, etc) to observe how diffusion in the solution would dictate the resultant composite.

7.3 Conclusion

From the high proton conductivity determined from EIS and fast ion dynamics observed from solid-state NMR a homogeneous sulfonated functionalized host with a fluorinated salt was the best composite material suitable for fuel cells at high anhydrous temperatures. Materials synthesized in this thesis are highly competitive with the properties of other anhydrous electrolytes being considered for fuel cell applications anhydrous electrolytes for fuel cell applications. Solid-state NMR provided additional insights into the proton conduction mechanisms and rates of ion dynamics within the composites studied.